Study of GPS Multipath Effects for Structural Deformation Monitoring

by

Ping Zhong

The thesis presented for the Degree of Doctor of Philosophy

The Hong Kong Polytechnic University

2008

The Hong Kong Polytechnic University

Department of Land Surveying & Geo-Informatics

Study of GPS Multipath Effects for Structural Deformation Monitoring

by

Ping Zhong

A thesis submitted in partial fulfillment of the requirements for the degree of Doctor of Philosophy

December 2007

CERTIFICATE OF ORIGINALITY

I hereby declare that this thesis is my own work and that, to the best of my knowledge and belief, it reproduces no material previously published or written, nor material that has been accepted for the award of any other degree or diploma, except where due acknowledgement has been made in the text.

____________________________(Signed)

__________Ping Zhong________(Name of student)

Abstract

GPS signal multipath effects are one of the most important error sources in precise GPS positioning and navigation. Although various methods have been proposed to reduce the effects, the existing methods are not always as effective as desired. This thesis aims to develop further the methods for mitigating the multipath effects.

A Vondrak filter is proposed for smoothing out the multipath effects in precise GPS applications such as structural vibration monitoring. The technique has a good signal resolution at the signal truncation frequency band, i.e. at the upper or lower limit of a frequency band. The proposed filter is compared with two commonly used filters, i.e. the wavelet and adaptive FIR filters, for such applications. Results from the study reveal that the performances of the Vondrak and wavelet filters are similar and superior to the adaptive FIR filter.

Due to the good filtering properties of Vondrak and wavelet filters, new filtering methods (i.e. cross-validation Vondrak filter (CVVF) and cross-validation wavelet filter (CVWF)), based on the Vondrak or wavelet filter and the technique of cross-validation, are developed for separating noise from the signals in GPS coordinate series. Test results show that both the proposed CVVF and CVWF methods are effective signal decomposers but the former is superior to the latter.

In investigating the variations in GPS multipath day-to-day repeatability, we propose to integrate the CVVF method, the existing stochastic SIGMA-Δ model and the aspect repeat time adjustment (ARTA) method to maximize GPS accuracy improvements. Test results show that the correlation of multipath signals decreases with the increase of the time interval between the current date and the date when the multipath model was established. The shorter the period of multipath signal, the weaker the correlation.

A sidereal filtering method is also developed based on GPS single difference observations for mitigating the effects of GPS signal multipath and diffraction. Test examples show that the new filtering method can reduce the GPS signal multipath and diffraction effects more effectively, and improve the accuracy by about 50–80%. The method is also advantageous in that it can be implemented in real-time applications such as deformation monitoring.

Finally, the thesis investigates the multipath mitigation using modernized GNSS signals due to the fact that the additional redundancy gives better averaging effects in the adjustment model. A GNSS data simulator is used to generate multipath contaminated GPS, GLONASS and Galileo data. Results show that an accuracy improvement of 63% on average can be obtained by using the future GPS/GLONASS/Galileo multiple-frequency data when compared to the current GPS single-frequency data.

Acknowledgements

Foremost, I would like to acknowledge the help of my chief supervisor, Prof. Xiaoli Ding, and co-supervisor, Dr. Wu Chen. Both have been extremely supportive, patient and generous in sharing their knowledge. In addition, Prof. Ding has always gone to great lengths to take care of me – encouraging professional development through seminars and conferences, making sure I had funding, and exhibiting comprehensive understanding when I needed some time off. I cannot imagine having gone through this experience without his guidance and help.

Prof. Dawei Zheng at Shanghai Astronomical Observatory deserves special recognition for his constructive suggestions and continuous encouragement. To me, he was much more than a teacher; he was both a friend and mentor.

My special appreciation goes to Prof. Dingfa Huang at Southwest Jiaotong University for his huge understanding and support.

I would like to acknowledge the kind help of staff members of the Department of Land Surveying & Geo-Informatics, Hong Kong Polytechnic University (HKPolyU) for their suggestions and encouragement during my studies. My fellow graduate students at the HKPolyU over the years are also appreciated for making my life in Hong Kong easier and more colorful. Thanks also go to Dr. Christopher Green of the Department of English, HKPolyU for polishing my English in the final stage.

Finally, I would like to thank my very important support network of friends and loved ones – my parents, and all my buddies for their unwavering support and patience.

Table of Contents

[blank page]

List of Figures

List of Tables

Chapter 1

Introduction

1.1 Background

Since the Global Positioning System (GPS) became operational in 1992, it has been revolutionizing the technologies for navigation and positioning, owing to its advantages of high accuracy, ability to operate in all meteorological conditions and the fact that it does not require inter-visibility between measuring points (Leick, 2004). However, GPS observations are contaminated by various error sources. Fortunately, differential GPS techniques can largely eliminate the common-mode errors between reference and rover GPS stations that result from ionospheric and tropospheric refraction and delays, satellite and receiver clock biases, and orbital errors. However, some other errors, such as GPS signal multipath effects, cannot be removed with this approach and are still significant in GPS positioning (Elósegui et al., 1995; Leick, 2004). For example, the effects of multipath on the carrier phase can amount to around 1/4 of the GPS signal wavelength (e.g. about 4.8 cm for L1) (Georgiadou and Kleusberg, 1988).

Multipath is a phenomenon whereby a signal is reflected or diffracted from nearby obstacles and arrives at a receiver's antenna via two or more different paths. A GPS receiver cannot distinguish between the direct and the indirect signals and thus aligns the local replicas of the code and carrier generated in the receiver to the composite signal instead of the direct signal. Multipath may be specular or diffused in nature. Diffused multipath results in relatively small errors due to the fact that it is generally uncorrelated with time and takes on an unbiased, random appearance (Braasch, 1996). However, specular multipath is more problematic due to the fact that it produces systematic, time-correlated errors that are not easily addressed (Larson et al., 2007). As a result, a multipathed signal introduces errors to the code and carrier-phase measurements, which then propagate into coordinates based on these data.

1.2 Previous Work

Many approaches for multipath reduction and correction have been previously developed. First, the effects of multipath can be avoided or reduced before the indirect signal is received by the GPS receiver, for instance, by carefully choosing observation sites that do not have potential GPS signal reflectors in their vicinities, by using a multipath-rejecting antenna design (e.g. chokering antenna, advanced pinwheel compact controlled reception pattern antenna (Kunysz, 2001)), or by placing frequency-absorbing foam underneath the antennas (Elòsegui et al., 1995). Due to the fact that the multipath signals typically enter the antenna through low elevation angles, an elevation cutoff angle can also be used in most GPS data processing software packages (Hoffman-Wellenhof et al., 2001). The main disadvantage of the method is that the rejection of some of the satellites or signals may degrade the strength of the satellite geometry, resulting in poor position determination.

After signal reception, the multipath effects can be mitigated within the GPS receiver. Advances in receiver data processing algorithms have also led to the development of so-called multipath “resistant” receivers. For example, the narrow correlator spacing technology (van Dierendonck et al., 1992), the multipath estimation technology (MET) (Townsend and Fenton, 1994), the multipath eliminating delay lock loop (MEDLL) (van Nee, 1992; Townsend et al., 1995), the strobe correlator (SC) and enhanced strobe correlator (ESC) (Garin and Rousseau, 1997), and the multipath mitigation window (MMW) (Bétaille at el., 2003) attempt to eliminate code and/or carrier-phase multipath effects at the signal processing level in the receiver. Compared to a narrow correlator receiver, MET and MEDLL receivers reduce delay lock loop (DLL) multipath effects by 25–50% and up to 90% respectively. The SC and ESC show a significant improvement in mitigating multipath signals with a long delay. However, the antenna and receiver tracking techniques perform less satisfactorily for short-delay multipath signals caused by close-by reflectors (Braasch and van Dierendonck, 1999; Ray et al., 2001; Weill, 2003). Also, these techniques are limited to receiver manufactures that are licensed to use these technologies, thus GPS users rarely have access to receiver hardware and none of these techniques are applicable to all existing receivers. After these efforts, the residual multipath effects are still as large as several centimeters in positions and are still significant in many precise GPS applications where the accuracy requirements are often at the millimeter level.

Several data post-processing techniques have been developed to reduce further GPS multipath effects. For example, a common practice for reducing code multipath is to smooth the pseudorange with the more precise carrier phase (Misra and Enge, 2001). One technique is to map the environment around a GPS antenna so that multipath corrections for each satellite signal can be determined as a function of its azimuth and elevation (Cohen and Parkinson, 1991). The software package TEQC (Estey and Meetens, 1999) can also be used to assess the effects of code multipath (Ogaja and Hedfors, 2006). Georgiadou and Kleusberg (1988) demonstrate that dual-frequency phase observations can be used to identify the presence of the multipath signals. Another technique is to use the signal-to-noise ratio (SNR) or carrier-to-noise power-density (C/N_0) recorded in the observational data file to reduce the effects of multipath or signal diffraction (Axelrad et al., 1996; Comp and Axelrad, 1998; Brunner et al., 1999; Bilich and Larson, 2007). Other techniques are used to reduce the multipath effects at the post-processing stage, extracting or eliminating the errors using filter-based approaches, such as Kalman filters (Ince and Sahin, 2000), band-pass finite impulse response (FIR) filters (Han and Rizos, 1997), wavelet filters (Teolis, 1998; Souza and Monico, 2004; Satirapod and Rizos, 2005), and adaptive filters (Ge et al., 2000). Modelling approaches that use the repeating property of GPS multipath signals are also developed, such as sidereal filtering (Genrich and Bock, 1992; Nikolaidis et al., 2001) and modified sidereal filtering (MSF) (Choi et al., 2004; Larson et al., 2007). These methods subtract a filter value from coordinates at each epoch and then make corrections to the subsequent GPS coordinates.

In summary, despite the research efforts devoted to mitigating the multipath effects, the existing methods are not always as effective as desired, especially in precise GPS applications. For example, in structural vibration monitoring, it is often difficult for most of the filter-based techniques to distinguish between the multipath signals and the structural vibrations, especially when the vibrations tend to fall in the same frequency range as the multipath signals. Many of these techniques, as demonstrated above, cannot be used in real-time applications such as deformation monitoring. In addition, a few studies have addressed the variations in the multipath day-to-day repeatability and the establishment of reliable multipath models when taking advantage of this repeating property. Little attention has been paid to the multipath mitigation technique using modernized GPS, GLONASS and Galileo signals.

1.3 Research Objectives

This study sets out to further develop methods for more effectively mitigating the carrier phase multipath effects for precise GPS applications, especially in structural deformation monitoring. More specifically, the thesis will:

- Further study and understand the features of GPS multipath effects;
- Study filters for effectively separating the multipath effects and the structural vibrations;
- Study and develop various methods for better mitigating the effects of GPS multipath; and

- Investigate real-time applications of some of the multipath mitigation methods.

1.4 Contributions of the Study to the Field

The contributions of this thesis involve:

- A Vondrak bandpass filter has been developed for mitigating multipath effects in precise GPS applications such as structural vibration monitoring. The proposed filter has been compared with two commonly used filters for such applications. The advantages and disadvantages of each of the filters are discussed.
- Two new filtering methods, cross-validation Vondrak filter (CVVF) and cross-validation wavelet filter (CVWF), based on Vondrak or wavelet filter and the technique of cross-validation, have also been developed for separating signals from noise in coordinate series and applied to establish reliable GPS multipath signal models. When using these methods, a balance between data fitting and smoothing can be better achieved in the filtering process, and signals can be automatically identified from noise. The proposed methods have been validated using both simulated data series and real GPS observations.
- An integrated use of the CVVF method, stochastic SIGMA-Δ model and aspect repeat time adjustment (ARTA) method has been proposed to

investigate the variations in multipath day-to-day repeatability and to maximize GPS accuracy improvements. The proposed method has been evaluated by comparison with traditional methods.

- A sidereal filtering method, based on GPS single difference observations, has also been developed for mitigating the effects of GPS signal multipath and diffraction on a satellite-by-satellite basis. The method is advantageous in that it can be implemented in real-time.
- Multipath mitigation using modernized GPS, GLONASS and Galileo signals has also been investigated. The effectiveness for mitigating multipath effects has been assessed by using data generated from a GNSS simulator.

1.5 Thesis Structure

This thesis consists of eight chapters. Chapter 2 provides an overview of GPS and GPS multipath effects. Chapter 3 develops the Vondrak bandpass filter and applies the filter to structural vibration monitoring for multipath mitigation. Chapter 4 presents the methods based on the Vondrak or wavelet filter and the method of cross-validation for establishing the GPS multipath model and mitigating multipath effects. Based on the proposed filter presented in Chapter 4 and the existing stochastic SIGMA-Δ model and ARTA method, Chapter 5 discusses the integrated use of these methods in maximizing improvement of GPS accuracy when taking advantage of the multipath day-to-day repeatability. Chapter 6 presents the sidereal filtering method based on GPS single differences for reducing the effects of GPS signal multipath and diffraction. The impact of modernized GNSS signals on multipath mitigation using the standard single-epoch least squares method is investigated in Chapter 7. Finally, Chapter 8 draws conclusions and presents recommendations for future research.

Chapter 2

Overview of GPS and GPS Signal Multipath

This chapter presents an overview of the Global Positioning System (GPS) and the effects of GPS signal multipath. This chapter begins with a discussion of the system segmentation, followed by an examination of GPS observables and various error sources. The characteristics of multipath effects caused by specular reflection, diffusion and diffraction are then described, followed by discussions of the impacts of reflector material properties on multipath. Finally, the characteristics of multipath effects are summarized.

2.1 System Segmentation

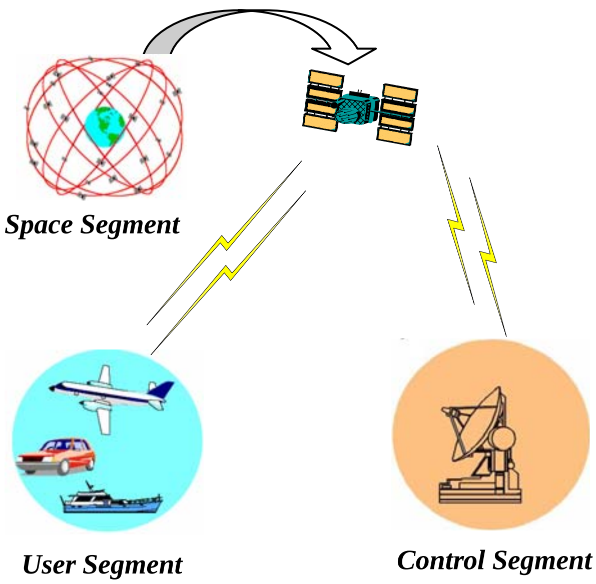

Fig. 2.1 GPS system consisting of three components: space, control and user.

GPS is a satellite based radio-navigation system that is capable of providing position, velocity and time 24 hours per day, anywhere on or near the surface of the Earth and under any weather conditions. The system is composed of three basic segments: space, control, and user (Spilker and Parkinson, 1996) (see Fig. 2.1).

Space Segment

The space segment consists of the GPS constellation, composed of orbiting satellites which continuously transmit ranging signals. The constellation has a nominal 24 satellites and a maximum of 36 in six nearly circular orbits inclined at an angle of 55° at an altitude of about 20,200 km above the earth and a period of approximately 12 sidereal hours. The constellation was designed to provide global coverage with four to eight visible satellites simultaneously above a 15° elevation angle at all times (Hofmann-Wellenhof et al., 2001).

GPS employs code division multiple access (CDMA), in which multiple signals can be transmitted at exactly the same frequency (Spilker, 1996). Signals from individual satellites are identified by a unique Pseudo Random Noise (PRN) code. Each GPS satellite transmits two carrier signals produced at L band frequencies of 1575.42 MHz and 1227.60 MHz respectively. The carrier signals are modulated by three binary codes: public C/A-code (Coarse Acquisition), encrypted P-code (Precise) and navigation message. The navigation message is a 50 Hz signal containing information on the ephemerides of the satellites, GPS time, clock behavior, and system status parameters. The data in the navigation message are relative to GPS time. The time is defined by the onboard atomic clocks of each satellite and maintained by the control segment.

Control Segment

The control segment is currently in development consists of the following elements: a master control station, six monitor stations and four ground control stations throughout the world. Monitor stations track all GPS satellites in view and collect the ranging data of each satellite. This information is then sent to the master station and processed to determine precise satellite orbits and clock corrections. Updated results are finally passed to the ground control stations and uploaded to each satellite via ground antennas. To further improve system accuracy, six more monitor stations operated by the National Geospatial-Intelligence Agency (NGA) were added to the grid in 2005. Further control segment enhancements are planned for introduction with the launch of the Block III satellites.

User Segment

This segment is composed of GPS antennas, receivers and the user community. GPS antennas collect satellite signals, and receivers calculate position, velocity and time estimates. The user community is provided with two GPS services: the standard positioning service (SPS) for the public and the precise positioning service (PPS) for military and other authorized users. SPS positioning accuracy has been intentionally degraded by selective availability (SA) measures, which entail a dither of the satellite clocks and falsification of the navigation message (Leick, 2004). SA was implemented on March 25, 1990, on all Block II satellites, but turned off on May 1, 2000. The civilian GPS user community has increased dramatically in recent years due to the emergence of low-cost portable GPS receivers, the switch off of the SA effect and the expanding areas of GPS applications, such as navigation, surveying, mapping, and time dissemination.

2.2 GPS Observables and Error Sources

2.2.1 Basic GPS Observables

GPS observables are ranges which are determined from measured time or phase differences between received signals and receiver generated signals. Since the ranges are biased by atmospheric signal delays and satellite and receiver clock errors, they are denoted as pseudoranges.

When GPS signals pass through the atmosphere from the satellite to the receiver, they suffer a number of propagation effects, such as ionospheric and tropospheric refraction and delays, and multipath. Besides the clock errors, the pseudorange is therefore affected by various propagation errors or biases. The mathematic model for code measurements in the unit of meter is given by (Leick, 2004)

$$\begin{aligned} P_i^j(t) = \rho_i^j(t) + c\,(\delta_i(t) - \delta^j(t)) + \delta_{i,orb}^j(t) \\ + \delta_{i,I_p}^j(t) + \delta_{i,T}^j(t) + \delta_{i,Mp}^j(t) + \varepsilon_{i,p}^j(t) \end{aligned} \tag{2.1}$$

where $P_i^j(t)$ represents the pseudorange at an epoch t between the observing site i and the satellite j; $\rho_i^j(t)$ is the geometric distance between the satellite and the receiver; c is the speed of light; $\delta_i(t)$ and $\delta^j(t)$ denote the receiver and satellite clock biases with respect to GPS time respectively; $\delta^j_{i,orb}(t)$, $\delta^j_{i,I_p}(t)$, and $\delta^j_{i,T}(t)$ are the range errors resulting from the satellite orbit, the ionospheric and tropospheric delays respectively; $\delta^j_{i,Mp}(t)$ is the code range multipath error; and $\varepsilon^j_{i,p}(t)$ is the code measurement noise of the GPS receiver.

Similar to the code measurements, the carrier phase measurements in the unit of meter are represented by (Hofmann-Wellenhof et al., 2001)

$$\begin{aligned}\phi^j_i(t) &= \rho^j_i(t) + c(\delta_i(t) - \delta^j(t)) - \lambda N^j_i(t_0) \\ &\quad + \delta^j_{i,orb}(t) - \delta^j_{i,I_p}(t) + \delta^j_{i,T}(t) + \delta^j_{i,M\varphi}(t) + \varepsilon^j_{i,\varphi}(t)\end{aligned} \tag{2.2}$$

where $\phi^j_i(t)$ is the measured carrier phase; λ denotes the wavelength of the GPS carrier; $N^j_i(t_0)$ is the integer phase ambiguity referring to the first epoch of observations t_0 and remains constant as long as the signal remains locked; $\delta^j_{i,M\varphi}(t)$ is the carrier phase multipath error; and $\varepsilon^j_{i,\varphi}(t)$ is the receiver carrier noise.

2.2.2 Differential GPS Observables

Differential positioning with GPS is a technique where two or more receivers are used. For receivers A and B, observing the same satellite j at epoch t, the resulting single-difference code and phase observables are given by (Hofmann-Wellenhof et al., 2001; Leick, 2004)

$$\Delta P^j_{AB}(t) = P^j_B(t) - P^j_A(t) = \Delta\rho^j_{AB}(t) + c\cdot\Delta\delta_{AB}(t) + \Delta\delta^j_{AB,Mp}(t) + \Delta\varepsilon^j_{AB,p}(t) \tag{2.3}$$

$$\begin{aligned}\Delta\phi_{AB}^{j}(t) &= \phi_{B}^{j}(t)-\phi_{A}^{j}(t)\\ &= \Delta\rho_{AB}^{j}(t)-\lambda\cdot\Delta N_{AB}^{j}(t_0)+c\cdot\Delta\delta_{AB}(t)+\Delta\delta_{AB,M\varphi}^{j}(t)+\Delta\varepsilon_{AB,\varphi}^{j}(t)\end{aligned} \tag{2.4}$$

where Δ represents the difference between receivers, e.g., $\Delta\rho_{AB}^{j}=\rho_{B}^{j}-\rho_{A}^{j}$ is the differential true range between receivers *A* and *B* and satellite *j*. Satellite clock errors are eliminated by using single difference between receivers with respect to the same satellite.

For two receivers *A* and *B*, and two satellites *j* and *k*, single differences ΔP_{AB}^{j}, ΔP_{AB}^{k}, $\Delta\phi_{AB}^{j}$ and $\Delta\phi_{AB}^{k}$ can be formed according to Equations (2.3) and (2.4). Subtracting these single differences, one obtains the double-difference code and phase observables (Hofmann-Wellenhof et al., 2001; Leick, 2004):

$$\nabla\Delta P_{AB}^{jk}(t)=\Delta P_{AB}^{k}(t)-\Delta P_{AB}^{j}(t)=\nabla\Delta\rho_{AB}^{jk}(t)+\nabla\Delta\delta_{AB,Mp}^{jk}(t)+\nabla\Delta\varepsilon_{AB,p}^{jk}(t) \tag{2.5}$$

$$\begin{aligned}\nabla\Delta\phi_{AB}^{jk}(t) &= \Delta\phi_{AB}^{k}(t)-\Delta\phi_{AB}^{j}(t)\\ &= \nabla\Delta\rho_{AB}^{jk}(t)-\lambda\cdot\nabla\Delta N_{AB}^{jk}(t_0)+\nabla\Delta\delta_{AB,M\varphi}^{jk}(t)+\nabla\Delta\varepsilon_{AB,\varphi}^{jk}(t)\end{aligned} \tag{2.6}$$

where ∇ represents the difference between satellites and Δ indicates the difference between receivers. The advantage of the double-difference observation is that the receiver clock errors are further eliminated. Double-difference observables are commonly used for GPS baseline solution.

The errors contaminating GPS signals can be classified into two categories: spatially correlated or uncorrelated errors. Ephemeris errors, ionosphere and troposphere biases are spatially correlated between receivers tracking the same satellite simultaneously. The spatially correlated errors tend to be cancelled by differencing measurements between receivers for short baselines, but increase in proportion with the baseline length. Spatially uncorrelated errors, such as multipath and measurement noise, depend on the individual environment or receiver. These errors do not relate to the baseline length and cannot be removed with the differencing method. Various error sources are discussed in the following subsections.

2.2.3 Ephemeris Errors

Ephemeris errors are inaccuracies of the satellite location represented by the broadcast or precise ephemeris. Broadcast ephemeris can be used in real-time applications with an accuracy of 1.6 m, while precise ephemeris can be applied to post-processing applications with errors of 5 cm (IGS, 2005). Satellite ephemeris errors in differential GPS mode depend on the length of baseline (between reference station and user). The impact of orbital errors on baseline length can be estimated by (Bauersima, 1983; Wells et al., 1987)

$$|\Delta b| = \frac{b}{r} \cdot |\Delta r| \tag{2.7}$$

where Δb is the baseline error; Δr is the orbital error; b is the baseline length; and r is the distance between satellite and user. Therefore, for short and medium baselines, satellite orbital errors will become insignificant.

2.2.4 Ionosphere Errors

The ionosphere is the part of the atmosphere extending in various layers from about

50 km to 1000 km above the earth's surface. The free electrons in the ionosphere affect the propagation of GPS signals (speed, direction and polarization) as they pass through the layers. The ionosphere is a dispersive medium, hence the ionospheric delay is frequency-dependent and its impacts on L1 and L2 signals are different. By taking advantage of the dispersive property, a linear combination of dual-frequency pseudorange or carrier phase observations can be used to eliminate the first order ionosphere delay. An improved model was also proposed by Brunner and Gu (1991) to account for high-order ionospheric errors. For single-frequency applications, the broadcast ionospheric delay coefficients in the half-cosine ionospheric delay model can be used to remove about 50% of the delay (Klobuchar, 1987).

The magnitude of ionospheric delay is related to the total electron content (TEC) along the signal propagation path from the GPS satellite to the receiver. The TEC depends on sunspot activities (an approximately 11-year cycle), seasonal and diurnal variations, elevation and azimuth of the satellite, and receiver location. The ionosphere can delay the GPS signal by several tens of meters in zenith direction under extreme conditions (Parkinson and Enge, 1996).

2.2.5 Troposphere Errors

Tropospheric errors are caused by the neutral atmosphere comprising the lower 10 km of the earth's atmosphere. This delay can be separated into a dry and a wet component, and about 90% of the total error arises from the dry and about 10% from the wet. Unlike the ionosphere, the troposphere is a nondispersive medium with respect to the GPS signals; hence the tropospheric delay is frequency-independent and is related only to the meteorological parameters (atmospheric pressure, temperature and relative humidity). The tropospheric errors can amount to about 2.3 m at the zenith and about 20 m near the horizon (Seeber, 2003). Several models (e.g. the Hopfield, Saastamoinen and Niell models) have been developed to estimate the tropospheric delay as a function of the satellite elevation, receiver height and meteorological parameters (Hofmann-Wellenhof et al., 2001). These models typically remove 90% of the delay, but the unmodeled error can reach 2-3 m for an elevation of 5° (Parkinson and Enge, 1996).

2.2.6 Multipath and Receiver Errors

GPS multipath occurs when signals traveling from a satellite to a receiver propagate via two or more paths due to reflections or diffractions from nearby obstacles such as buildings, trees or fences. The multipath signals combined with the direct signal, result in degraded accuracy of both code and carrier phase measurements. Details of the multipath theory will be presented in the next subsection.

Receiver error is caused mainly by thermal noise and dynamic stress of the receiver, which greatly depends on the design of the receiver (Leva et al., 1996). The code noise is at the level of several decimeters for most modern receivers, while the phase noise is at the level of a few millimeters. Multipath and noise errors cannot be eliminated by using the differential GPS techniques due to their spatial uncorrelation characteristics between the reference and the user.

2.3 GPS Signal Multipath

Carrier phases are always required for precise GPS applications where the accuracy requirements are often at the centimeter or millimeter level due to their shorter wavelengths. In this section, the carrier phase multipath disturbance is emphasized.

2.3.1 Specular Multipath

Amplitude

Specular multipath effects occur when the GPS signal is reflected by a smooth surface, which can be illustrated using a planar vertical reflection surface with distance *d* from the antenna (see Fig. 2.2) (Georgiadou and Kleusberg, 1988; Leick, 2004).

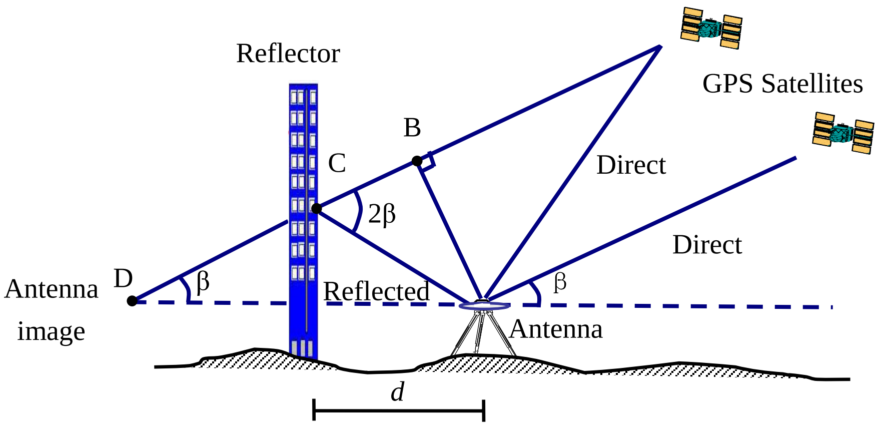

Fig. 2.2 GPS multipath signals due to reflection from a vertical planar surface.

The direct line-of-sight carrier phase observable is described by:

$$S_d = A\cos\varphi \tag{2.8}$$

and the reflected signal can be written as:

$$S_r = \alpha A \cos(\varphi + \theta), \qquad 0 \le \alpha \le 1 \tag{2.9}$$

where A and φ are the amplitude and phase of the direct signal respectively; α is the amplitude attenuation factor, which is the ratio of the reflected signal amplitude with respect to the direct signal, and θ is the multipath phase shift.

It is seen from Fig. 2.2 that the multipath delay is the sum of the distance *BC* and *CD*, which equals $2d\cos\beta$. When converting the distance into cycles and then to radians, the total multipath phase delay is expressed as:

$$\theta = \frac{4\pi d}{\lambda}\cos\beta + \phi \tag{2.10}$$

where λ is the carrier wavelength; β is the incident angle of the satellite signal; and ϕ is the fractional shift. The superposition of the direct and single reflected signals is:

$$S = S_d + S_r = R\cos(\varphi + \psi) \tag{2.11}$$

where the amplitude R and multipath delay ψ of the composite signal may be represented by (Leick, 2004):

$$R = A(1 + 2\alpha\cos\theta + \alpha^2)^{1/2} \tag{2.12}$$

$$\psi = \arctan\left(\frac{\alpha\sin\theta}{1 + \alpha\cos\theta}\right) \tag{2.13}$$

The maximum path delay can be found from Equation (2.13) when $\partial\psi / \partial\theta = 0$, if constant reflectivity is considered (e.g. α is constant). Thus, the maximal multipath effects on phase measurements occur for $\alpha = 1$ and $\theta = \pm\pi / 2 = 1/4$ cycle. Converting the phase into range, it gives 1/4 of the GPS signal wavelength (or about 4.8 cm for L1 carrier phase observable).

Figure 2.3 shows the multipath errors for the L1 phase measurement, assuming that the elevation angle β is $\pi / 4$ and the amplitude attenuation α ranges from 1 (reflected signal as strong as direct signal) to 0 (no reflection) with the increase of distance *d* from 0 to 50 m.

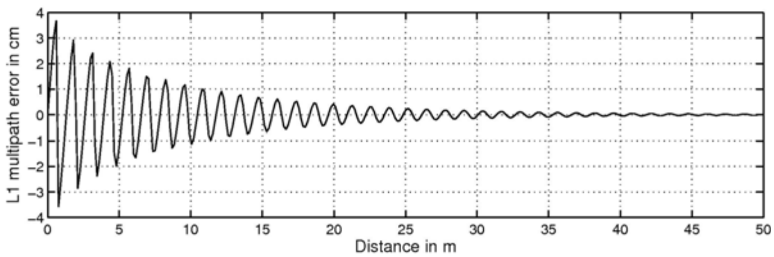

Fig. 2.3 Relationship between L1 multipath error and distance.

The result in Fig. 2.3 shows that the multipath error due to the close-by reflectors tends to cause more trouble than do signals with a long delay. This is attributed to the signals reflected from nearby reflectors suffering less spreading loss than from distant obstacles.

Period

The frequency of multipath f_ψ can be expressed by differentiating Equation (2.10):

$$f_{\psi} = \frac{1}{2\pi}\frac{d\theta}{dt} = \frac{2d}{\lambda}\sin\beta\frac{d\beta}{dt} \tag{2.14}$$

Equation (2.14) indicates that the multipath frequency is proportional to distance d and the signal frequency, and is a function of the elevation angle of GPS satellite.

Figure 2.4 shows the variations of the L1 multipath period with the distance between reflector and antenna at elevation angles of 15° and 75° respectively. Here the change rate of the elevation angle $d\beta / dt$ is assumed to be 0.07 mrad/sec (one-half of the satellite's mean motion (Leick, 2004)).

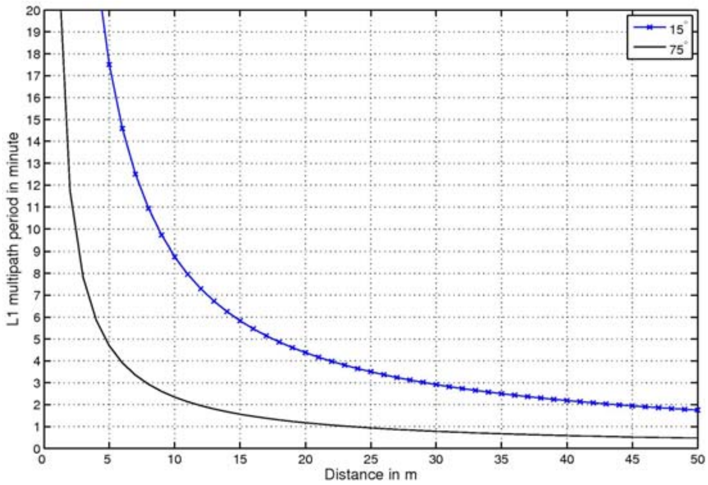

Fig. 2.4 Relationship between L1 multipath period and distance at elevation angles of 15° and 75°.

It is seen from Fig. 2.4 that the higher the satellite elevation angle, the greater the distance between the vertical reflectors and the antenna, the shorter the period of the multipath errors.

Since the current antenna and receiver tracking techniques perform less satisfactorily for short-delay multipath signals caused by close-by reflectors, e.g., less than 30 m (Braasch and van Dierendonck, 1999; Ray et al., 2001; Weill, 2003), the typical multipath periods are considered varying from tens of seconds to tens of minutes.

Repeatability

GPS multipath signals repeat largely themselves every sidereal day if the relative geometry of the satellites, the reflectors and the antennas remains unchanged between sidereal days (Georgiadou and Kleusberg, 1988; Hofmann-Wellenhof et al., 2001; Leick, 2004). To show the day-to-day repeating property of GPS multipath signals, the carrier phase multipath series obtained in our experiment over three consecutive days are taken as an example (Fig. 2.5). Offset of 2 cm is added to separate the time series for clarity. It is seen from Fig. 2.5 that the oscillations due to multipath are apparent as well as the day-to-day repeatability.

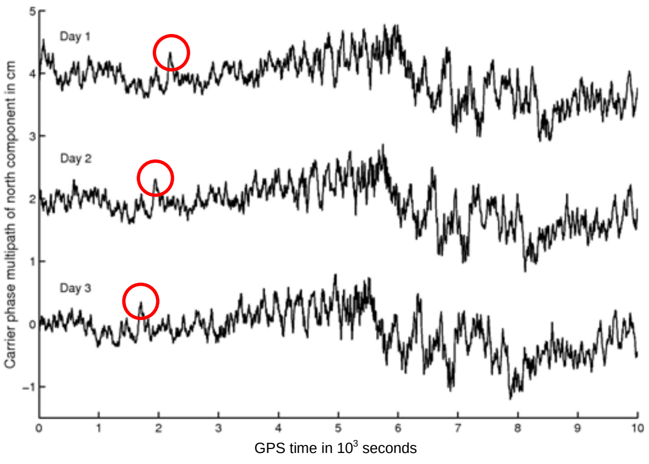

Fig. 2.5 An illustration of GPS multipath day-to-day repeatability.

The sidereal day-to-day correlation of the GPS coordinate series has been discussed in multipath research over the last decade (Elòsegui et al., 1995; Radovanovic, 2000; Wübbena et al., 2001; Park et al., 2004; Zheng et al., 2005). The results indicate that the repeatability of the GPS multipath is useful to verify the presence of the multipath by analyzing its repeating patterns and therefore improving the GPS accuracy.

2.3.2 Diffusion and Diffraction

Diffuse multipath occurs when the GPS signal is incident on a rough (relative to the signal wavelength) surface and the reflected signal is scattered in multiple directions. Diffraction occurs when the GPS signal is reflected by the edges or corners of the reflectors. One example of diffraction is that the satellites are tracked by the GPS receiver, although the direct line-of-sight between the GPS satellite and the antenna is obstructed.

Unlike specular multipath, diffuse multipath and diffraction do not usually show such a sidereal day-to-day repeatability due to that they are generally uncorrelated with time and noise-like in behavior (Braasch, 1996). The effects of diffusion and diffraction are equivalent to the sum of multiple reflections with different amplitudes and phases, depending on the nature of the surface (e.g. its roughness and structure).

2.3.3 Impacts of Reflector Material on Multipath

Although the direct and reflected signals are simultaneously transmitted by GPS satellites, the strength of the reflected signal tends to attenuate. Some of the factors affecting signal attenuation are the properties of the reflector material. The metal materials have good electrical conductivity, thus the electromagnetic wave undergoes total reflection. The geodetic GPS antenna tends to have a metallic ground plate that serves to attenuate waves caused by ground reflection under the antenna. Multipath errors reflected from non-metal materials rely on the dielectric constant. Generally, the greater the dielectric constant, the higher the reflection. The dielectric constants of some materials are listed in Table 2.1 (Guo et al., 1995).

Table 2.1 Dielectric constants of some materials.

Material	Dielectric constant	Material	Dielectric constant
Concrete	5	Soil moist	9.5
Fiberglass	2.55	Soil watery	20.8
Sand stone	4.5	Vacuum	1 (by definition)
Silex	3.5	Water	61.5
Soil dry	3.2	Wood dry	6.7

It is seen from Table 2.1 that moist and watery soils have larger dielectric constants than does dry soil. Moreover, the dielectric constant of water is as large as 61.5, which may result in severe multipath errors. Therefore, the general recommendation for multipath mitigation is the careful selection of antenna site, avoiding any strong reflectors, such as water surfaces, in the vicinity.

2.4 Summary

The system configuration, observables and various error sources of GPS have been briefly discussed in this chapter, along with the carrier phase multipath effects. Some characteristics of the multipath are summarized as follows:

- The amplitude of the multipath does not exceed a certain amount. The maximum of multipath effects on carrier phase can amount to about 1/4 of the GPS signal wavelength.
- The multipath disturbance exhibits a frequency behavior. Typical multipath periods are considered to range from tens of seconds to tens of minutes.
- The day-to-day repeating properties of GPS multipath signals are significant over consecutive days, although there are effects of diffusion and diffraction.
- The elimination of multipath signals is possible by setting satellite cut-off elevation angle, using chokering antennas and carefully selecting observation sites that do not have potential GPS signal reflectors in the vicinity.

[blank page]

Chapter 3

Separating GPS Multipath Effects and Structural Vibrations Using Digital Filters

3.1 Introduction

A large number of major structures (e.g. high-rise buildings and long suspension bridges) have been built in many parts of the world. To ensure their integrity, durability and reliability, especially under severe loading conditions, such as during earthquakes, typhoons and storms, there is an increasing need to monitor the dynamic behaviors of the structures. Although conventional techniques can be used to measure the structural vibrations and displacements, they exhibit limitations. For example, accelerometers are unable to measure slow motion or deformation of a building. Laser interferometers and electronic distance measurement instruments are often difficult to apply in the on-site environment, and may not produce accurate results (Lovse et al., 1995).

GPS technology has been widely used in structural vibration monitoring during the last two decades, owing to its advantages of high accuracy, ability to operate in all meteorological conditions and not requiring for inter-visibility between measuring points when compared with the traditional methods (Lovse et al., 1995; Brown et al., 1999; Ogaja et al., 2001; Li et al., 2006). When GPS is applied to such applications, the baseline length is generally short (e.g. 5 kilometers or shorter). In this case, the use of differential GPS techniques can largely eliminate the common-mode errors between reference and rover GPS stations that result from ionospheric and tropospheric refraction and delays, satellite and receiver clock biases, and orbital errors. However, some other errors, such as GPS signal multipath effects, cannot be removed with this approach and still have significant effects on GPS position estimates (Elósegui et al., 1995; Leick, 2004). The resulting monitoring results mainly consist of GPS multipath disturbance, random noise and vibrations. It is therefore essential to apply an appropriate method in data processing for effectively separating the multipath errors and the structural vibrations.

Several filter-based approaches have been developed to extract or eliminate multipath effects, such as wavelet filters (Teolis, 1998; Ogaja et al., 2001; Souza and Monico, 2004; Satirapod and Rizos, 2005) and adaptive finite impulse response (FIR) filters (Kinawi et al., 2002; Chan et al., 2005). For some of the filters, the selection of filter parameters is challenging and it is often difficult to distinguish between the multipath signals and the structural vibrations, especially when the vibrations may fall into the same frequency band as the multipath signals.

A Vondrak bandpass filter (Zhong et al., 2006; Zhong et al., 2007) is proposed here to smooth out the multipath errors and extract the vibration signals. The Vondrak bandpass filter and two other filters (i.e., wavelet and adaptive FIR) applicable to structural vibration monitoring are first described. Despite these filters being able to improve GPS accuracy to different extents, much remains uncertain about which filter has superior performance when retrieving vibration signals from GPS observational series. Field GPS experiments are then carried out to obtain a deeper insight into the filter performance. Based on the test results, advantages and disadvantages of each of the filters are discussed from the aspects of precision improvement, selection of filter parameters and computation efficiency. Finally, recommendations for selecting filters and filter parameters in different situations are presented.

3.2 Filters for GPS Structural Vibration Monitoring

Signals can be separated from noise using filters due to the distinct time-frequency characteristics of the signals and noise. For example, the random noise exists all through the GPS observations and exhibits a high-frequency feature, whereas the structural vibration signal has a local distribution in the frequency domain. Research (Lovse et al., 1995) suggested that typical structural vibrations range from 10 to 200 mm in amplitude and from 0.1 to 10 Hz in frequency. Thus the frequencies of vibrations are low relative to the random noise.

As discussed in Chapter 2, the maximum of multipath effects on the carrier phase can amount to a quarter of the carrier wavelength, and the typical multipath periods range from tens seconds to tens minutes. Therefore, the frequencies of multipath disturbances are also low relative to the random noise, but may be close to those of the vibrations and may even fall in the same frequency range as the vibration signal.

It is significant to use a filter with high performance for extracting the accurate vibration signals. Fundamentals of the three aforementioned filters and filtering steps for separating vibrations from multipath are described as follows.

3.2.1 Vondrak Bandpass Filter

The performance of a digital filter relies on its frequency response function (FRF). The FRF of the Vondrak filter proposed by Huang and Zhou (1981) is:

$$F(\varepsilon, f) = \left[1 + \varepsilon^{-1}(2\pi f)^6\right]^{-1} \quad (3.1)$$

where frequency response F is a function of smoothing factor ε and signal frequency f. Based on Equation (3.1), Fig. 3.1 illustrates frequency response curves of the Vondrak filter for different smoothing factors.

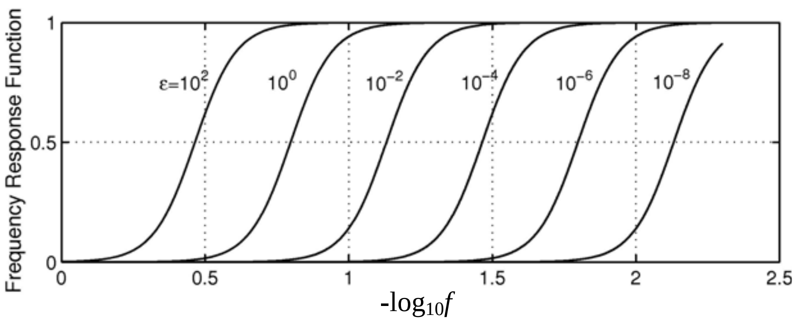

Fig. 3.1 Examples of frequency response of the Vondrak filter.

It is seen from Fig. 3.1 that for different smoothing factors, the curves are almost identical with a shift along the horizontal axis, reflecting the filtering properties of the filter. Signals with periods of -log$_{10}f$ where $F = 1$ remain in the filtered curves, while those where $F = 0$ are completely filtered out. As a result of a fact that signals where $0 < F < 1$ are partially filtered out, the corresponding frequency band is called the truncation frequency band. More details of the Vondrak filter can be found in Chapter 4.

Based on the characteristics of one-side filter, Vondrak bandpass numerical filter can be implemented by giving central frequency, f_0, and range of bandpass frequency band, Δf, (Vondrak, 1977). Figure 3.2 shows the Vondrak bandpass filter.

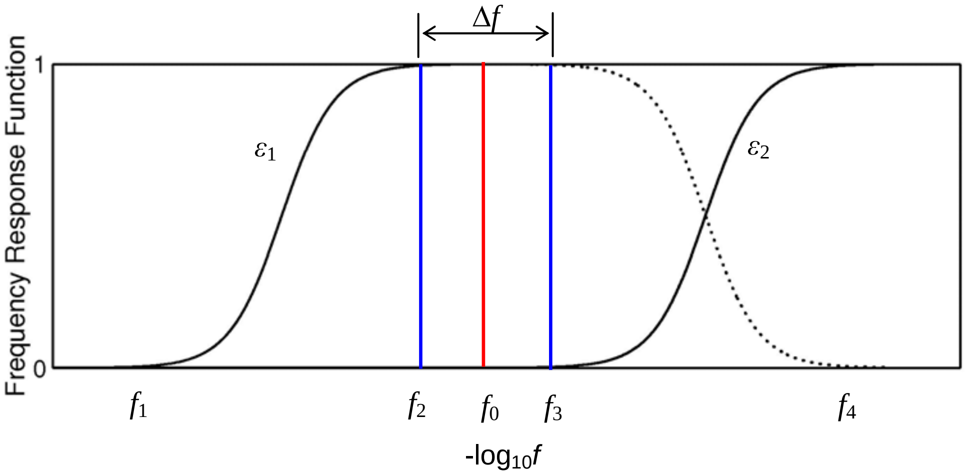

Fig. 3.2 Schematic representation of the Vondrak bandpass filter.

Converting Equation (3.1) into a function of ε and F, we can express the common logarithm of frequency f as:

$$\log_{10} f = \log_{10}(1-F)/6 + \log_{10}\varepsilon/6 - \log_{10} 2\pi - \log_{10} F/6 \tag{3.2}$$

Suppose $F(\varepsilon_1, f_1) = 0.01$, $F(\varepsilon_1, f_2) = 0.99$, $F(\varepsilon_2, f_3) = 0.01$ and $F(\varepsilon_2, f_4) = 0.99$ respectively, where ε_1 and ε_2 are smoothing factors corresponding to two border values of the frequency band. Therefore Equation (3.2) can be written as:

$$\begin{cases} \log_{10} f_1 = -0.47 + \log_{10} \varepsilon_1 / 6 \\ \log_{10} f_2 = -1.13 + \log_{10} \varepsilon_1 / 6 \\ \log_{10} f_3 = -0.47 + \log_{10} \varepsilon_2 / 6 \\ \log_{10} f_4 = -1.13 + \log_{10} \varepsilon_2 / 6 \end{cases} \tag{3.3}$$

Based on Equation (3.3), the central frequency f_0 and the frequency range Δf can be calculated by

$$\log_{10} f_0 = \log_{10} f_2 f_3 / 2 = \log_{10} f_1 f_4 / 2 = -0.80 + \log_{10} \varepsilon_1 \varepsilon_2 / 12 \tag{3.4}$$

$$\Delta f = \log_{10}(f_2 / f_3) = -0.66 + \log_{10}(\varepsilon_1 / \varepsilon_2) / 6 \tag{3.5}$$

Then the values of ε_1 and ε_2 are obtained:

$$\log_{10} \varepsilon_1 = 6.78 + 6 \log_{10} f_0 + 3\Delta f \tag{3.6}$$

$$\log_{10} \varepsilon_2 = 2.82 + 6 \log_{10} f_0 - 3\Delta f \tag{3.7}$$

By filtering the observational data twice using the smoothing factors determined by Equations (3.6) and (3.7) respectively and noting the difference between them, the result of the Vondrak bandpass filter can be achieved.

It is seen from Fig. 3.2 that the difference, $F(\varepsilon_1)$ - $F(\varepsilon_2)$, involves not only the desired signals determined by f_0 and Δf but also those that partially remain due to the effects of the truncation frequency band (e.g. signals with frequencies between f_1 and f_2). It is considered that signals, enveloped between the left branch of the graph and the right dotted curve, are maintained after filtering.

When Δf is negative, that is $\log_{10}f_2 < \log_{10}f_3$, a narrow filter is derived. The amplitude of the desired signal with frequency f_0 is depressed due to the effects of the truncation frequency band. In particular, when Δf equals zero, then $f_0 = f_2 = f_3$ and the difference, $F(\varepsilon_1, f_0) - F(\varepsilon_2, f_0)$, reaches its maximum value of 0.98 and up to 2% amplitude attenuation of the signal in the center of the frequency band occurs. When Δf is positive, that is $\log_{10}f_2 > \log_{10}f_3$, the signal with frequency f_0 remains completely and at the same time the other signals with frequencies contiguous to f_0 are partially maintained.

When the Vondrak bandpass filter is applied to structural vibration monitoring, the central frequency f_0 can be determined by the dominant natural frequency of the observational series, which may be identified from the design of the structure or by applying time-frequency analyses, e.g., the Fast Fourier Transform (FFT). In this case, $\Delta f > 0$ is select to maintain the amplitude of the vibration signals. If the dominant natural frequencies of the data series fall over a frequency band, the cut-off frequencies at the two ends of the frequency band, e.g. f_2 and f_3 ($f_2 > f_3$) in Fig. 3.2 can be chosen, and then determine f_0 and Δf using Equations (3.4) and (3.5).

3.2.2 Wavelet Filter

Wavelet transform is used to represent or approach a signal with a family of wavelet functions (or wavelet basis) generated from a prototype function (called a “mother” wavelet) by translation and dilation operations (Teolis, 1998). The wavelet transform of a signal f is (Daubechies, 1992):

$$W_f(a,b) = < f, \Psi_{a,b} > = \int_R f(t) \frac{1}{\sqrt{|a|}} \overline{\Psi}(\frac{t-b}{a})\, dt \tag{3.8}$$

where $\Psi(t)$ is the wavelet basis; a and b represent the dilation and translation parameters respectively ($a, b \in R$ and $a \neq 0$); and $\overline{\Psi}(t)$ is the complex conjugate of $\Psi(t)$.

The signal can be reconstructed from

$$f = \frac{1}{C_\Psi} \int_R \int_R < f, \Psi_{a,b} > \Psi_{a,b}(t) \frac{dadb}{a^2}, \tag{3.9}$$

provided that the constant C_Ψ satisfies the following admissibility condition

$$0 < C_\Psi = \int_R \frac{|F\{\Psi\}(\omega)|^2}{|\omega|} d\omega < \infty \tag{3.10}$$

where $F\{\Psi\}$ is the Fourier transform of the mother wavelet $\Psi(t)$ and ω is the signal frequency.

In practical applications such as signal processing, a finite number of data points are usually given. A discrete version of the wavelet transform is then required, where discrete dilation and translation parameters are used. Here the discrete dyadic wavelet transform based on Mallat algorithm (Mallat, 1988) is applied to GPS observables. It performs the analysis through recursive action of conjugated filters and gives a discrete multiresolution description of continuous-time signals. Details of discrete dyadic wavelet transform and wavelet multiresolution analysis can be found in Chapter 4.

The procedure for removing multipath errors or extracting vibration signals using the wavelet filter involves three main steps.

Step 1: Decomposition

A signal can be decomposed into different signal levels representing different frequency bands by using the discrete dyadic wavelet transform. We take the discrete Meyer wavelet as an example and show the central frequencies relative to each of the decomposition levels in Table 3.1.

Table 3.1 Central frequencies of Meyer wavelet for data series with a sampling rate of 10 Hz.

Level	1	2	3	4	5	6	7	8	9
Freq. (Hz)	3.361	1.680	0.840	0.420	0.210	0.105	0.053	0.026	0.013

With the information of central frequencies and the aid of time-frequency analysis or a prior knowledge of structure design, the vibration signal levels can be identified.

Step 2: Denoising

Wavelet-based denoising can be implemented by thresholding (Donoho, 1995), singularity detection (Mallat and Hwang, 1992; Hsung et al., 1999) and removing high-frequency oscillation (Xiong et al., 2005). In this chapter, the vibration signals are extracted with the last method by keeping the coefficients of the vibration signal levels unchanged and setting the coefficients of the other decomposition levels at zero.

Step 3: Reconstruction

The modified wavelet coefficients obtained in Step 2 can be assembled back into the signal through upsampling and filtering. This process is termed reconstruction.

3.2.3 Adaptive FIR Filter

An adaptive filter has the capability of continuously adjusting and updating the filter coefficients by adaptive algorithms based on the previous obtainable parameters to improve or optimize their performances. Since the vibration signals, multipath signals and GPS noise tend to fall in the same range of frequencies and the noise varies in time, it is therefore preferable to use an adaptive filter rather than a fixed filter in structural vibration monitoring (Ge et al., 2000). An adaptive FIR filter based on the recursive least-squares (RLS) algorithm is employed in this study to mitigate multipath effects and to derive vibrations from coordinate series.

An adaptive FIR filter, in general, consists of two basic processes:

- A filtering process to compute an output in response to an input signal and to generate an estimation error by computing this output with a desired response.

- An adaptive process for the adjustment of the parameters of the filter in accordance with the estimation error.

The combination of two processes working together constitutes a feedback loop, as illustrated in Fig. 3.3.

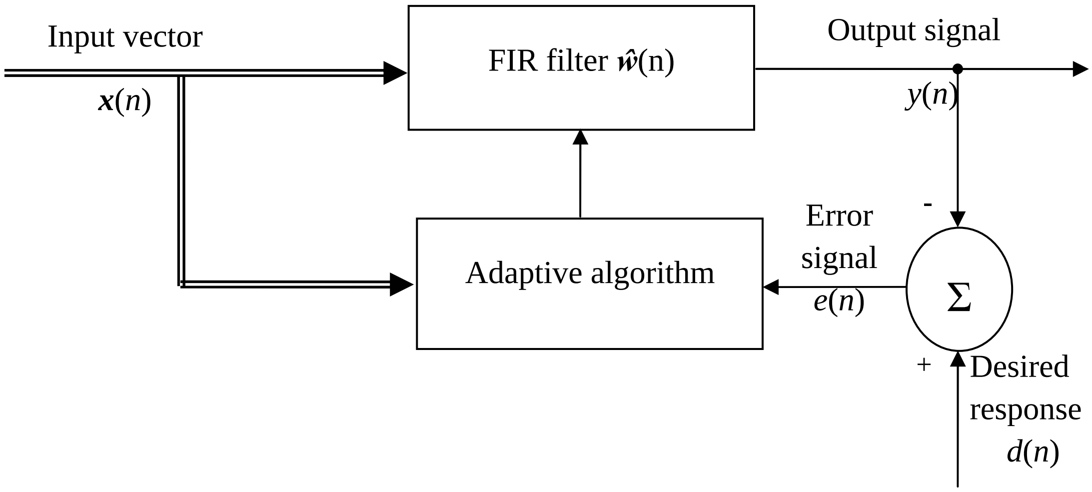

Fig. 3.3 A block diagram of an adaptive FIR filter.

The overall filter output of Fig. 3.3 can be expressed as:

$$y(n) = \hat{\boldsymbol{w}}(n)\boldsymbol{x}(n) \tag{3.11}$$

where the tap-weight estimate vector $\hat{\boldsymbol{w}}(n)$ is a random vector and $\boldsymbol{x}(n)$ is the tap-input vector. Also the estimation error is given by

$$e(n) = d(n) - y(n) \tag{3.12}$$

where $d(n)$ is the input desired response. The estimation criterion of the RLS is a least-squares time average that takes into account all the estimation errors up to current time instant n as follows (Haykin 2002):

$$\varepsilon(n) = \sum_{i=0}^{n} \lambda^{n-i} e^{2}(i) \tag{3.13}$$

where the forgetting factor λ is introduced to better track any changes in the signal characteristics. For stationary signals, λ should be chosen as unity. Otherwise, λ should be smaller than unity to track the nonstationary part of the signals (Akay, 1994).

The optimal filter weight, $\hat{\boldsymbol{w}}(n)$, can be obtained by taking the derivation of Equation (3.13) with respect to the filter weight and setting the derivation at zero. Thus the filter weight can be updated using the following recursive equation

$$\hat{\boldsymbol{w}}(n) = \hat{\boldsymbol{w}}(n\text{-}1)+\boldsymbol{g}(n)\xi(n) \tag{3.14}$$

where $\boldsymbol{g}(n) = \dfrac{\lambda^{-1}\boldsymbol{P}^{-1}(n-1)\boldsymbol{x}(n)}{1+\lambda^{-1}\boldsymbol{x}^{T}(n)\boldsymbol{P}^{-1}(n-1)\boldsymbol{x}(n)}$;

$\xi(n) = d(n)$ - $\hat{\boldsymbol{w}}^{T}(n\text{-}1)\boldsymbol{x}(n)$; and

$\boldsymbol{P}(n) = \sum_{i=1}^{n} \lambda^{n-i} \boldsymbol{x}(i)\boldsymbol{x}^{T}(i)$.

When applying the adaptive FIR filter to structural vibration monitoring, two GPS measurement series of consecutive days, dynamic and static, with the same length are required (Chan et al., 2005). The dynamic signal, $d(n)$, as the desired response of Fig. 3.3 can be expressed as

$$d(n) = s(n) + \delta_{mp}(n) \tag{3.15}$$

where $s(n)$ is the vibration signal and $\delta_{mp}(n)$ is the multipath error. It is assumed that both are uncorrelated with each other.

The static signal, r(n), is the multipath $\delta'_{mp}(n)$ that is significantly correlated with $\delta_{mp}(n)$ of Equation (3.15), due to the repeating property of GPS multipath signals. That is

$$r(n) = \delta'_{mp}(n) \tag{3.16}$$

Through the adaptive FIR filtering, an estimate of multipath $\hat{\delta}_{mp}(n)$ is output as a coherent component that is correlated between the primary (dynamic) and the reference (static) signals. Desired vibrations $\hat{s}(n)$ as an incoherent component can then be obtained by subtracting the filter output from the dynamic signal.

3.3 GPS Field Experiments

A motion simulation table (see Fig. 3.4) was designed for simulating various frequencies and amplitudes of vibration in order to verify the accuracy of GPS when it is applied to structural vibration monitoring. It consists of a movable platform, two servomotors, two ball screws, an electronic control system, a 16-channel data acquisition system, a power terminal box, a supporting frame and a desktop for motion control and data acquisition.

For time synchronization between GPS and the motion simulation table, a GPS receiver (Ashtech GG24) is connected to the computer to synchronize the computer clock with the atomic clock. The four legs of the supporting frame can be adjusted to make the movable table horizontal. The servomotors are controlled by the computer to simulate various vibrations. The table is capable of generating sinusoidal waves, circular motions, white noise and other waveforms defined by time histories of input wave in two perpendicular horizontal directions. The precision of the simulated amplitudes is better than 0.1 mm.

Fig. 3.4 Motion simulation table.

Three field experiments were carried out on a test site in Pak Shek Kok, Hong Kong from 30 to 31 January 2004. Two Leick 9500 dual-frequency GPS receivers and two AT202/302 antennae were used with a baseline length of about 11 m at a sampling rate of 10 Hz. The cutoff elevation angle for GPS observations was set to 15º. In the tests, one antenna was attached to the movable platform of the motion simulation table as the rover station and another was fixed on a tripod as the reference station. On the first day, the two GPS antennae were kept still for an hour to determine precisely the position of the movable platform relative to the reference station before the simulated vibrations were introduced. During the second day's test the antennae were kept still.

A flow chart showing the processing procedure for analyzing the filter performance is illustrated in Fig. 3.5. Firstly, DD carrier-phases computed from the known coordinates are subtracted from those computed from the observations in order to obtain raw DD residuals. Secondly, time series of the raw DD residuals is filtered by using digital filters to achieve filtered DD residuals. The raw and filtered DD residuals are then used to estimate the coordinates of the rover station based on a single epoch algorithm. Finally, the coordinate series thus obtained are compared with the true values of the simulated vibrations to investigate the filter performance for separating the vibration signals from the multipath effects.

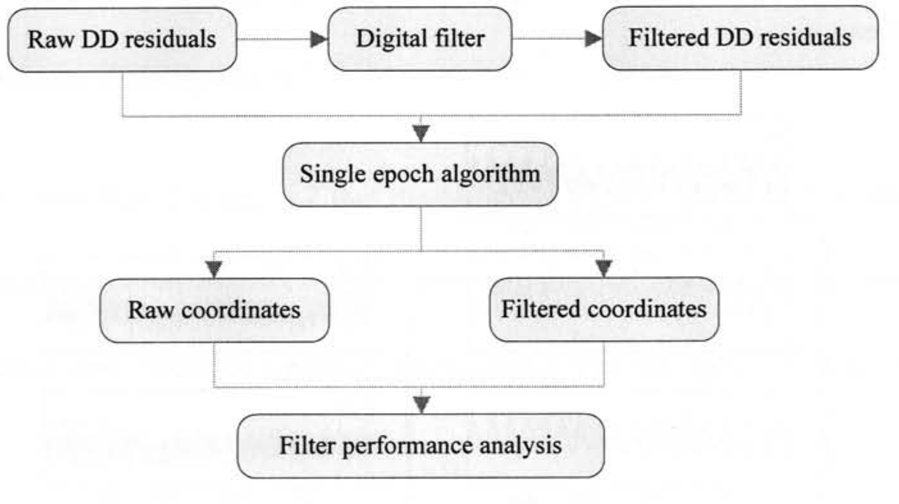

Fig. 3.5 Computation flow chart for analyzing the filter performance.

3.4 Comparative Analyses and Results

Experiment 1

The simulated vibrations are circular motion with frequency and amplitude of 0.075 Hz and 2 mm respectively. There are six satellites in view and 2400-second data collection is carried out. The satellite pair PRNs 11-8 (PRN 11 is selected as reference satellite due to its highest elevation angle) is taken as an example and show the time series of the raw and filtered DD residuals, and their differences in Fig. 3.6. Comparisons of the coordinate series before and after filtering with the theoretical vibration values in the *X*, *Y* and *H* directions are shown in Fig. 3.7. The *X* and *Y* coordinates refer to the Easting and Northing directions respectively in a Universal Transverse Mercator (UTM) system, while *H* coordinate gives the ellipsoidal height. For easy interpretation, the mean coordinates have been removed from the coordinate time series.

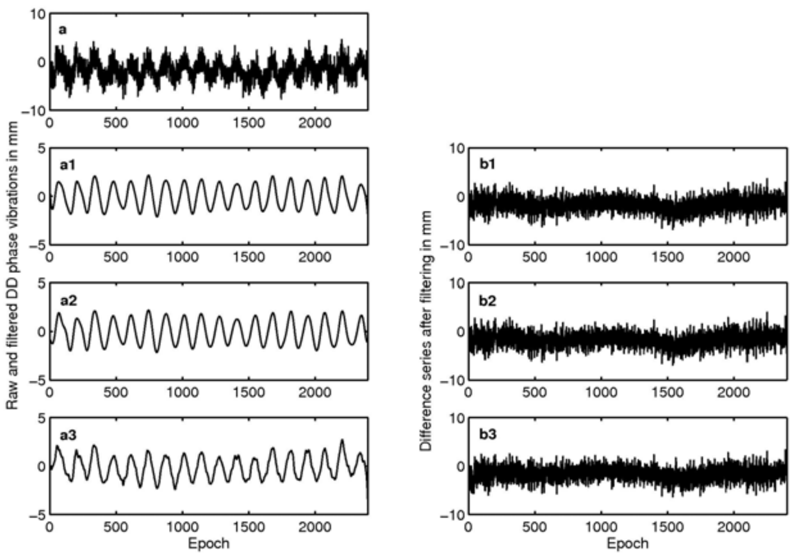

Fig. 3.6 a Raw DD residuals; **a1**, **a2**, **a3** filtered DD residuals based on Vondrak,

wavelet and adaptive FIR filtering methods respectively; and **b1**, **b2**, **b3** difference series between raw and filtered values (Experiment 1).

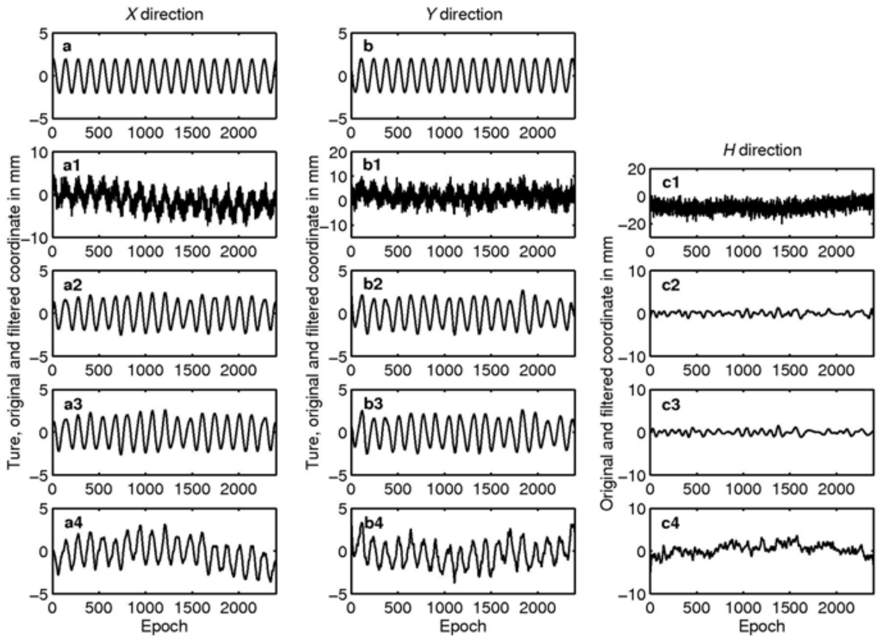

Fig. 3.7 a, **b** True vibrations of *X* and *Y* directions; **a1**, **b1**, **c1** original coordinates of *X*, *Y* and *H* directions; **a2**, **b2**, **c2** Vondrak filtered coordinate series; **a3**, **b3**, **c3** wavelet filtered coordinates; and **a4**, **b4**, **c4** adaptive FIR filtered coordinates for the three directions (Experiment 1).

It is seen from Figs. 3.6 and 3.7 that the Vondrak, wavelet and adaptive FIR filters can be used to separate the vibration signals from the multipath errors and noise. The GPS accuracy of tracking dynamic displacement can be up to 2 mm after the filtering.

Experiment 2

Circular motion with frequency of 0.5 Hz and amplitude of 20 mm is simulated in this experiment. Five satellites are visible and 2400-epoch observations are collected. Figure 3.8 shows the coordinate series before and after filtering and the true values of the simulated vibrations. It is obvious from visual inspection of Fig. 3.8 that the adaptive FIR filtered coordinates in *H* direction largely retain the tendency of the original coordinate series in the same direction. It is considered that the tendency of low frequency vibrations results from the residual multipath effects due to reflection or diffraction of nearby obstacles.

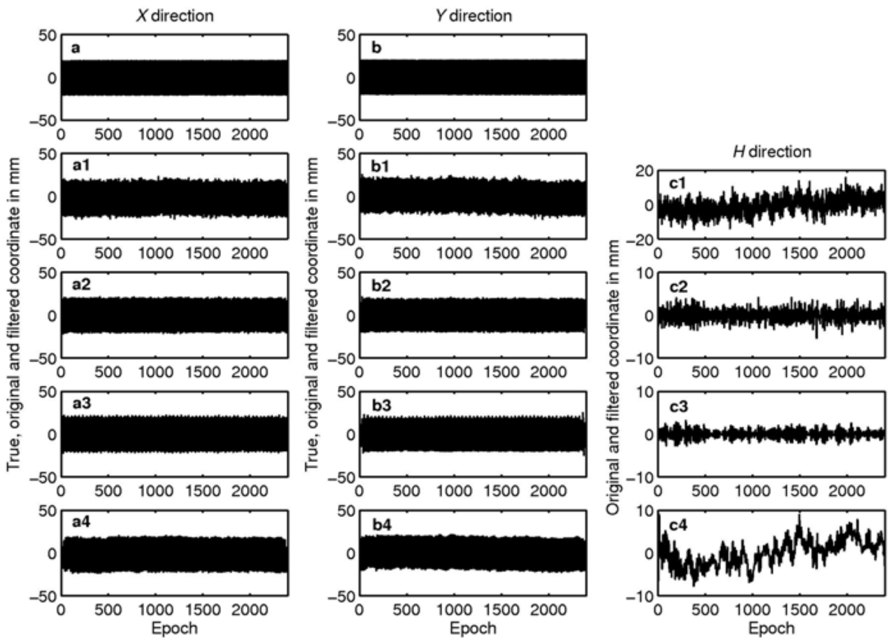

Fig. 3.8 Same as those described in Fig. 3.7, except for Experiment 2.

Experiment 3

A motion with frequency from 0.025 to 0.5 Hz and amplitude from 0 to 18 mm is simulated. Six visible satellites and 2400-epoch observational data are used in this experiment. For clarity, the true, original and filtered coordinates for the first 800 epochs are depicted in Fig. 3.9.

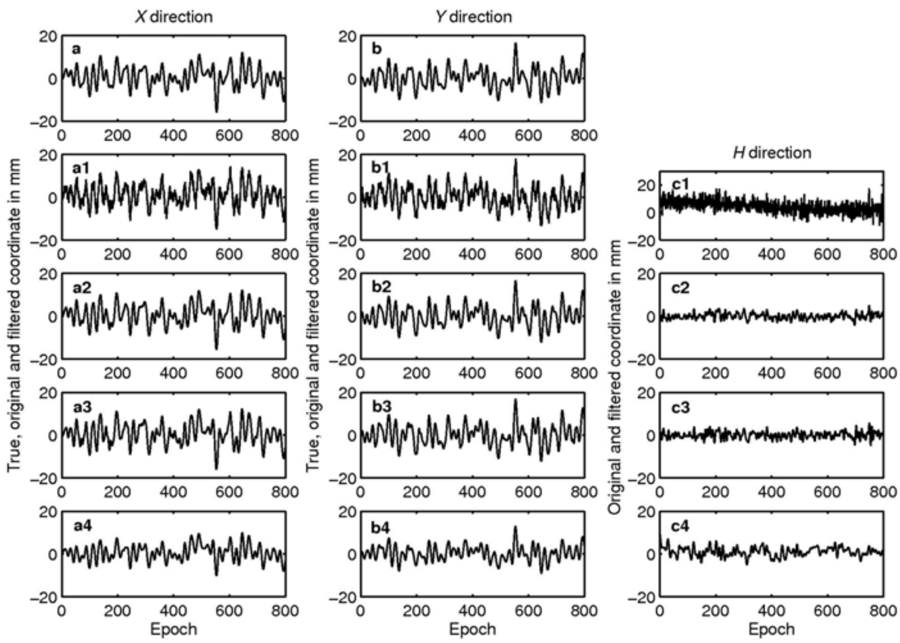

Fig. 3.9 Same as those described in Fig. 3.7, except for Experiment 3.

It is seen from Fig.3.9 that the measurement accuracy of GPS for complex signals with varying frequencies and amplitudes can be improved with any of the filters.

3.4.1 Comparison of Precision

To evaluate the filter performance for mitigating multipath or extracting the vibrations in a quantitative manner, we note the difference between the GPS determined (either original or filtered) coordinates and the true vibrations based on an epoch-by-epoch estimation. Then the root mean square (RMS) values are calculated by

$$\mathrm{RMS} = \left[\frac{1}{n} \sum_{i=1}^{n} (x_i - t_i)^2 \right]^{\frac{1}{2}} \tag{3.17}$$

where n is the total number of samples; x_i denotes the original or filtered coordinates at epoch *i*; and t_i is the true vibrations. Minimum detectable vibrations estimated by 3 times RMS (at the 99.7% confidence level) with and without applying the filtering methods are listed in Table 3.2. To show the effectiveness of the filters, Table 3.3 shows the percentage improvements in accuracy by comparing the RMS values of the coordinate series before and after filtering.

Table 3.2 Minimum detectable vibrations before and after filtering at the 99.7% confidence level in the three directions (unit: mm).

	Experiment 1			Experiment 2			Experiment 3		
	X	*Y*	*H*	*X*	*Y*	*H*	*X*	*Y*	*H*
Before Filtering	6.3	8.6	9.9	8.5	7.2	13.3	5.1	10.3	18.7
Vondrak	0.9	1.1	1.5	5.8	4.2	4.3	2.4	2.2	4.8
Wavelet	0.9	1.0	1.5	6.1	5.4	3.0	2.6	2.4	5.4
Adaptive FIR	2.7	2.6	3.7	7.3	5.4	9.1	4.4	5.4	7.6

It is seen from Table 3.2 that the minimum detectable vibrations before the filtering range from 5.1 to 18.7 mm; the values are 0.9-5.8 mm after applying the Vondrak filter, 0.9-6.1 mm after the wavelet filtering, and 2.6-9.1 mm for the adaptive FIR filter.

Table 3.3 Accuracy improvements after filtering for the three directions (unit: %).

	Experiment 1			Experiment 2			Experiment 3		
	X	*Y*	*H*	*X*	*Y*	*H*	*X*	*Y*	*H*
Vondrak	86	87	85	32	41	68	54	79	74
Wavelet	85	88	85	28	25	77	49	77	71
Adaptive FIR	58	70	63	14	25	31	14	47	59

It is seen from Table 3.3 that the accuracy improvements after applying the Vondrak and wavelet filters are greater than those of the adaptive FIR filter, especially for multi-frequency and multi-amplitude signals in Experiment 3. The average improvements in accuracy after the Vondrak and wavelet filtering are 56%, 66% and 77% for *X*, *Y* and *H* directions respectively.

The results in Tables 3.2 and 3.3 indicate that the GPS accuracy for monitoring the structural vibrations can be improved by any of the three filters. The performances of the Vondrak filter are almost the same as those of the wavelet filter in aspects of the minimum detectable vibrations and the accuracy improvements. Both filters are superior to the adaptive FIR filter.

3.4.2 Comparison of Filtering Methods

The different fundamentals (e.g. frequency response) or algorithms of filters may result in different procedures and parameters for vibration extraction. The advantages and disadvantages of each of the filters with respect to certain aspects such as parameter selection and computation efficiency will be analyzed in the next subsection.

Vondrak Bandpass Filtering

Figure 3.10 illustrates the power spectrum density (PSD) estimates of the raw DD residuals series for Experiments 2 and 3 using Welch's method (Welch, 1967).

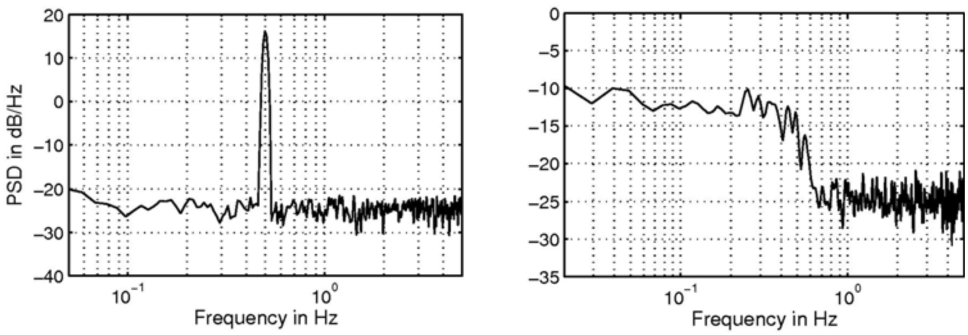

Fig. 3.10 PSD of raw DD residuals for Experiments 2 (*left panel*) and 3 (*right panel*).

It can be seen from Fig. 3.10 that the estimated frequency components are almost the same as the simulated 0.5 Hz in Experiment 2 and 0.025-0.5 Hz in Experiment 3. Thus the central frequency f_0 of Experiment 2 and the frequency range Δf of Experiment 3 can be determined. To effectively separate the vibrations from the effects of other errors, the frequency ranges in Experiments 1 and 2 are selected as 0.1 due to the fact that the amplitude of the signal with frequency $f_0/4$ after filtering is only about 5% of that before filtering. The merits and shortcomings of the Vondrak filter will be presented afterwards.

Wavelet Filtering

There are two important factors to consider when applying the wavelet filter to structural vibration monitoring. One is the selection of wavelet basis; the other is the determination of vibration signal levels. Different wavelets perform differently. For example, Haar wavelets are discontinuous and consequently poorly localized in frequency (Wan and Wei, 2000); Daubechies and Coiflet wavelets are orthogonal and compactly supported but asymmetrical (Sun et al., 2003); Meyer wavelets have characteristics of not only rapid decay and infinite differentiability in the time domain, but also compact support in the frequency domain (Pinsky, 2002). For analyzing multipath signals within a limited frequency spectrum, compact support in the frequency domain is a desirable feature. Therefore the symmetric orthogonal discrete Meyer wavelet is chosen as the wavelet basis.

Figure 3.11 shows the 8-level Meyer wavelet decomposition of the DD residuals for Experiment 3, where S is the raw DD residuals; $a8$ and $d8$-$d1$ denote the approximation and details respectively. As the wavelet transform is linear, the signal after wavelet decomposition can be represented by $S = a8 + d8 + d7 + \dots + d1$.

It is seen from Fig. 3.11 that the extrema and amplitudes of the noise decrease with the increase of the decomposition level. It is therefore considered that the signals exist at the higher levels. Based on the PSD estimates of Experiment 3 (see Fig. 3.10) and the central frequencies relative to each of the decomposition levels (see Table

3.1), the vibration signals falling between *d*4 and *d*8 can be determined. For Experiments 1 and 2, the wavelet-decomposed signal levels are the details of *d*6-*d*7 and *d*4 respectively.

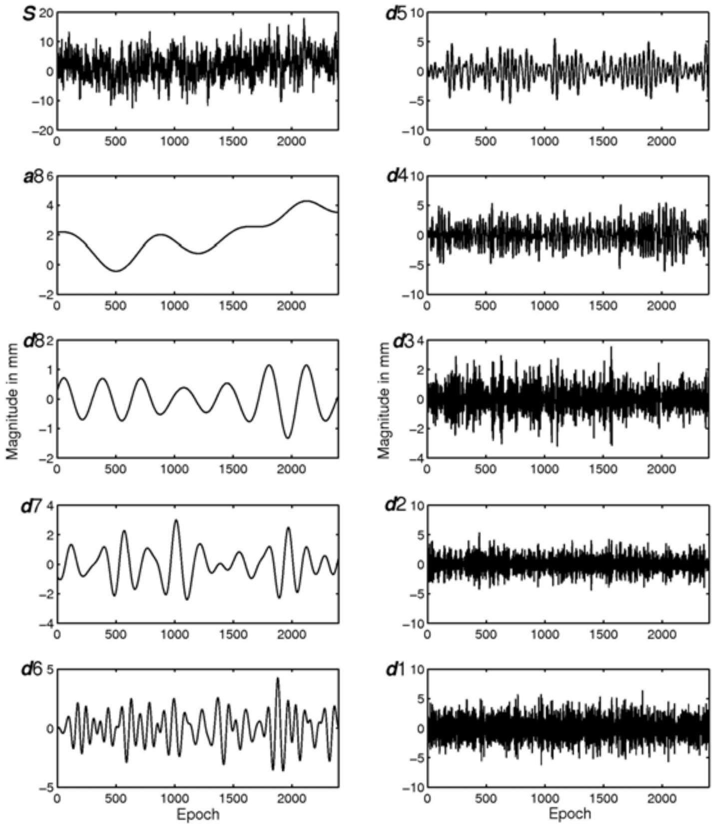

Fig. 3.11 Wavelet decomposition of DD residuals for Experiment 3: ***S*** raw DD residuals; ***a*8** approximation; ***d*8**-***d*1** details from levels 8 to 1.

It can be seen from the analysis above that the Vondrak and wavelet filters are not only easy to implement but also computationally efficient without calculation iteration. However, the implementation of both filters requires the time-frequency analysis to determine the dominant natural frequencies of the vibrations.

Adaptive FIR Filtering

Figure 3.12 illustrates the procedure of adaptive FIR filtering, taking Experiment 1 as an example. The static GPS measurements are required to separate the multipath effects from the dynamic GPS measurements. It is seen from Fig. 3.12 that the vibration signals in subplot *e* are contaminated by some residual errors. It is considered that the errors may be caused by the effects that the multipath signals are not exactly repeatable between the two consecutive days. Further analysis of GPS multipath repeatability can be found in Chapter 5.

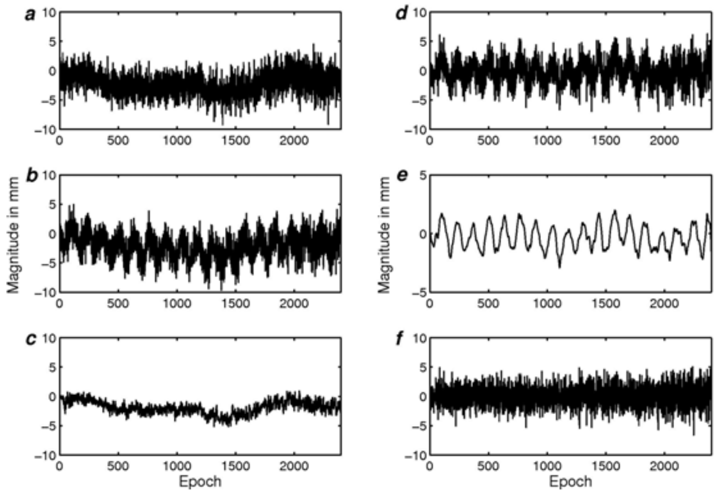

Fig. 3.12 Extracting vibrations based on adaptive FIR filters for Experiment 1: ***a*** static DD residuals; ***b*** dynamic DD residuals; ***c*** multipath signals as coherent component of filter output; ***d*** vibrations and noise as incoherent component of filter output; ***e*** vibration signals obtained by a lowpass filter with cutoff frequency of 1 Hz, and ***f*** difference between ***d*** and ***e***.

Although its fast convergence rate and stable filter characteristic, the RLS algorithm in the adaptive FIR filtering may be computationally costly since it requires M^2 (M is the filter order) operations per time update.

3.5 Conclusions and Recommendations

A Vondrak bandpass filter has been proposed and applied to structural vibration monitoring. The performance of the proposed filter retrieving vibration signals from multipath effects has been compared with those of the wavelet and adaptive FIR filters. Based on the analysis results with real GPS observations, the following conclusions can be drawn:

(1) The GPS accuracy of tracking dynamic displacement and complex signals with varying frequencies and amplitudes can be improved by any of the filters. The measurement accuracy in amplitude can reach 2 mm.

(2) The Vondrak bandpass filter is effective in separating structural vibrations from multipath effects. Its performance is similar to that of the wavelet filter in terms of the minimum detectable vibrations and the accuracy improvements. The minimum detectable vibrations range from 0.9 to 6.0 mm for both of the filters and the accuracy improvements on average are 56%, 66% and 77% for *X*, *Y* and *H* directions respectively.

(3) The results of experiments in this chapter show that the Vondrak bandpass filter and wavelet filter are superior to the adaptive FIR filter. The implementation of the adaptive FIR filter is computationally costly and requires static GPS observations; whereas the implementation of the other

two filters is computationally efficient, but requires time-frequency analysis or a prior knowledge of structure design.

Recommendations are presented here for selecting filters and filter parameters in different situations, when filters are applied to retrieve structural vibrations from multipath effects. If a signal with a dominant natural frequency exists in the observational series or a vibration signal with a certain frequency is to be extracted, the Vondrak bandpass filter can be used, avoiding the estimation of wavelet-decomposed vibration levels. In this situation, the central frequency f_0 can be chosen as the dominant natural frequency or the frequency to be analyzed. The frequency range Δf can be selected as 0.1 to maintain the vibration amplitudes and effectively separate the vibration signals from other errors. If the vibration signals fall over a frequency range, either the wavelet or the Vondrak bandpass filter can be utilized.

[blank page]

Chapter 4

Establishing Multipath Model and Filtering GPS Time-Series with Cross-Validation Based Filters

4.1 Introduction

In precise GPS applications, such as deformation monitoring, the geometry relating the GPS satellites, reflective surface and the antenna does not usually change significantly between consecutive sidereal days. Therefore, GPS multipath signals also repeat largely themselves over the same time period (Genrich and Bock, 1992; Hoffman-Wellenhof et al., 2001; Han and Rizos, 1997; Leick, 2004), although variations do occur under certain conditions such as when the surface moisture content changes or the satellite orbits are significantly altered (Kim et al., 2003; Forward et al., 2003). Some research has been carried out to mitigate GPS multipath effects based on the sidereal day-to-day repeating characteristics of GPS multipath signals (Elósegui et al., 1995; Radovanovic, 2000; Wübbena et al., 2001; Park et al., 2004). When taking advantage of this repeating property, an accurate multipath model is necessary to remove multipath errors from subsequent GPS observations.

As discussed in Chapter 3, the Vondrak and wavelet filters can be extensively used to reduce the multipath effects. However, the implementation of both filters requires a priori knowledge of signal frequency or time-frequency analysis, e.g., the Fast Fourier Transform (FFT). These approaches may become questionable when the a priori frequency is unknown or the signal-to-noise ratio (SNR) is low.

In this chapter, we propose to apply the method of cross-validation (Clark and Thompson, 1978; Breiman et al., 1984; Stone, 1974; Schumacher et al., 1997) combined with Vondrak (1977) or wavelet filter to separate signals from noise in a data series with no time-frequency analysis or a prior information. The proposed methods are applied to extract the multipath ‘signal’ based on GPS observations, and this signal is then used to make corrections to subsequent GPS observations. The Vondrak filter has a good signal resolution at the signal truncation frequency band, i.e., at the upper or lower limit of a frequency band. The wavelet filter has good localized time-frequency features. When the Vondrak or wavelet filter is combined with the method of cross-validation, a balance between data fitting and smoothing can be achieved in the filtering process, and the signals can be automatically identified from noise.

The proposed two data filtering methods will be firstly introduced; testing results with simulated data series and real GPS observations will be presented afterward.

4.2 Cross-Validation Vondrak Filter (CVVF)

4.2.1 Principles of Vondrak Filter

A series of observational data can be expressed as (x_i, y_i), $i = 1, 2, \ldots, N$, where x_i and y_i are the measurement epochs and the measurements respectively. The basic concept of the Vondrak filter is to derive filter values under the following condition (Vondrak, 1977):

$$Q = F + \lambda^2 S \rightarrow \min, \tag{4.1}$$

where F expresses the fidelity of the filtered to the unfiltered values; S is the smoothness of the filtered curve and λ^2 is a unitless positive coefficient that controls the degree of filtering or the smoothness of the filtered series.

$$F = \sum_{i=1}^{N} p_i (y_i' - y_i)^2, \tag{4.2}$$

$$S = \sum_{i=1}^{N-3} (\Delta^3 y_i')^2, \tag{4.3}$$

where y_i' is the filtered value corresponding to measurement y_i, p_i is the weight of y_i; and $\Delta^3 y_i'$ is the third-difference of filter values based on a cubic Lagrange polynomial.

When the coefficient $\lambda^2 \rightarrow \infty$, $S \rightarrow 0$ and $F \rightarrow \min$, a smooth parabola will be derived, and the operation is called absolute smoothing. When $\lambda^2 \rightarrow 0$, $F \rightarrow 0$, the filtered values approach the measurements, a rough curve will result and the operation is called absolute fitting. Here $\varepsilon = 1 / \lambda^2$ is identified as the smoothing factor.

4.2.2 Solution of Vondrak Filtering

Provided that y_i' is the filtered value at time x_i, and all the points (x_i, y_i') lie on the curve defined by the continuous function $f(x)$, the quantity S can thus be expressed as (Vondrak, 1969)

$$S = \int_{x_1}^{x_n} \left[f'''(x) \right]^2 dx \tag{4.4}$$

where x_1 and x_n are arguments at border points of the curve and $f'''(x)$ denotes the third derivative of function $f(x)$. Since the analytical expression of the function is unknown, the value of $f'''(x)$ can be estimated by the discrete filtered values y_i'.

In deriving the solution, a cubic Lagrange polynomial $L_i(x)$ is fitted to four adjacent points (x_i, y_i'), (x_{i+1}, y_{i+1}'), (x_{i+2}, y_{i+2}') and (x_{i+3}, y_{i+3}') when considering points (x_{i+1}, y_{i+1}') and (x_{i+2}, y_{i+2}'). The expression of $L_i(x)$ is given by

$$\begin{aligned} L_i(x) = {} & \frac{(x - x_{i+1})(x - x_{i+2})(x - x_{i+3})}{(x_i - x_{i+1})(x_i - x_{i+2})(x_i - x_{i+3})} y_i' \\ & + \frac{(x - x_i)(x - x_{i+2})(x - x_{i+3})}{(x_{i+1} - x_i)(x_{i+1} - x_{i+2})(x_{i+1} - x_{i+3})} y_{i+1}' \\ & + \frac{(x - x_i)(x - x_{i+1})(x - x_{i+3})}{(x_{i+2} - x_i)(x_{i+2} - x_{i+1})(x_{i+2} - x_{i+3})} y_{i+2}' \\ & + \frac{(x - x_i)(x - x_{i+1})(x - x_{i+2})}{(x_{i+3} - x_i)(x_{i+3} - x_{i+1})(x_{i+3} - x_{i+2})} y_{i+3}'. \end{aligned} \tag{4.5}$$

The third derivative of Equation (4.5) can be expressed as

$$\begin{aligned} L_i'''(x) = {} & \frac{6}{(x_i - x_{i+1})(x_i - x_{i+2})(x_i - x_{i+3})} y_i' \\ & + \frac{6}{(x_{i+1} - x_i)(x_{i+1} - x_{i+2})(x_{i+1} - x_{i+3})} y_{i+1}' \\ & + \frac{6}{(x_{i+2} - x_i)(x_{i+2} - x_{i+1})(x_{i+2} - x_{i+3})} y_{i+2}' \\ & + \frac{6}{(x_{i+3} - x_i)(x_{i+3} - x_{i+1})(x_{i+3} - x_{i+2})} y_{i+3}'. \end{aligned} \tag{4.6}$$

Then the quantity S can be written as

$$\begin{aligned} S &= \sum_{i=1}^{N-3} \int_{x_{i+1}}^{x_{i+2}} \left[L_i'''(x)\right]^2 dx = \sum_{i=1}^{N-3} \left[L_i'''(x)\right]^2 (x_{i+2} - x_{i+1}) \\ &= \sum_{i=1}^{N-3} (a_i y_i' + b_i y_{i+1}' + c_i y_{i+2}' + d_i y_{i+3}')^2, \end{aligned} \tag{4.7}$$

where the coefficients a_i, b_i, c_i and d_i are

$$\begin{cases} a_i = \dfrac{6\sqrt{(x_{i+2} - x_{i+1})}}{(x_i - x_{i+1})(x_i - x_{i+2})(x_i - x_{i+3})} \\ b_i = \dfrac{6\sqrt{(x_{i+2} - x_{i+1})}}{(x_{i+1} - x_i)(x_{i+1} - x_{i+2})(x_{i+1} - x_{i+3})} \\ c_i = \dfrac{6\sqrt{(x_{i+2} - x_{i+1})}}{(x_{i+2} - x_i)(x_{i+2} - x_{i+1})(x_{i+2} - x_{i+3})} \\ d_i = \dfrac{6\sqrt{(x_{i+2} - x_{i+1})}}{(x_{i+3} - x_i)(x_{i+3} - x_{i+1})(x_{i+3} - x_{i+2})} \end{cases} \tag{4.8}$$

Put Equations (4.2) and (4.7) into Equation (4.1) to obtain the following formula

$$Q = \sum_{i=1}^{N} p_i (y_i' - y_i)^2 + \lambda^2 \sum_{i=1}^{N-3} (a_i y_i' + b_i y_{i+1}' + c_i y_{i+2}' + d_i y_{i+3}')^2. \tag{4.9}$$

To find such values y_i' which make Q minimum, the following condition needs to be satisfied

$$\frac{\partial Q}{\partial y_i'} = 0 \qquad i = 1,2,\ldots,N \tag{4.10}$$

According to the partial derivations of F and S with respect to y_i', a general expression fulfilling Equation (4.10) is given by

$$\sum_{j=-3}^{3} A_{j,i} y'_{i+j} = B_i y_i \qquad i = 1,2,\ldots,N \tag{4.11}$$

with $A_{j,i} = 0$ for $i + j \le 0$ or $i + j \ge N + 1$, where B_i is denoted by εp_i; i and j are the row and column numbers of the equation respectively. The index j is equal to zero at the main diagonal from which j is negative to the left and positive to the right. The coefficient matrix of Equation (4.11) is a seven-diagonal matrix, where each coefficient $A_{j,i}$ is calculated by

$$\begin{cases} A_{-3,i} = a_{i-3} d_{i-3} \\ A_{-2,i} = a_{i-2} c_{i-2} + b_{i-3} d_{i-3} \\ A_{-1,i} = a_{i-1} b_{i-1} + b_{i-2} c_{i-2} + c_{i-3} d_{i-3} \\ A_{0,i} = \varepsilon p_i + a_i^2 + b_{i-1}^2 + c_{i-2}^2 + d_{i-3}^2 \\ A_{1,i} = a_i b_i + b_{i-1} c_{i-1} + c_{i-2} d_{i-2} \\ A_{2,i} = a_i c_i + b_{i-1} d_{i-1} \\ A_{3,i} = a_i d_i \end{cases} \tag{4.12}$$

Equations (4.8) and (4.12) are used to form a set of linear equations as expressed in Equation (4.11). Solving the linear equations can obtain the filtered values.

4.2.3 Modification of the Vondrak Filter

For measurements with the same distribution of random errors, the smoothness of the filtered curves derived using a Vondrak filter should be the same. However, it can be concluded from Equations (4.1) that when the density or the interval of the observations is different, the smoothing factors are different for retaining the same smoothness of the filtered curves. As a consequence, the Vondrak filter can be modified by (Vondrak, 1977)

$$F = (N-3)^{-1}\sum_{i=1}^{N} p_i (y_i' - y_i)^2 \tag{4.13}$$

and

$$S = (x_{N-1} - x_2)^{-1}\sum_{i=1}^{N-3} (\Delta^3 y_i')^2 \tag{4.14}$$

where F is independent of the number of observations and S is independent of the length of the interval.

Once the smoothing factor is selected, whatever the density of the observations or the length of the interval is, filtered curves with the same smoothness are derived. The computation process described in Section 4.2.2 is easily converted to the modified one by using $a(x_{N-1} - x_2)^{-1/2}$, $b(x_{N-1} - x_2)^{-1/2}$, $c(x_{N-1} - x_2)^{-1/2}$, $d(x_{N-1} - x_2)^{-1/2}$ and $\varepsilon(N-3)^{-1}$ instead of the quantities a, b, c, d and ε, respectively. In addition, if the measure of the argument is changed the value of ε should also be changed to give the same result. The dimension of ε is the dimension of the argument powered to minus six.

The main advantages of the Vondrak filter are:

- No predefined fitting function is required;
- Filtered values at the two ends of the data series can be calculated;
- Applicable to data of equal and unequal intervals, and
- Capable of being used as a numerical filter for separating signals of different

frequencies (Zheng, 1988; Zheng and Luo, 1992).

4.2.4 Cross-Validation Applied to Vondrak Filter

The main purpose of filtering is to properly separate signals from noise. A pivotal issue in using the Vondrak filter is how to select the smoothing factor ε to remove random noise while at the same time retaining the useful signals. Here the method of cross-validation (Clark and Thompson, 1978; Breiman et al., 1984; Stone, 1974; Schumacher et al., 1997) is introduced for the purpose of selecting the smoothing factor.

The basic concept of cross-validation is to cross-validate the filtered results with data samples. The procedure of implementing the proposed method is composed of three steps:

Step 1: The observation series (x_i, y_i), $i = 1, 2, \ldots, N$ is randomly sampled into two parts: the filtering series (sample size = N_1), $(x_{1,i}, y_{1,i})$, $i = 1, 2, \ldots, N_1$, and the validation series (sample size = N_2, and $N_2 << N_1$), $(x_{2,i}, y_{2,i})$, $i = 1, 2, \ldots, N_2$. We use P_i to refer the ith division of the measurement.

Step 2: The filter values can be calculated from the Vondrak-filtered series using a given smoothing factor ε. The variance of the validation series relative to the filter values can then be calculated with

$$C(\varepsilon, P) = \frac{1}{N_2} \sum_{i=1}^{N_2} \left[y_{2,i} - f'(x_{2,i}) \right]^2, \tag{4.15}$$

where $f'(x_{2,i})$ are values derived by cubic spline interpolation of the filtered values for the $x_{2,i}$ epoch.

Step 3: Suppose that K different smoothing factors ε_k, $\varepsilon_k = 10^{-k}$, $k = 1, 2, \ldots, K$, are used. For each of the factors the measurement data is randomly sampled M times, denoted by P_j, $j = 1, 2, \ldots, M$. Thus, M variances $C(\varepsilon_k, P_j)$ can be obtained. The mean value of the M variances for each smoothing factor can be finally derived

$$\overline{C}(\varepsilon_k, P) = \frac{1}{M}\sum_{j=1}^{M} C(\varepsilon_k, P_j)\,. \tag{4.16}$$

The ε_k value that makes the smallest $\overline{C}(\varepsilon_k, P)$ is considered the optimal smoothing factor.

The validation sample size used in the analysis will only be 5% of the data series in order not to degrade the resolution and to maintain the high-frequency signals in the measurement data. The number of divisions is $M = 40$ to ensure statistical significance. In addition, to prevent edge effects due to poorer filtering results at the ends of a data series, about 70% of the data from the middle of the series are selected for cross-validation.

For convenience of reference, the proposed Vondrak filter will be termed the cross-validation Vondrak filter (CVVF). The term seems appropriate since the CVVF uses the optimal smoothing factor determined with the cross-validation method already described.

4.3 Cross-Validation Wavelet Filter (CVWF)

As discussed in Chapter 3, a wavelet family associated with the mother wavelet ψ can be generated by two operations: dilation and translation. The dilation parameter, *a*, and translation parameter, *b*, indicate the width and location of the moving wavelet window in the wavelet transform respectively. The wavelet transform can provide a time-frequency representation of the signal and allow the components of a non-stationary signal (e.g, GPS signal) to be analyzed.

4.3.1 Discrete Dyadic Wavelet Transform

When considering the computational efficiency, dyadic *a* and *b* values are generally used, i.e.

$$a = 2^m; \qquad b = n2^m \tag{4.17}$$

where *m* and *n* are integers. For some particular choices of $\Psi(t)$, there exists a corresponding discrete wavelet $\Psi_{m,n}$ that has good time-frequency localization properties such that

$$\Psi_{m,n}(t) = 2^{-m/2}\Psi(2^{-m}t - n), \tag{4.18}$$

forms an orthonormal basis for $L^2(R)$. Using the orthonormal basis, any $f(t) \in L^2(R)$ can be expressed as

$$f(t) = \sum_{m,n=-\infty}^{+\infty} \alpha_{m,n} \Psi_{m,n}(t) \tag{4.19}$$

where the discrete wavelet coefficient $\alpha_{m,n}$ is defined by

$$\alpha_{m,n} = \int_R f(t)\overline{\Psi}_{m,n}(t)dt \tag{4.20}$$

The wavelet transform defined by Equations (4.17) to (4.20) is the discrete dyadic wavelet transform (Teolis, 1998). It consists of decomposing a signal into components at several frequency levels that are related to each other by powers of two.

4.3.2 Wavelet Multiresolution Analysis

The basic concept of multiresolution analysis is to analyze the signal at different scales (or resolutions) by using filters (Mallat, 1988; Debnath, 2002). In the wavelet multiresolution analysis, a signal can be decomposed into its approximations and details. The detail at level *m* is defined as

$$D_m(t) = \sum_{n \in Z} \alpha_{m,n} \Psi_{m,n}(t)\,, \tag{4.21}$$

where *Z* is the set of positive integers. The approximation at level *M* is defined as the sum of the details up to that level, i.e.

$$A_M(t) = \sum_{m > M} D_m(t)\,. \tag{4.22}$$

The signal $f(t)$ can be expressed by

$$f(t) = A_M(t) + \sum_{m \le M} D_m(t) \tag{4.23}$$

From Equation (4.23), it is obvious that the approximations are related to one another by

$$A_{M-1}(t) = A_M(t) + D_M(t) \tag{4.24}$$

Equations (4.23) and (4.24) provide a tree structure of a signal and also a reconstruction procedure of the original signal. By selecting different dyadic scales, an input signal can be decomposed into many low-resolution components, referred to as the wavelet decomposition tree (see Fig. 4.1).

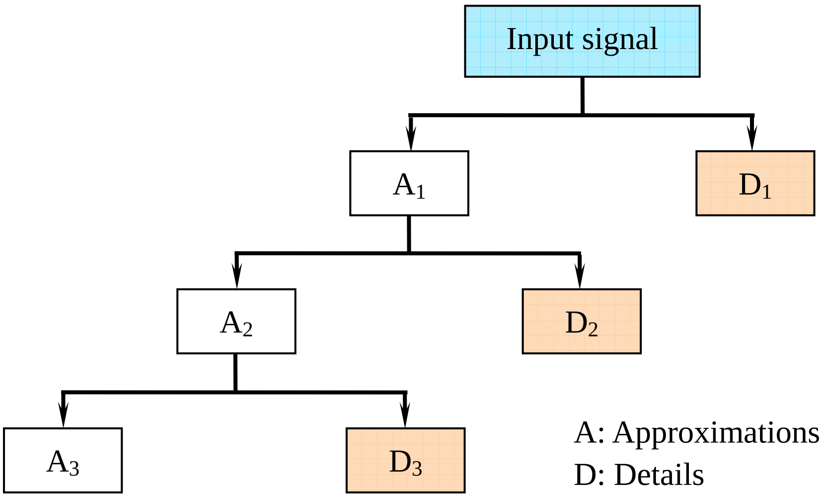

Fig. 4.1 Wavelet decomposition tree: A_1, A_2, A_3 are the low-frequency approximations; and D_1, D_2, D_3 are the high-frequency details.

The decomposed approximations and details capture the different frequency bands at different levels, giving information that may not be clearly seen in the original data. For instance, if the input signal is being sampled at f_s Hz, then the highest frequency of the sampled signal is represented by $f_s/2$ Hz based on the Nyquist theorem. The first detail, D_1, as the output of the highpass filtered input signal falls into the frequency band between $f_s/2$ and $f_s/4$. Likewise, the second detail, D_2, captures the band of frequencies between $f_s/4$ and $f_s/8$, and so on. Figure 4.2 illustrates the wavelet-decomposed frequency bands relative to the components shown in Fig. 4.1.

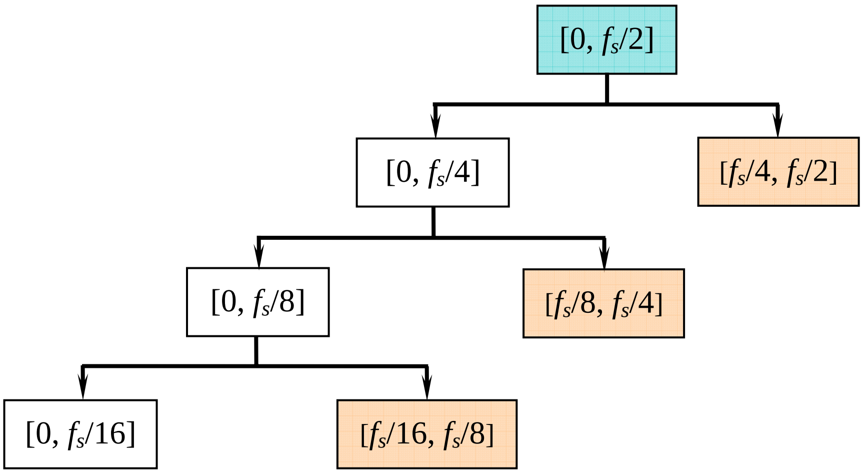

Fig. 4.2 Wavelet-decomposed frequency bands correspond to components of Fig. 4.1.

In this chapter, the discrete dyadic wavelet transform based on the Mallat algorithm (Mallat, 1988) is applied to reduce the computational effort involved. In addition, the discrete Meyer wavelet is selected as the wavelet basis for the same reason as discussed in Chapter 3.

4.3.3 Wavelet Transform Based on Cross-Validation

In this subsection, we propose to use the method of cross-validation (Stone, 1974; Clark and Thompson, 1978; Breiman et al., 1984; Nason, 1996; Schumacher et al., 1997) after the dyadic wavelet decomposition to automatically identify the wavelet-decomposed signal levels. The following implementation procedure is proposed (Zhong et al., 2007):

Step 1: The observational data series (x_i, y_i), i = 1, 2, … N is divided into two parts, the odd series ($x_{1, 2m-1}$, $y_{1, 2m-1}$) and the even series ($x_{2, 2m}$, $y_{2, 2m}$) m = 1, 2, … N_1 (when N is an even number, $N_1 = N/2$; while $N_1 = (N-1)/2$ when N is an odd number). The odd series is regarded as the filtering series, whilst the even series is randomly sampled into the validation series (sample size = N_2, and $N_2 << N_1$).

Step 2: K-level wavelet decomposition is applied to the filtering series and the filtered values f' at the kth level can be obtained. The variance of the validation series relative to the filter values can then be calculated with

$$C(k,P) = \frac{1}{N_2}\sum_{i=1}^{N_2}\left[y_{2,i} - f'(x_{2,i})\right]^2 \tag{4.25}$$

where P is a random division of the even series; ($x_{2,i}$, $y_{2,i}$), i = 1, 2, … N_2 is the validation samples; and $f'(x_{2,i})$ are values derived by cubic spline interpolation of the filter values for the $x_{2,i}$ epoch.

Step 3: The decomposed signals between the k_1th (k_1 = 1, 2, … K+1) and the k_2th ($k_2 = k_1$, k_1+1, … K+1) levels are used as the filtered values and repeat Step 2, where the details are from 1 to K levels and the approximation is represented by the (K+1)th level. Then, for each of the filter values from the k_1th to the k_2th levels, the even series is randomly sampled M times, denoted by P_j, j = 1, 2, … M. Thus, M variances C ($k_{1,2}$, P_j) can be obtained with Equation (4.25) and their mean can be finally derived

$$\overline{C}(k_{1,2}, P) = \frac{1}{M}\sum_{j=1}^{M} C(k_{1,2}, P_j)\,. \tag{4.26}$$

The $k_{1,2}$ (i.e., decomposed levels ranging from k_1 to k_2) that makes the smallest $\overline{C}(k_{1,2}, P)$ is considered the signal levels of the filtering series.

Step 4: The raw observational data series is decomposed with a (K+1)-level wavelet transform, and then select results from k_1+1 to k_2+1 levels as the signals based on the results of Step 3. A (K+1)-level wavelet transform is used because the sampling rate of the odd series is half that of the raw observational series.

Step 5: Keep the coefficients of the signal levels determined in Step 4 unchanged and set the coefficients of the other decomposition levels at zero. The filtered values of the observational series are reconstructed based on the wavelet coefficients thus obtained.

About 70% of the data in the middle of the observational series are selected for cross-validation to prevent edge effects due to poorer filtering results at the ends of a data series. Considering the computation efficiency and statistical significance of random divisions, we make the validation sample size N_2 be 20% of the filtering sample size N_1 and the number of divisions M = 20.

For convenience of reference, the wavelet filter that uses the method of cross-validation to determine the wavelet-decomposed signal levels is termed the cross-validation wavelet filter (CVWF).

4.4 Simulation Studies and Analyses

The simulated test data are generated using the following model:

$$u_t = y_t + e_t, \tag{4.27}$$

where e_t is a Gaussian white noise series with a normal distribution, and y_t is the signal component in the 'observable' sequence u_t.

4.4.1 CVVF Method

The simulated signals consist of three sinusoidal waves, with periods of 300 s, 150 s and 40 s, representing typical GPS multipath wavelengths, and a modulation signal with a period of 1200 s added to the sinusoidal wave of 300 s period. The model for simulating the signals is then

$$\begin{aligned} y_t &= 2.0\sin(2\pi t/1200)\times\sin(2\pi t/300) \\ &\quad + 0.5\sin(2\pi t/150) + 0.5\sin(2\pi t/40). \end{aligned} \tag{4.28}$$

The data sampling interval is 2 s and the sample size is 2000. The simulated results using Equation (4.28) at different noise levels, N (0, 2.0) and N (0, 3.5), are shown in Fig. 4.3. The optimal smoothing factors determined using the CVVF method are 0.01

and 0.0001 respectively. The RMS values of the difference between the simulated signals y_t and the filtered values $\bar{u}_t$ are ±0.220 cm and ±0.448 cm respectively for the two noise levels. The RMS values of the difference between the signals plus the noise u_t and the filtered values $\bar{u}_t$ are ±1.986 cm and ±3.579 cm respectively. The computation time for the example is about 30 s on a typical personal computer.

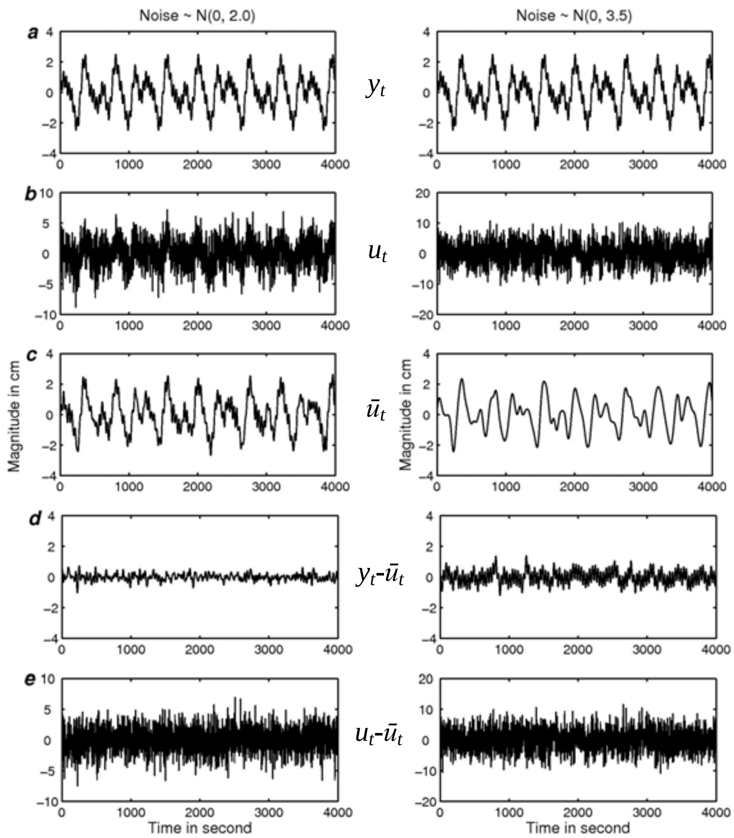

Fig. 4.3 Simulation results of CVVF method: ***a*** Simulated signal series; ***b*** simulated signal series plus noise *N* (0, 2.0) (*left panel*) and *N* (0, 3.5) (*right panel*); ***c*** filtered series with smoothing factor 0.01 (*left panel*) and 0.0001 (*right panel*); ***d*** difference between simulated signals and filtered values; and ***e*** difference between simulated signals plus noise and filtered values.

It can be seen from Fig. 4.3 that the smaller the smoothing factor, the smoother the filtered curve. When the standard deviation of the white noise reaches 2.0 cm, approaching the amplitude of the simulated signals of about 2.5 cm (see subplot *a* in Fig. 4.3), the signals and the noise can still be successfully separated. However, when the noise level reaches 3.5 cm, the high frequency signals of 40 s period are filtered out.

Some additional simulation studies have also been carried out to obtain further insights into the performance of the CVVF method at different noise levels. Table 4.1 summarizes the results, where the smoothing factors and the RMS values of the difference series at different noise levels are given.

Table 4.1 Optimal smoothing factors and RMS values of the differences between the simulated signal (y_t) and the filtered ($\bar{u}_t$) data series and between the simulated signal plus noise (u_t) and the filtered ($\bar{u}_t$) data series at different noise levels (unit: cm).

Noise level	0.2	0.6	1.0	1.4	2.0	2.4	3.0	3.5
Optimal smoothing factor	0.1	0.1	0.1	0.1	0.01	0.01	0.001	0.0001
RMS of y_t-$\bar{u}_t$ series	0.034	0.082	0.134	0.154	0.220	0.245	0.306	0.448
RMS of u_t-$\bar{u}_t$ series	0.203	0.583	0.987	1.373	1.986	2.321	3.003	3.579

Table 4.1 shows that the optimal smoothing factors decrease and the RMS values increase with the increase of the observational noise. The RMS of the difference series between $\bar{u}_t$ and u_t are always close to the corresponding noise levels (less

than 1 mm), indicating that the CVVF method works well for data series with different noise levels.

Figure 4.4 illustrates the relationship between the noise levels and the RMS values of the difference series between $\bar{u}_t$ and y_t. The magnitude of the simulated signals is about 2.5 cm. It is seen in Fig. 4.4 that when the noise level is lower than about 2.5 cm, the relationship is nearly a straight line, indicating that the signals and the noise can be separated almost completely by the CVVF method. When the noise level is greater than about 2.5 cm, the relationship tends to be less stable, since the high-frequency signals (periods shorter than 40 seconds) are filtered out together with the noise.

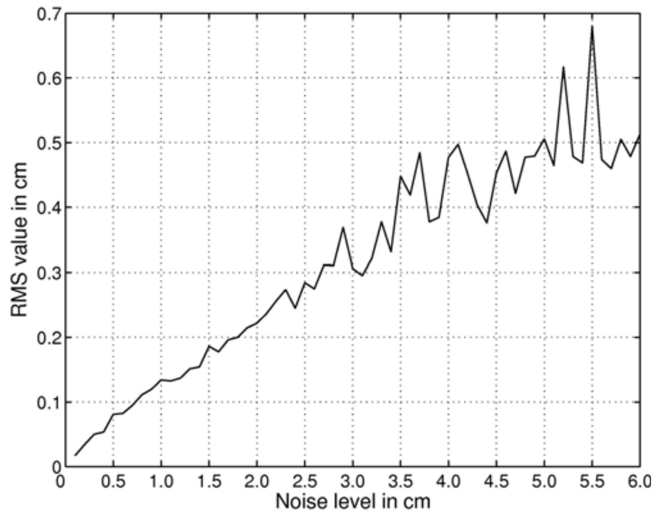

Fig. 4.4 Relationship between the noise levels and the RMS values of the difference series between filtered values and simulated signals.

A further simulation study was carried out to examine the performance of the proposed CVVF method. Here the signal is composed of two sinusoidal waves with periods of 1200 and (1200-k) seconds respectively, with k = 50, 100, …, 1150 (increment = 50). The simulation model is

$$u_t = 2.0\sin(2\pi t/1200) + 0.5\sin[2\pi t/(1200-k)] + e_t \tag{4.29}$$

where the random noise e_t follows the normal distribution N (0, 1.0). The data sampling interval and sample size are the same as those used for Equation (4.28), i.e., 2s and 2000 respectively. The period of one of the sinusoidal waves changes with k. The RMS values calculated from the differences between $\bar{u}_t$ and u_t are shown in Fig. 4.4.

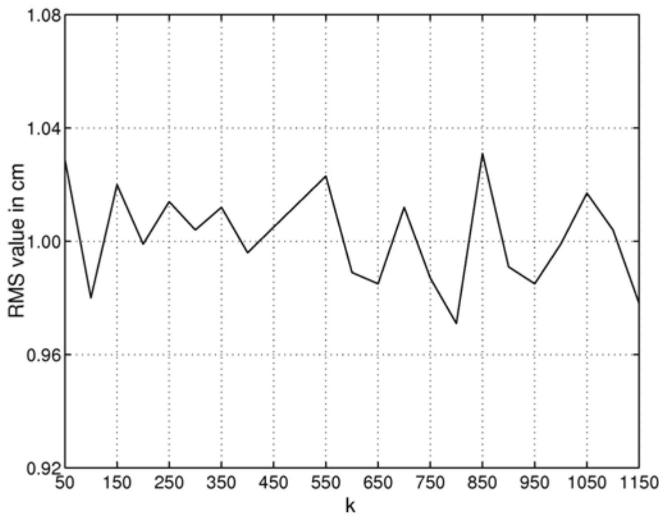

Fig. 4.5 RMS values calculated from the differences between filtered values and simulated signals plus noise. k is a factor used to adjust the periods of the second sinusoidal wave (see Equation (4.29)).

It is seen from Fig. 4.5 that the fluctuations of the RMS values of the differences between $\bar{u}_t$ and u_t are around 1.0 cm. This means that the time-varying signals have been effectively separated from the noise.

4.4.2 CVWF Method

Test observational series is simulated using the following model

$$u_t = \sin(2\pi t / 2400) + \sin(2\pi t / 300) + 0.6\sin(2\pi t / 60) + e_t \qquad (4.30)$$

where u_t is a simulated observation and e_t is Gaussian white noise. Compared with the simulation model of the CVVF method (i.e., Equation (4.28)), the modulation signal is not added to the model of the CVWF in order to theoretically determine which levels the wavelet-decomposed signal falls into. The observational series (signals) consists of three sinusoidal waves, with periods of 2400 s, 300 s and 60 s, representing GPS multipath wavelengths, since the typical multipath periods are considered to vary from tens of seconds to tens of minutes as discussed in Chapter 2. The data sampling rate is 1 s and the sample size is 4000.

Figure 4.6 shows the 8-level Meyer wavelet decomposition of the simulated data series at noise level $N(0, 1.0)$, where S is the simulated observational data series; $a8$ and $d8$-$d1$ denote the approximation and details respectively. As the wavelet transform is linear, the signal obtained after wavelet decomposition can be represented by $S = a8 + d8 + d7 + \ldots + d1$.

It is seen from Fig. 4.6 that the extrema and amplitudes of the noise decrease with the increase of the decomposition level. It is therefore considered that the signals exist at the higher levels. The signal levels determined by the CVWF method are the details of $d5$-$d8$ and the approximation of $a8$ (or $d5$-$a8$, the same below). To analyze the

Meyer wavelet-decomposed signal levels theoretically, the central frequencies relative to each of the decomposition levels are listed in Table 4.2.

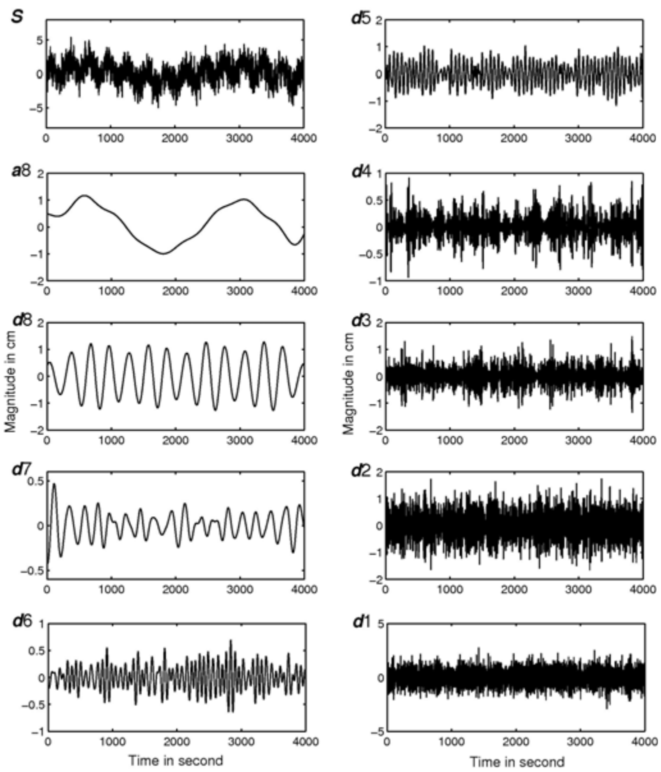

Fig. 4.6 Meyer wavelet decomposition of simulated data series at noise level *N*(0, 1.0): ***S*** simulated signal series; ***a*8** approximation; ***d*8-*d*1** details from levels 8 to 1.

Table 4.2 Central frequencies of Meyer wavelet for data series with sampling rate of 1 Hz.

Level	*d*1	*d*2	*d*3	*d*4	*d*5	*d*6	d7	*d*8
Freq. (Hz)	0.3317	0.1658	0.0829	0.0415	0.0207	0.0104	0.0052	0.0026

It can be seen from the frequencies of the simulated signal and Table 4.2 that the signal with a frequency of 0.0167 Hz (corresponding to 60-s period signal in

Equation (4.30)) falls between *d*5 and *d*6, whilst the signal of 0.0033 Hz (300 s in period) falls between *d*7 and *d*8. Since *a*8 represents the frequency range of 0 to 0.0020 Hz based on the knowledge of the dyadic wavelet decomposition (see Section 4.3.2 for details), the frequency of 0.0004 Hz (2400 s in period) exists at the level of *a*8. Therefore, the signal levels identified above are the same as the result of cross-validation.

To obtain further insights into the performance of the proposed technique at different noise levels, Table 4.3 summarizes some additional test results, including the signal levels and the RMS values of the series that result from noting the difference between the simulated signal and the filtered series at different noise levels. The results for noise levels of $N(0, 1.4)$ and $N(0, 1.8)$ are shown in Fig. 4.7.

Table 4.3 Signal levels determined with the cross-validation method and RMS values of the difference series between the simulated and the filtered data series at different noise levels.

Noise level (cm)	0.4	1.0	1.4	1.8	2.4	3.0
Signal levels	*d*5-*a*8	*d*5-*a*8	*d*5-*a*8	*d*7-*a*8	*d*8-*a*8	*d*8-*a*8
RMS (cm)	0.100	0.262	0.364	0.476	0.520	0.535

The results in Table 4.3 indicate that the signal levels decrease with the increase of noise levels, meaning that fewer signals remain in the filtered values. Also the RMS values of the difference series between the simulated signal and the filtered data series are quite small, indicating that the combination of wavelet transform and cross-validation works well for data series with different noise levels.

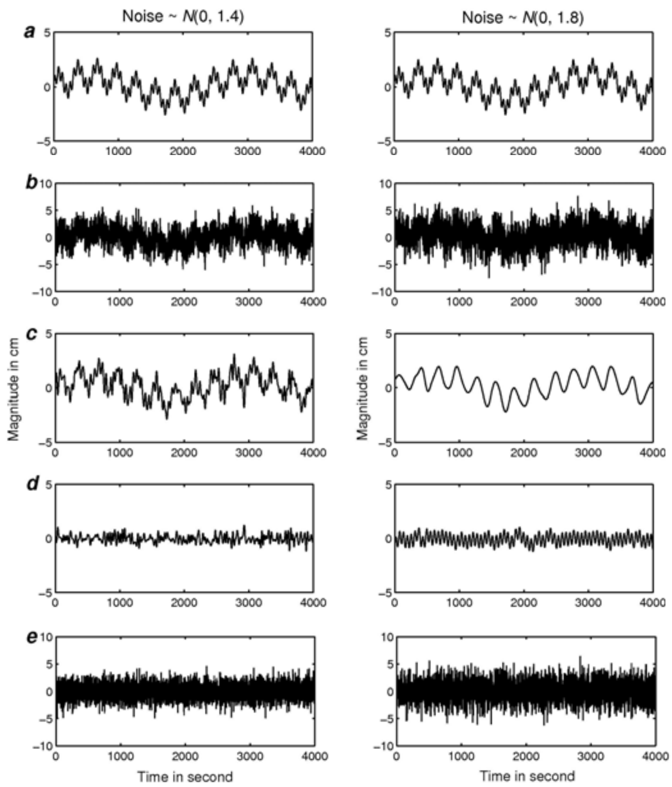

Fig. 4.7 ***a*** simulated signal series; ***b*** simulated signal series plus noise *N*(0, 1.4) (*left panel*) and *N*(0, 1.8) (*right panel*); ***c*** filtered series with signal levels *d*5-*a*8 (*left panel*) and *d*7-*a*8 (*right panel*) kept; ***d*** difference between simulated signals and filtered values; and ***e*** difference between simulated signals plus noise and filtered values.

It can be seen from Fig. 4.7 that when the standard deviation of the white noise reaches 1.4 cm, approaching half of the amplitude of the simulated signal (about 2.6 cm) (see subplot *a* in Fig. 4.7), the signals and the noise can still be successfully separated. However, when the noise level reaches 1.8 cm, high-frequency signals of 60 s in period are filtered out.

4.5 Mitigation of Multipath in Real GPS Data

Here we use the CVVF and CVWF methods to extract a model of multipath effects from GPS measurements and then use the model to correct subsequent GPS measurements. In the experiment, GPS observations were collected on the roof of a building at the Hong Kong Polytechnic University, using two dual-frequency GPS receivers (Leica System SR530 with AT-502 antennas) with a baseline length of about 86 m, from 10 March 2004 (DOY 070) to 12 March 2004 (DOY 072) at a sampling rate of 10 Hz. Many strong GPS signal reflectors exist in the vicinity of the receivers as shown in Fig. 4.8.

Fig. 4.8 Test site and motion simulation table for the experiments.

The coordinates of the rover antenna were estimated in a post-processing kinematic mode, where the ambiguities were fixed in the processing. The resolved point coordinates for a period of nearly 45 minutes over three consecutive days are used for the analysis and shown in Figs. 4.9, 4.10 and 4.11 for the *X*, *Y* and *H* directions respectively. The *X* and *Y* coordinates correspond to the Easting and Northing directions in a Universal Transverse Mercator (UTM) system, while the *H* coordinate gives the ellipsoidal height. For easy interpretation, the mean coordinates have been removed from the coordinate time series.

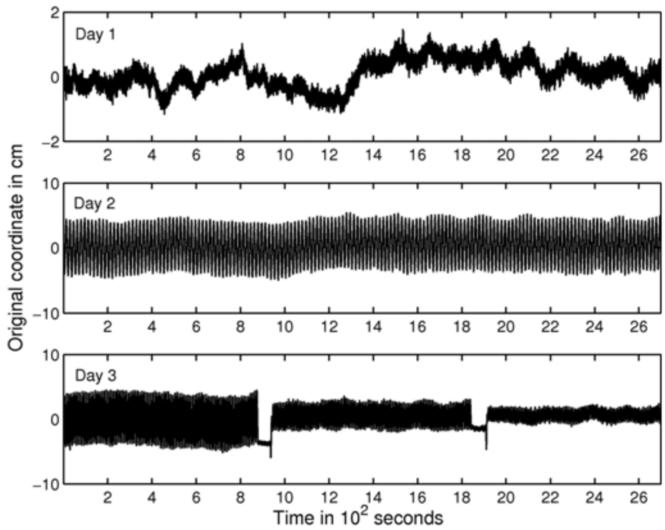

Fig. 4.9 Original *X* coordinates over the three consecutive days, with different motion patterns (Day 1: static; Day 2: motion with frequency of 0.06Hz and amplitude of 40mm; Day 3: motion with frequency of 0.1Hz and amplitude varying from 40mm to 20mm, then from 20mm to 10mm).

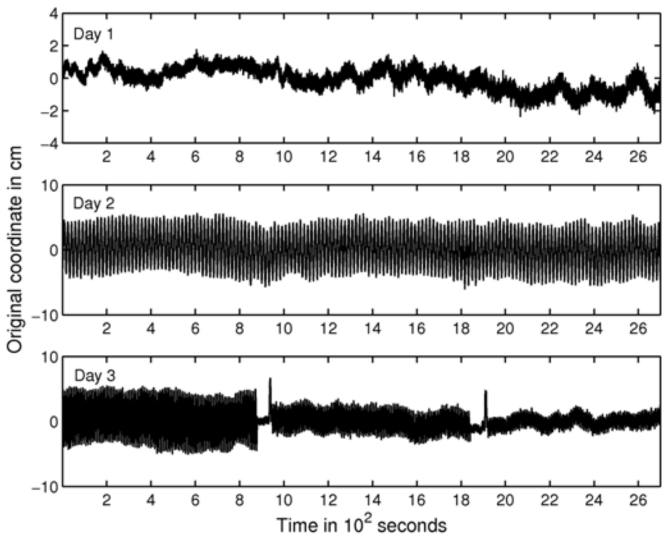

Fig. 4.10 Original *Y* coordinates over the three consecutive days, with different motion patterns (the same as those described in Fig. 4.9).

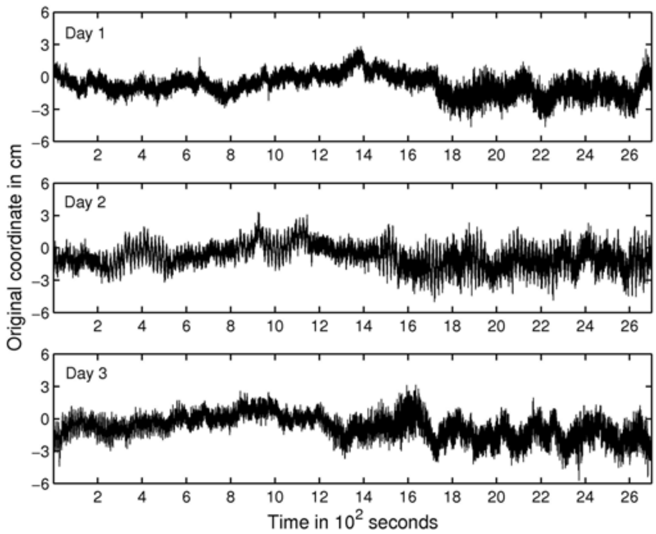

Fig. 4.11 Original *H* coordinates over the three consecutive days, with different motion patterns (the same as those described in Fig. 4.9).

In the tests, the GPS antenna was kept still during the first day's test, but was set on a motion simulation table on the second and third days. The motor-driven motion simulation table can simulate various modes of motions (see Section 3.3 for details). The frequency and amplitude of the simulated motion for the second day were 0.06 Hz and 40 mm respectively, while for the third day the frequency was 0.1 Hz and the amplitude was changed from 40 to 20 mm, then gradually from 20 to 10 mm. All the simulated motions were in the horizontal plane only. Due to the design of the motion simulation table, it had to be reset to its original position before a new motion mode could be introduced. Therefore, abnormal values (see e.g. the third subplots in Figs. 4.9 and 4.10) appear in the time series at locations when a new motion mode was introduced. We will view these abnormal values as gross errors and ignore them in data processing.

4.5.1 CVVF Method

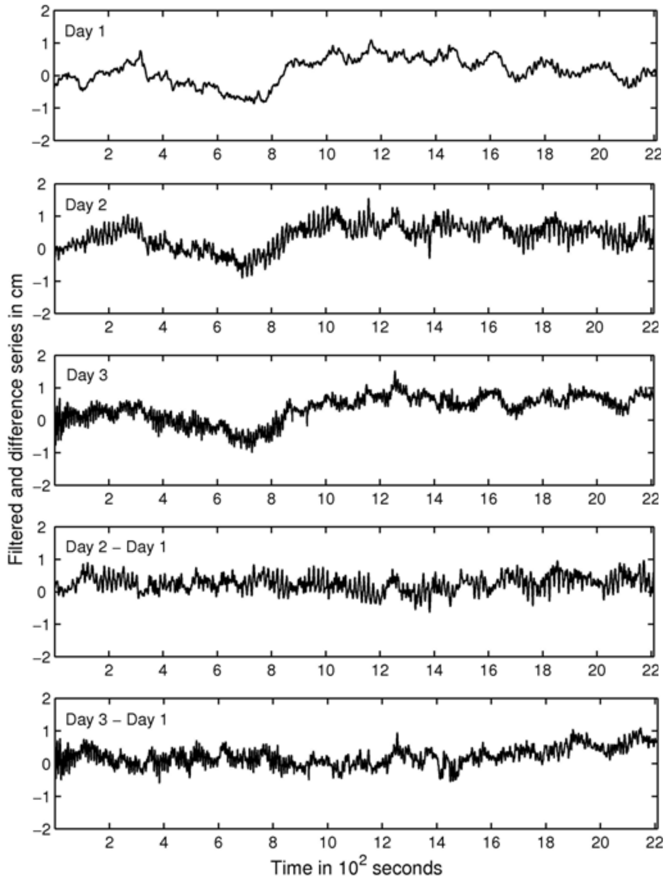

Fig. 4.12 Filtered and difference series of the *X* direction, with the simulated motions removed.

Figures 4.12, 4.13 and 4.14 show the CVVF-filtered *X, Y* and *H* coordinates of the 3 days and the differences between the results from the different days. The simulated motions were removed from the coordinate series before applying the CVVF method to more clearly show the errors caused by the multipath disturbance. It is considered that the signals in the plots are mainly caused by multipath disturbance as the noise has been filtered out already. It is however interesting to note that there were still some high-frequency signals in the results from the second and third days (Figs. 4.12, 4.13 and 4.14). It is considered that the signals were caused by residual vibrations of the table and an additional multipath signature due to the movement of the antenna, because the signals have the same frequency as the simulated motions. The smoothing factors ε and the RMS values of the noise series derived using the CVVF method are listed in Table 4.4. The maximum correlation coefficients between the multipath time series of the consecutive days in the *X*, *Y* and *H* directions are given in Table 4.5.

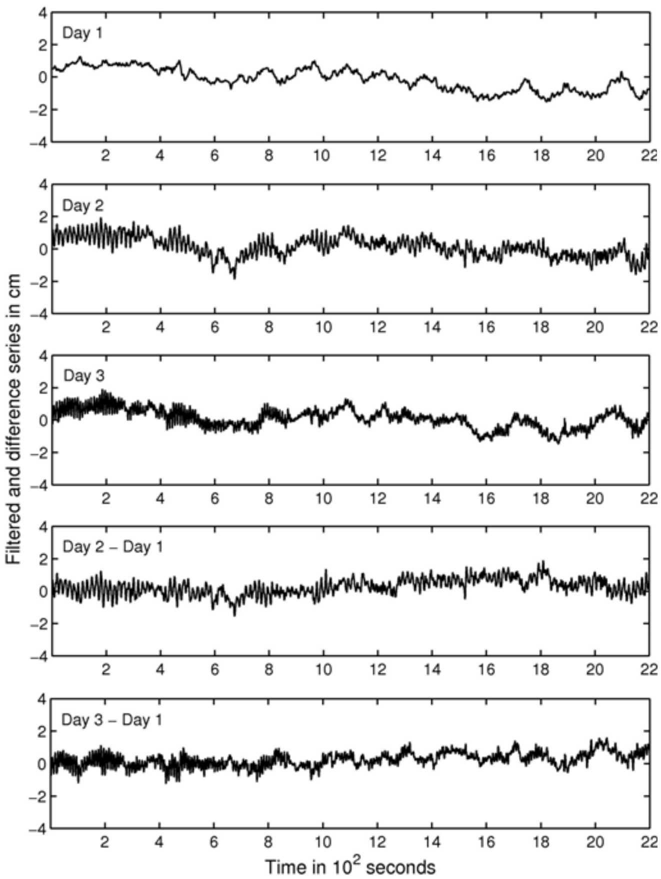

Fig. 4.13 Filtered and difference series of the *Y* direction, with the simulated motions

removed.

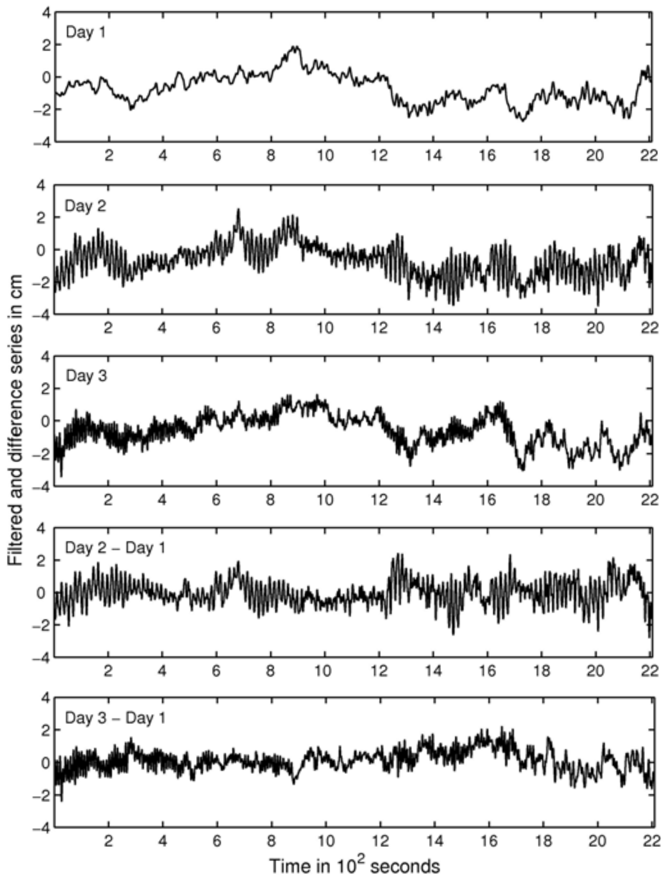

Fig. 4.14 Filtered and difference series of the *H* direction, with the simulated motions removed.

Table 4.4 Optimal smoothing factors and RMS of noise series for GPS test results.

Day	*X*		*Y*		*H*	
	ε	RMS (cm)	ε	RMS (cm)	ε	RMS (cm)
1	1.0e-6	0.121	1.0e-6	0.210	1.0e-7	0.456
2	1.0e-5	0.120	1.0e-5	0.238	1.0e-5	0.475
3	1.0e-4	0.120	1.0e-4	0.225	1.0e-5	0.496

Table 4.5 Maximum correlation coefficients between multipath series of the three days *X*, *Y* and *H* coordinates.

Day	*X*	*Y*	*H*
1-2	0.809	0.684	0.665
2-3	0.686	0.612	0.543

It is seen from Table 4.4 that the optimal smoothing factors are different for the different days and the different directions, but the RMS values of the noise series are almost the same for the same directions. This indicates that the CVVF method has successfully separated the noise in all cases.

It is seen from Table 4.4 that the smoothing factors of the second and the third day determined with the method of cross-validation are larger than those of the first day. This is due to the high-frequency signals in the data series from the second and third days. As discussed in Section 4.4, the larger the smoothing factor, the rougher the filtered curve and thus, the more high-frequency signals remain in the filtered curve.

It is also seen from Table 4.4 that the RMS values of the *H* direction are larger than those of the *X* and *Y* directions, indicating that the random errors in the vertical direction are larger than those in the horizontal directions. This agrees well with the fact that the positioning accuracy of GPS in the vertical direction is generally worse than that in the horizontal direction.

The results in Table 4.5 show that the correlation coefficients fall between 0.809 and 0.543, all of which exceed the threshold value of ±0.22 at the 99% confidence level by using the Monte Carlo test (Zhou and Zheng, 1999), despite the existence of the high-frequency multipath disturbances in the data series. Accurate multipath models established using the first day's coordinate series are removed from the coordinate series of subsequent days based on the sidereal day-to-day repeating property of GPS multipath signals. The results are shown in the fourth and fifth panels of Figs. 4.12, 4.13 and 4.14 for the three directions. The RMS values of the second and third days' coordinate time series with and without applying the multipath corrections are given in Table 4.6 to show the effects of the corrections. The results in Table 4.6 show that the RMS values of the second and the third days' errors have been reduced by about 20–40% after the multipath corrections are applied.

Table 4.6 RMS errors of the second and third day coordinate series in the *X*, *Y* and *H* directions before and after multipath corrections are applied (unit: cm).

Day	*X*		*Y*		*H*	
	Before	After	Before	After	Before	After
2	0.400	0.251	0.622	0.501	0.987	0.775
3	0.422	0.288	0.591	0.432	0.932	0.648

4.5.2 CVWF Method

The CVWF-filtered *X*, *Y* and *H* coordinates of the 3 days and the differences between the results of the different days are quite similar to those shown in Figs. 4.12, 4.13 and 4.14, thus they are not illustrated here. The wavelet-decomposed signal levels determined using the cross-validation method and the RMS values of the noise series are listed in Table 4.7.

Table 4.7 Wavelet-decomposed signal levels and RMS of noise series for GPS test results.

Day	*X*		*Y*		*H*	
	Signal level	RMS (cm)	Signal level	RMS (cm)	Signal level	RMS (cm)
1	*d*6-*a*8	0.122	*d*7-*a*8	0.216	*d*7-*a*8	0.462
2	*d*5-*a*8	0.120	*d*5-*a*8	0.236	*d*6-*a*8	0.493
3	*d*5-*a*8	0.122	*d*5-*a*8	0.228	*d*6-*a*8	0.509

It is seen from Table 4.7 that the wavelet-decomposed signal levels from the second and third days determined using the cross-validation method are greater than those of the first day. Therefore more signals are retained in the data series from the last two days. This coheres with the existence of high-frequency signals in the second and third day's coordinates.

It is also seen from Table 4.7 that the signal levels are different for the different days and the different directions, but the RMS values of the noise series are almost the same for the same directions. This explains that the signals have been successfully separated from the noise by using the CVWF method in all cases.

The maximum correlation coefficients between the filtered series of the two consecutive days fall between 0.807 and 0.548, all of which exceed the threshold value of ±0.22 at the 99% confidence level by using the Monte Carlo test (Zhou and Zheng, 1999). Accurate multipath models derived from the first day's CVWF-filtered coordinate series are removed from the coordinate series of subsequent days by taking advantage of the sidereal day-to-day repeatability. The results show that the RMS values of the second and third days' errors were reduced by about 20–40% after the corrections.

4.6 Conclusions and Discussions

Two data filtering methods, CVVF and CVWF, have been proposed based on the method of cross-validation. The CVVF method uses the cross-validation method to determine the optimal smoothing factor of the Vondrak numerical filter; whereas the CVWF method utilizes the method of cross-validation to identify the wavelet-decomposed signal levels. The two methods have been applied to mitigate multipath effects in GPS observations. The following conclusions can be drawn from the study:

(1) Both CVVF and CVWF methods are effective signal decomposers, however the former is superior to the latter. The CVVF method can be used to separate noise and signal in a data series when the noise level is lower than

the magnitude of the signal. When the noise level is higher than the magnitude, high-frequency signals tend to be filtered out together with the noise. With regard to the CVWF method, the signal can be separated from noise when the noise level is lower than half of the magnitude of the signal. When the noise level is higher than half of the magnitude, high-frequency signals may be filtered out.

(2) Both methods work well for data series with different noise levels. The CVVF method also does well for data series with different frequencies of signal at different sections of the series.

(3) For the CVVF method, the larger the smoothing factor, the rougher the filtered curve and the more high-frequency signals remain in the data series.

(4) Reliable GPS multipath models for point coordinate series can be derived with the CVVF and CVWF methods. The models can be used to reduce the effects of GPS multipath by taking advantage of the sidereal day-to-day repeating characteristics of GPS multipath signals. Test results have shown that 20–40% improvement in GPS accuracy can be achieved using the two methods.

[blank page]

Chapter 5

Integrated Use of CVVF, SIGMA-Δ and ARTA Methods for Mitigating Multipath Effects

5.1 Introduction

The accuracy of GPS in small scale engineering applications is limited mainly by multipath disturbance and signal diffraction. To improve the satellite distribution geometry and shorten the required observation time, observations from low elevation satellites may be included in data processing but this increases the systematic errors and noise. One way of reducing the errors is to utilize stochastic or weighing models. Comp and Axelrad (1997) use the signal-to-noise ratio (SNR) values to model the multipath effects. The SIGMA-ε model developed by Hartinger and Brunner (1998) uses the carrier-to-noise power-density ratio (C/N_0) values to weight GPS observations. Since the diffracted GPS signals are usually associated with low C/N_0 values, Brunner et al. (1999) have developed a SIGMA-Δ model for stochastic modelling of the diffraction errors.

In precise real-time positioning, estimation of point position with single-epoch observations is possibly highly affected by multipath errors. One technique of mitigating the multipath errors is to use sidereal filtering (Bock, 1991) by taking advantage of the fact that the GPS satellites orbit the Earth with a period of half a sidereal day, bringing the same satellite configuration at the same time on successive sidereal days. The sidereal day-to-day correlation of GPS coordinate series has been discussed for multipath research over the last decade (Elósegui et al., 1995; Radovanovic, 2000; Wübbena et al., 2001; Park et al., 2004). However, some researchers found that the satellite repeat period is not sidereal (Seeber et al., 1997; Ding et al., 1999). Recent investigations of Choi et al. (2004) showed that correcting coordinates using data from the previous day, shifted by the mean of the individual orbit repeat periods, gave more precise results than using the nominal sidereal period (86,164 s). This method was termed modified sidereal filtering (MSF). More recently, Larson et al. (2007) developed an aspect repeat time adjustment (ARTA) method to estimate time-varying and site-dependent shifts.

This chapter investigates the variations in the multipath day-to-day repeatability and the advantages of the current methods in maximizing GPS accuracy improvements over a time period of tens days. In general, for precise positioning applications such as deformation monitoring, low cutoff elevation angle of GPS satellites (e.g. 10–15°) can be used to minimize the multipath disturbance and signal blockage (Meng et al., 2004). However, the errors caused by diffracted GPS signals may become significant. In this chapter, the stochastic SIGMA-Δ model is used to mitigate the diffraction errors, which is followed by application of the CVVF to establish a multipath signal model (see Chapter 4 for details) and use of the ARTA method to reduce the multipath effects. We first present the method of obtaining the orbital repeat periods and show their variations. The SIGMA-Δ weight model and the ARTA method are then introduced. Finally, the method integrating SIGMA-Δ, CVVF and ARTA is applied to GPS observational data over a time period of about one month and compared with other traditional methods. The comparative results of accuracy improvements are also presented.

5.2 Orbital Repeat Periods

The average orbit repeat period (T_a) of an individual satellite can be determined by the GPS broadcast ephemeris parameters and Kepler's Third Law (Axelrad et al., 2005):

$$n = \sqrt{GM / a^3} + \Delta n \tag{5.1}$$

$$T_a = 86400 - 2(2\pi / n) \tag{5.2}$$

where n is the mean motion; GM = 3986005×10^8 m^3/s^2 is the Earth's universal gravitational parameter; a is the semi-major axis of the satellite orbit; and Δn is the mean motion difference.

Figure 5.1 shows the daily orbital repeat periods based on the global combined broadcast ephemerides for the GPS constellation for the year 2005. It is seen from Fig. 5.1 that the repeat periods are greater than the nominal sidereal period and different for each satellite, the variations of which show a secular drift, small amplitude oscillations, and sudden changes. The secular drift is due to resonance of the GPS orbits with the tesseral harmonics in the Earth's gravity field; the small amplitude oscillations occur twice monthly due to perturbations caused by lunar gravity; and the abrupt changes in the repeat periods are caused by manoeuvres of satellite orbit maintenance (Choi et al., 2004).

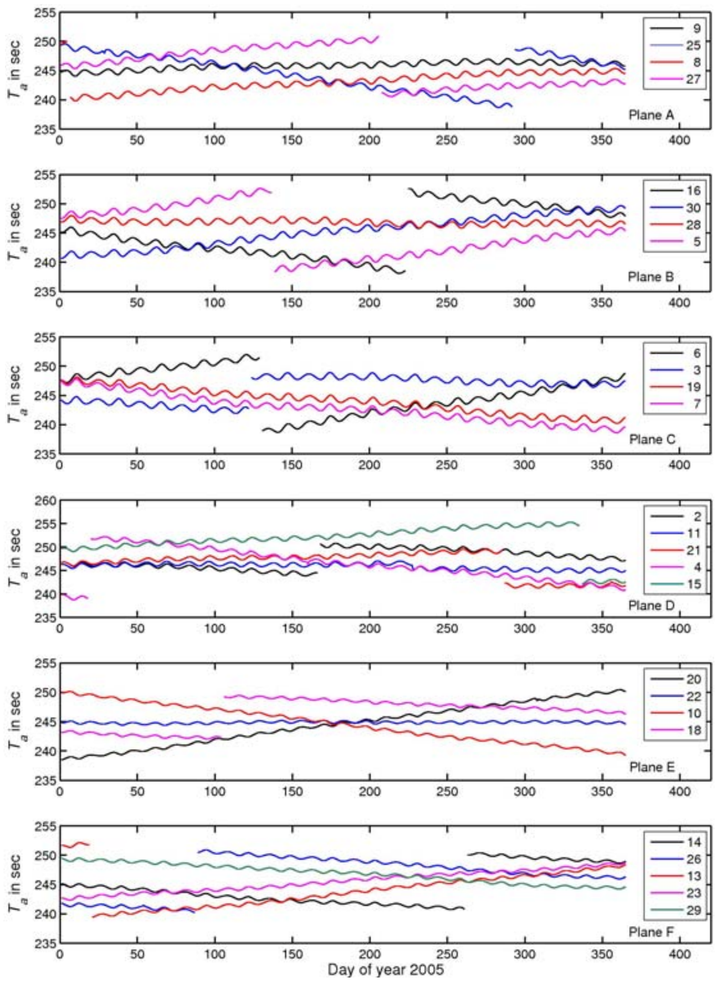

Fig. 5.1 Orbit repeat periods of GPS (PRN) satellites for the 6 orbital planes for 2005 (satellites with unusual periods are not shown herein (see Fig. 5.2)).

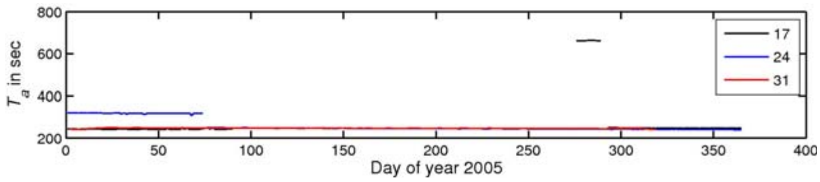

Fig. 5.2 Orbit repeat periods for PRNs 17, 24 and 31 for the year 2005.

Figure 5.2 illustrates three satellites, PRNs 17, 24 and 31, with large manoeuvres which can be identified in the GPS NANUs (Notice Advisory to Navstar Users) messages. For instance, the satellite PRN 24 was removed for maintenance on DOY 074 and repositioned on DOY 075. The satellites with orbits manoeuvred significantly are not precisely repeatable and thus excluded in our analysis.

The GPS satellite orbits are designed for repeating ground tracks; however, because of the orbital perturbations and manoeuvres that correct and reposition the orbits, the ground tracks are modified. In reality, the orbital period is set about 4 seconds faster than half-sidereal to compensate for a westward drift of the longitude of the ascending node of 14.665 degrees per year, caused mainly by the earth oblateness (Axelrad et al., 2005). Thus, the orbit repeat time for most satellites is expected to be about 8 seconds earlier than sidereal.

5.3 Stochastic SIGMA-Δ Model

The GPS signal power is a measure of its quality, which can be expressed by the carrier-to-noise power-density measurement C/N_0, i.e. the ratio of the signal carrier power to the noise power in a 1-Hz bandwidth (Langley, 1997). The C/N_0 is the real power ratio received at the GPS antenna and is recorded in the binary observational data file. Since the antenna design and receiver processing techniques have a significant impact on the C/N_0 value, it is therefore a key parameter in analysing the GPS receiver performance and it directly affects the precision of GPS phase observations (Langley, 1997).

The SIGMA-Δ weight model uses the measured C/N_0 values of the GPS signals and a template function to estimate weights for the least squares adjustment of the phase data. The variance of the phase observations σ_Δ^2 can be obtained by (Brunner et al., 1999)

$$\sigma_\Delta^2 = C_i \cdot 10^{-(C/N_{0\text{measured}} - \alpha \cdot \Delta)/10} \tag{5.3}$$

where the subscript i indicates the L_i signal (L_1 or L_2); C_i depends on the bandwidth of the tracking loop used by the receiver tracking channel (C_1 equals 2.30×10^4 mm^2 in the analysis below); the factor α is an empirical constant, which is generally chosen to be 2.0; and Δ is the difference between the C/N_0 observation and a template value, which is expressed as

$$\Delta = C/N_{0\text{template}} - C/N_{0\text{measured}} . \tag{5.4}$$

Since the C/N_0 is mainly elevation dependent, the C/N_0 template for a certain antenna type is defined by the highest C/N_0 values at a certain elevation angle. Figures 5.3 and 5.4 show the C/N_0 observations and templates of a Leica choke-ring antenna (AT504) and a light weight single-frequency antenna used in the experiment, each connected to a Septentriod PolaRx2@ GPS receiver.

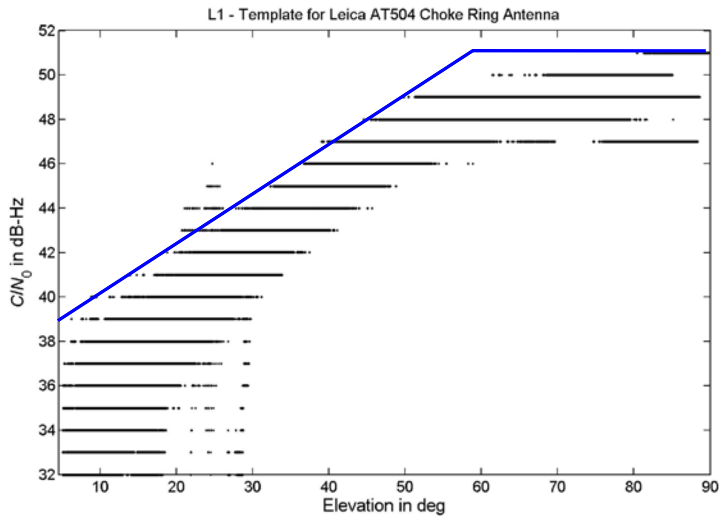

Fig. 5.3 C/N_0 and template for Leica AT504 choke ring antenna (L_1).

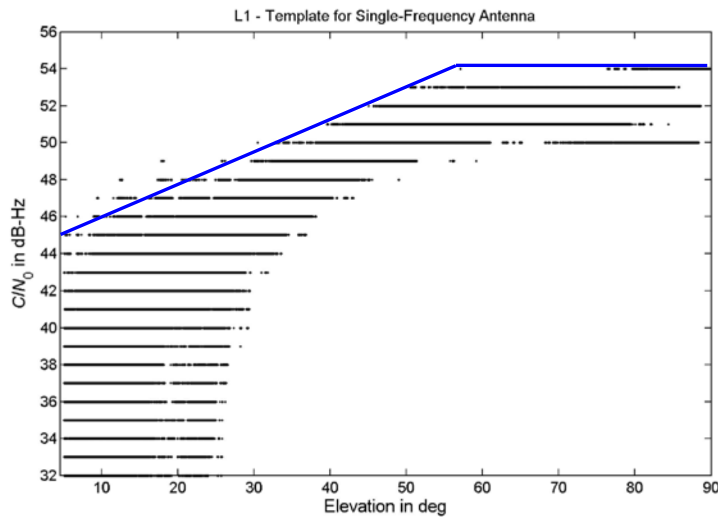

Fig. 5.4 C/N_0 and template for light weight single-frequency antenna (L_1).

The envelopes of the highest C/N_0 values in Figs. 5.3 and 5.4 represent the best signal quality to be obtained at certain GPS sites. The variance of a double-difference (DD) phase observations can be calculated using Equation (5.3) and the law of the propagation of variances. Since the diffracted GPS signals coincide with the difference as shown in Equation (5.4), the signal diffraction can be mitigated in the least squares adjustment by de-weighting the DD phase observations when Δ is not equal to zero.

5.4 Aspect Repeat Time Adjustment (ARTA)

The aspect repeat time adjustment (ARAT) method was developed by Larson et al. (2007) to account for the different contributions from different satellites to the coordinates and the disparate levels of multipath. The method of ARAT uses the coordinate time series of each GPS site to estimate the time-varying and site-dependent shift. The optimal shifts between two days of coordinate series are determined by minimizing the RMS difference for a range of shifts (e.g. 236–256 sec).

When implementing the ARTA, a shift interval needs to be estimated that depends on how quickly the dominant multipath period changes (Larson et al., 2007). To illustrate how to select the shift interval, the GPS observations of the North component on 19 November 2005 (DOY is 323) are taken as an example. Details of the GPS experiments can be found in Section 5.5.1. The RMS values in each consecutive time interval for a one-hour period using various shift intervals are calculated. The intervals of 60, 120, 240 and 480 seconds are used as examples as they well represent the variation of RMS with the shift intervals (see Fig. 5.5).

The results in Fig. 5.5 indicate that the shorter shift intervals (60 and 120 seconds) are clearly better than using the longer intervals (240 and 480 seconds). The interval of 60 s gives generally low RMS values; however, they also exhibit highly oscillatory behaviour when compared to the 120-sec interval. The estimated optimal shift values associated with intervals of 60 s and 120 s, as shown in Fig. 5.6, are further investigated.

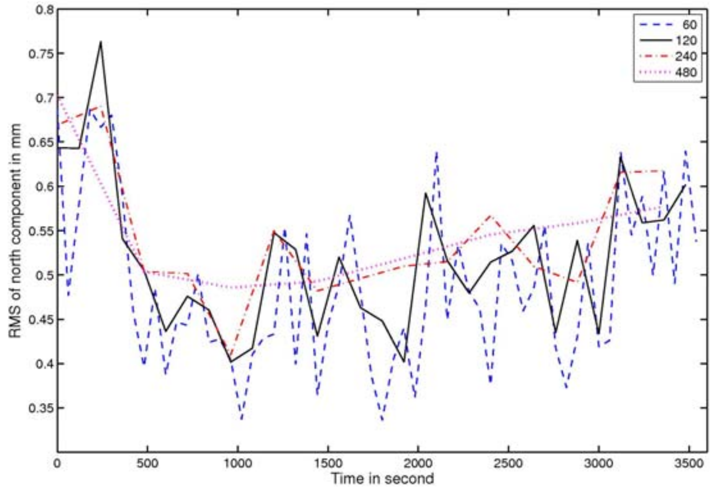

Fig. 5.5 RMS of the North component after ARTA using shift intervals of 60, 120, 240 and 480 seconds.

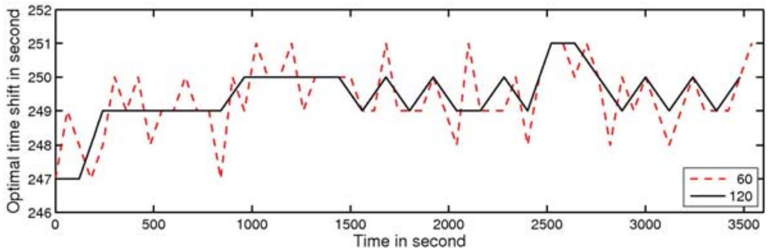

Fig. 5.6 Estimated optimal time shifts after ARTA using shift intervals of 60 and 120 seconds.

It is seen in Fig. 5.6 that the estimated time shifts for a 120-sec interval are more stable than those for the interval of 60 seconds. Therefore, a shift interval of 120 seconds is used in this chapter as it provides both good RMS improvement and a stable estimate of time shifts.

5.5 GPS Experiments and Results

5.5.1 GPS Data Acquisition

GPS observations were collected from two stations that were about 11 m apart, located on the roof of a building in Hong Kong. There are some strong GPS signal reflectors in the vicinity of the stations. A Septentriod PolaRx2@ GPS receiver was used to take observations from 18 November 2005 (DOY 322) to 16 December 2005 (DOY 350) at a data sampling rate of 1 Hz. A Leick AT504 choke ring antenna was fixed on a concrete pillar as the reference station, while a light weight single-frequency antenna was used for the rover station (see Fig. 5.7). The satellite elevation cutoff angle was set to 12°.

Fig. 5.7 Reference and rover stations and site environment.

The position of the rover antenna was calculated epoch-by-epoch in a kinematic mode and then projected into a map grid system ENU (East, North, up). The results for a period of 24 hours over the 29 consecutive days are shown in Figs. 5.8, 5.9 and

5.10 for the East, North and up components respectively. Offsets of 10 cm, 6 cm and 16 cm are added to the East, North and up components respectively, to separate the time series for clarity. The mean coordinates have been removed from the results for easy interpretation of the variations.

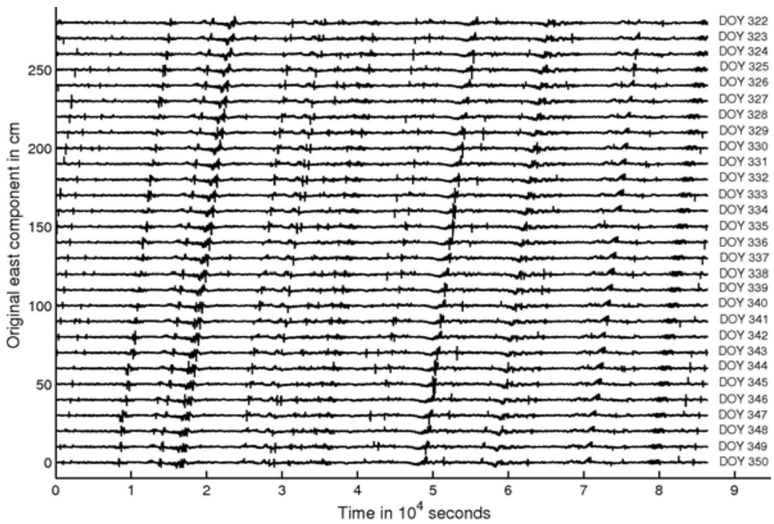

Fig. 5.8 Original East component from DOY 322 (top) to 350 (bottom).

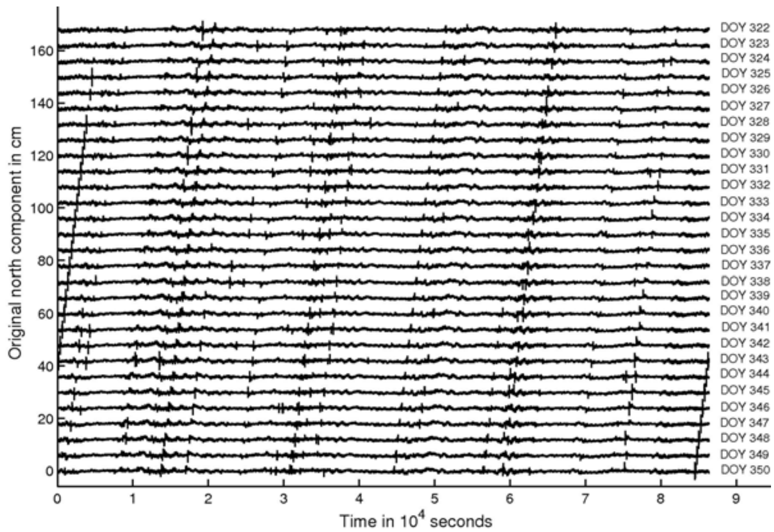

Fig. 5.9 Original North component from DOY 322 (top) to 350 (bottom).

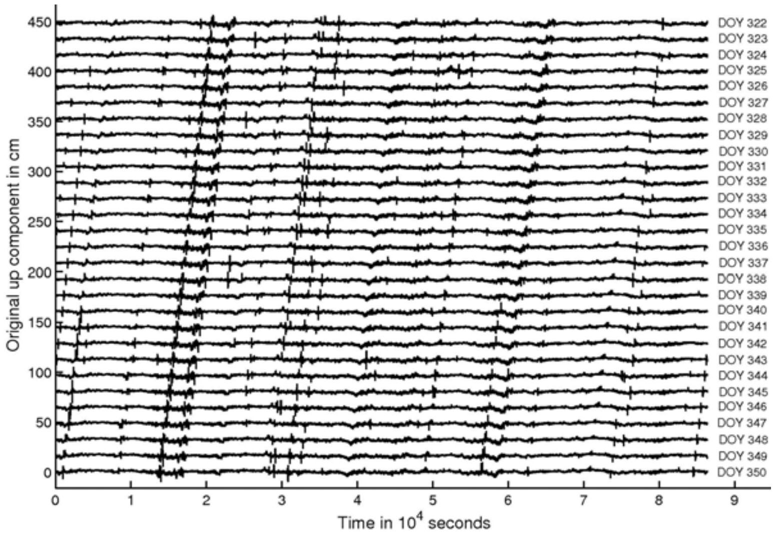

Fig. 5.10 Original up component from DOY 322 (top) to 350 (bottom).

It can be seen from Figs. 5.8, 5.9 and 5.10 that sudden changes of up to several centimeters appear in the coordinate series, but the day-to-day repeatability of some of the sudden changes is not obvious. It is considered that the abnormal values are caused by the effects of signal diffraction. These sudden changes will affect the analysis of the repeating property of multipath signals if they are not removed. The comparative results with and without the removal of the diffraction will be presented later.

5.5.2 Mitigation of Diffraction Effects

The stochastic SIGMA-Δ model is used to reduce the signal diffraction effects. The coordinate series of 18 November 2005 (DOY 322) will be used as an example. The coordinate series for all three components before and after applying the SIGMA-Δ model are shown in Figs. 5.11 and 5.12 respectively. To show the coordinate outliers which are defined as data points greater than 3 times the interquartile range (IQR) of the data series in any direction, the outlier bounds are indicated by the horizontal lines in Figs. 5.11 and 5.12. The IQR is more sensitive to the data outliers than the traditional mean and standard deviation, since changes in the upper and lower 25% of the data series do not affect it (Bock et al., 2000). To show the effects of the SIGMA-Δ model, Table 5.1 gives the median, outlier bounds and number of outliers in the coordinate series with and without applying the method.

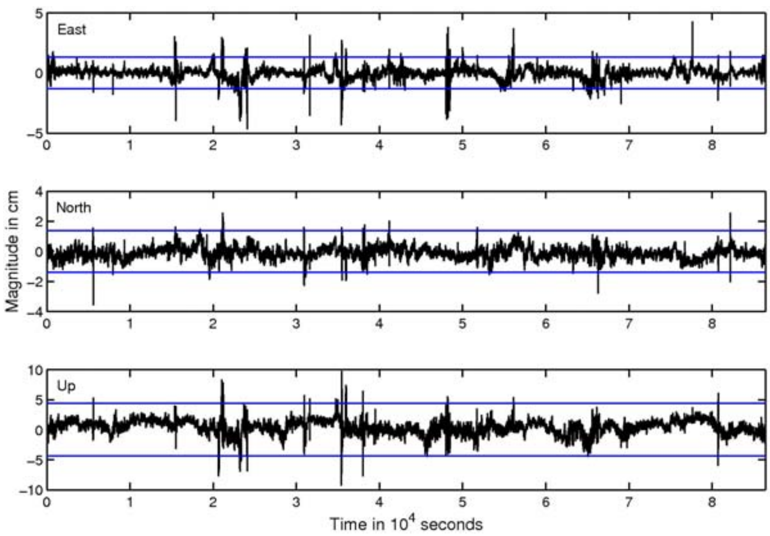

Fig. 5.11 Original coordinates for the East, North and up components and bounds for outlier rejection indicated by horizontal lines on DOY 322.

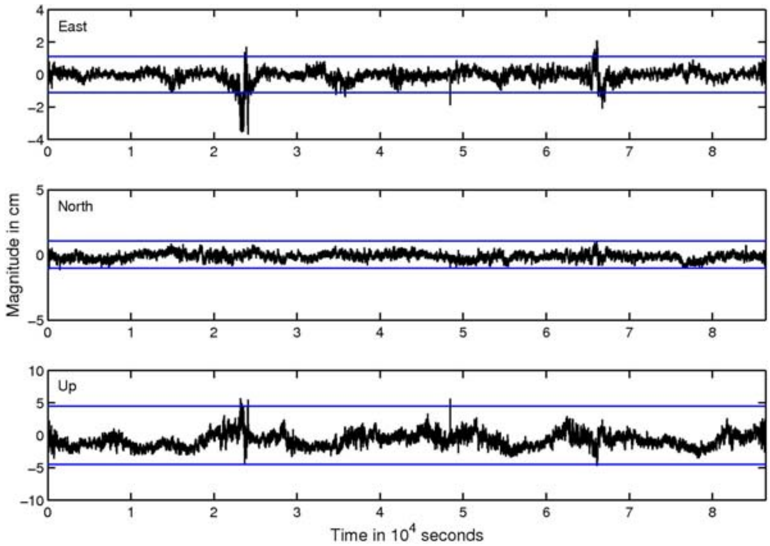

Fig. 5.12 Coordinates of Fig. 5.11 after applying the SIGMA-Δ model and bounds for outlier rejection indicated by horizontal lines.

Table 5.1 Statistics of coordinate series in the three directions before and after the SIGMA-Δ model is applied.

	East		North		Up	
	Before	After	Before	After	Before	After
Median (cm)	0.010	-0.022	-0.120	-0.140	0.520	-0.808
Outlier bounds (cm)	1.320	1.017	1.380	1.047	4.380	4.497
Number of outliers	1639	916	324	3	327	50

The results in Table 5.1 indicate that a great number of outliers are removed with the SIGMA-Δ model. The percentage of outliner reduction after applying the SIGMA-Δ model is about 44%, 99% and 85% for the East, North and up directions respectively. The relatively poor performance of the East component is considered to be caused by the bad satellite configuration as shown in Fig. 5.13. It can be seen from Fig. 5.13 that the abnormal values in the East component correspond to periods of fewer available satellites and higher horizontal dilution of precision (HDOP).

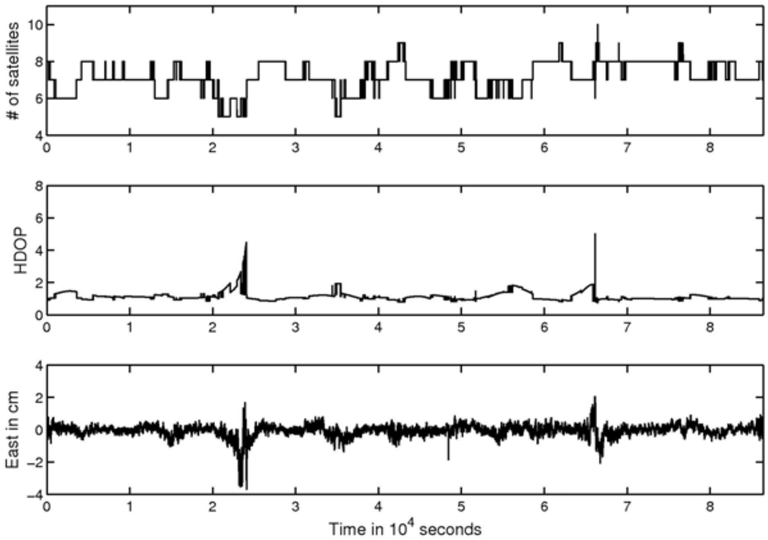

Fig. 5.13 Number of satellites, horizontal dilution of precision (HDOP), and East coordinate component with signal diffraction removed.

To illustrate the frequency characteristics of the coordinate series before and after applying the SIGMA-Δ model, Fig. 5.14 shows the power spectral density (PSD) estimates constructed as Welch averaged periodograms (Welch, 1967) using multiple sections (with no overlap) and a Hanning taper. It is seen from Fig. 5.14 that the PSD is almost kept unchanged at frequencies between 0.002 Hz and 0.1 Hz, whereas it is slightly reduced outside the frequency range. This indicates that using the SIGMA-Δ model can not only reduce significantly the signal diffraction, but can also retain the major GPS multipath signals with periods from tens of seconds to tens of minutes (see Chapter 2).

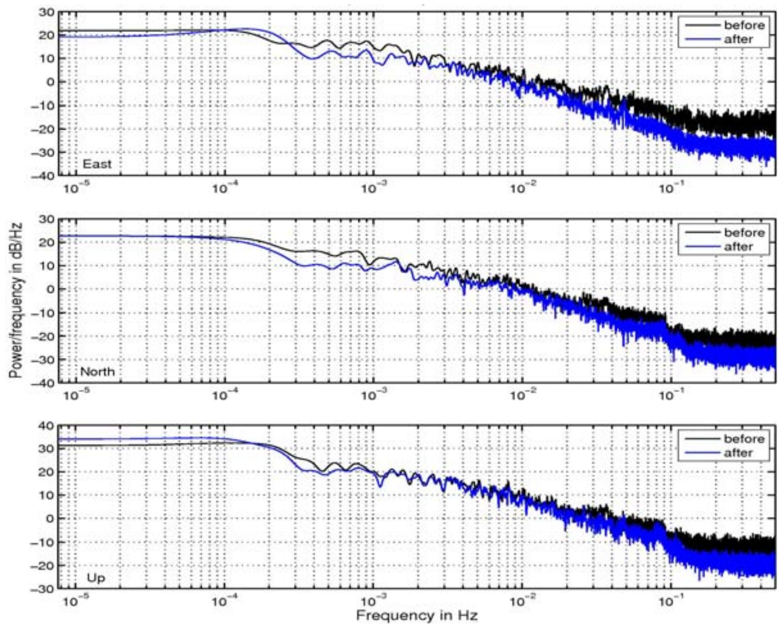

Fig. 5.14 PSD of coordinate series in the East, North and up directions before and after the SIGMA-Δ model is applied.

5.5.3 Coordinates from SIGMA-Δ, CVVF and ARTA

The coordinate series from DOY 323 to 350 after implementing the SIGMA-Δ, CVVF and ARTA techniques are shown below to give a visual presentation of the results. Offsets of 6 cm, 3 cm and 12 cm are added to the East, North and up components respectively, for separating the time series. Figures 5.15, 5.16 and 5.17 show the coordinate series for all three components after using the SIGMA-Δ model. Visual inspection of Figs. 5.15, 5.16 and 5.17 indicates that coordinate series repeat largely themselves over a time period of about one month, although not exactly. It is considered that the signals in the coordinate series are caused mainly by multipath.

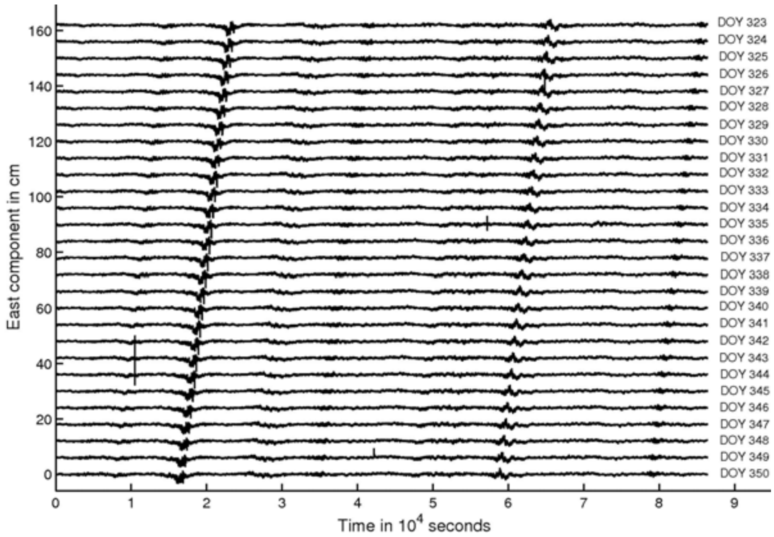

Fig. 5.15 Coordinate series for the East component from DOY 323 (top) to 350 (bottom) after the SIGMA-Δ model is applied.

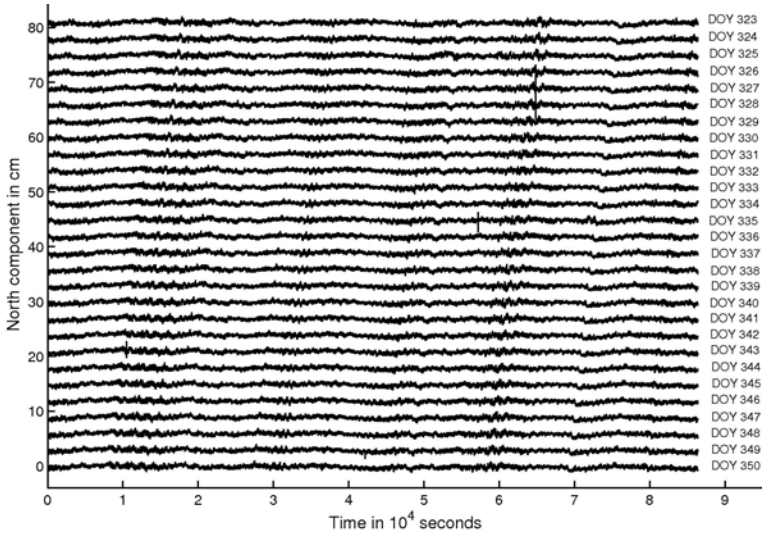

Fig. 5.16 Coordinate series for the North component from DOY 323 (top) to 350 (bottom) after the SIGMA-Δ model is applied.

Here accurate multipath models were established by filtering the first day's coordinate series (DOY is 322) with the CVVF method as discussed in Chapter 4 and are then removed from the coordinate series of subsequent days by using the ARTA method. The difference series are shown in Figs. 5.18, 5.19 and 5.20 for the East, North and up components respectively. It can be seen from Figs. 5.18, 5.19 and 5.20 that the multipath signals are mitigated significantly.

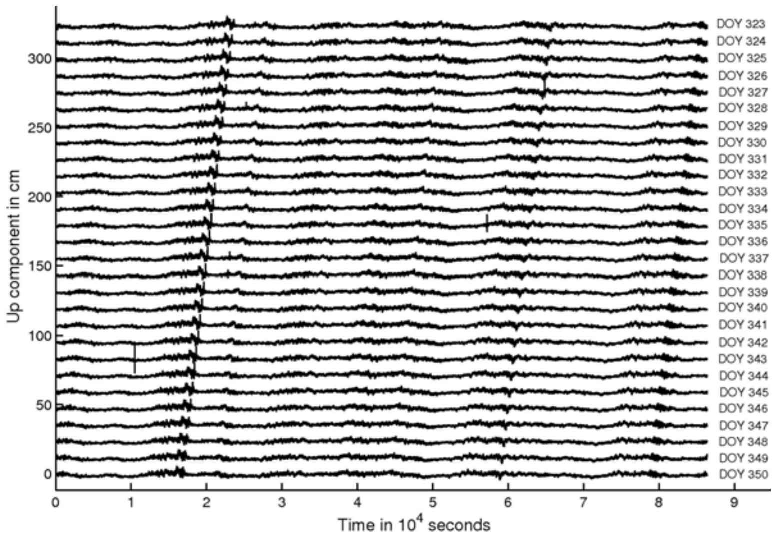

Fig. 5.17 Coordinate series for the up component from DOY 323 (top) to 350 (bottom) after the SIGMA-Δ model is applied.

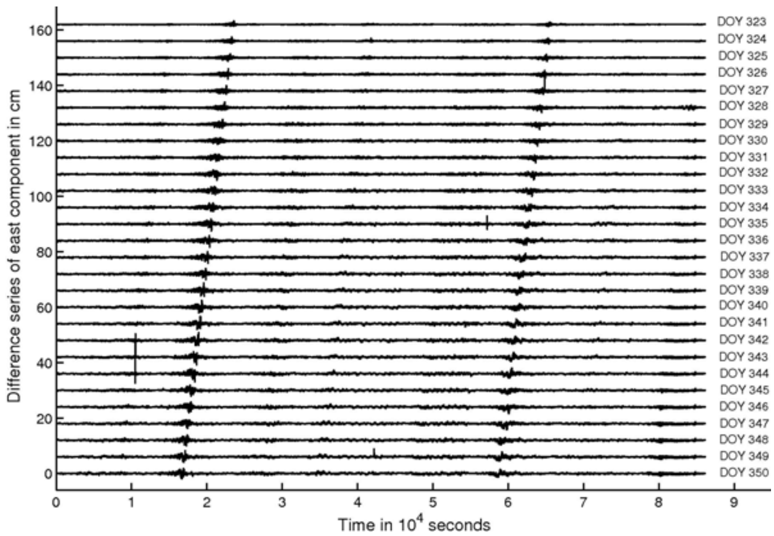

Fig. 5.18 Difference series for the East component from DOY 323 (top) to 350 (bottom) after the CVVF and ARTA methods are applied.

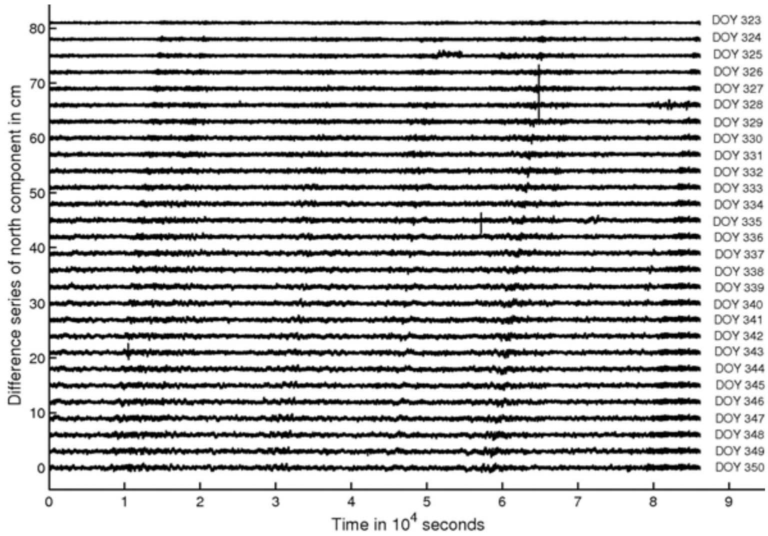

Fig. 5.19 Difference series for the North component from DOY 323 (top) to 350 (bottom) after the CVVF and ARTA methods are applied.

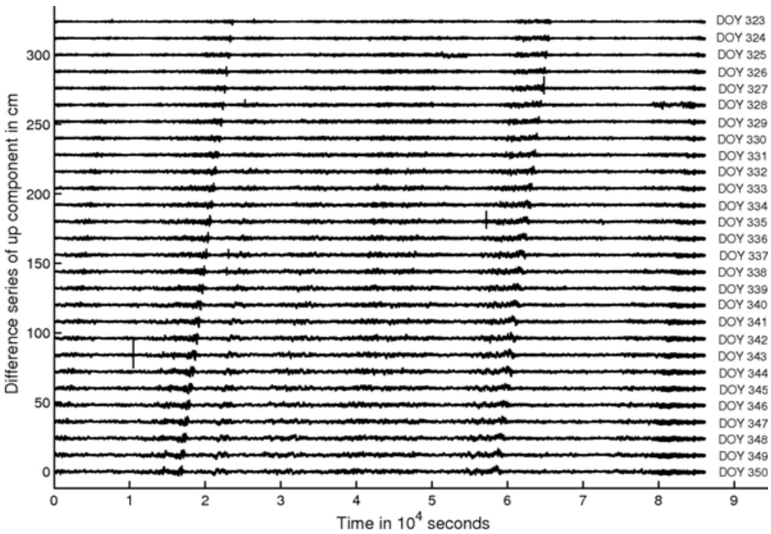

Fig. 5.20 Difference series for the up component from DOY 323 (top) to 350 (bottom) after the CVVF and ARTA methods are applied.

5.5.4 Accuracy Improvements

To obtain further insights into the performance of the method integrating the SIGMA-Δ, CVVF and ARTA, this section uses the standard data stacking technique

(Bock et al., 2000) to estimate the GPS accuracy improvements before and after applying the SIGMA-Δ model and compares them with the results of the ARTA method after the SIGMA-Δ is applied. The stacking algorithm is to shift entirely the coordinate series of multipath model according to a single shift and to correct the coordinate series of subsequent days. Here the single shift is determined by minimizing the RMS difference for a range of shifts (e.g. 236-256 s). In the following discussion, the CVVF method is used to establish multipath signal models for both the stacking and ARTA methods; thus it is not referred to in the comparison. The comparative results of accuracy improvements for the three directions are shown in Fig. 5.21.

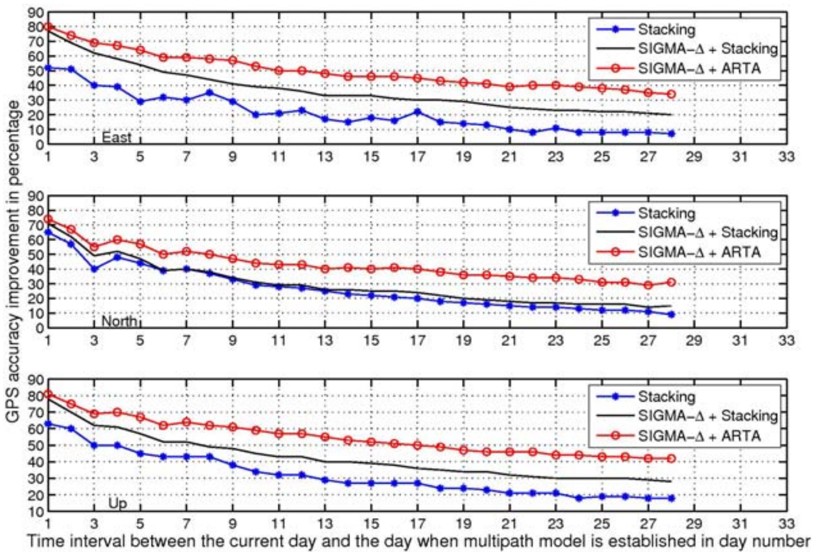

Fig. 5.21 Relationship between the GPS accuracy improvements and the time intervals between the current day and the day when the multipath model was established for the East, North and up directions after applying the different methods.

It is seen from Fig. 5.21 that the method of stacking exhibits the worst performance.

This is due to the effects of signal diffraction in the original coordinate series. The use of stacking after the SIGMA-Δ model can improve the accuracy by about 16%, 3% and 11% on average for the East, North and up directions respectively. The proposed method gives the best performance, leading to further improvements in accuracy of about 13% on average over the three directions when compared to stacking after the SIGMA-Δ.

It is also seen from Fig. 5.21 that the method of stacking after the SIGMA-Δ shows better performance over stacking when the time interval between the current day and the day when the multipath model was established is shorter than 5 days; while the method of ARTA after the SIGMA-Δ is better than stacking after the SIGMA-Δ for time intervals greater than 5 days. This indicates that the SIGMA-Δ model and the ARTA method are more effective for relatively short and long time intervals respectively.

To examine the accuracy improvements in the frequency domain, Figs. 5.22, 5.23 and 5.24 show the East, North and up components wavelet spectra respectively, for DOY 336 (14-day time interval) and 350 (28-day time interval) after applying the different methods discussed above.

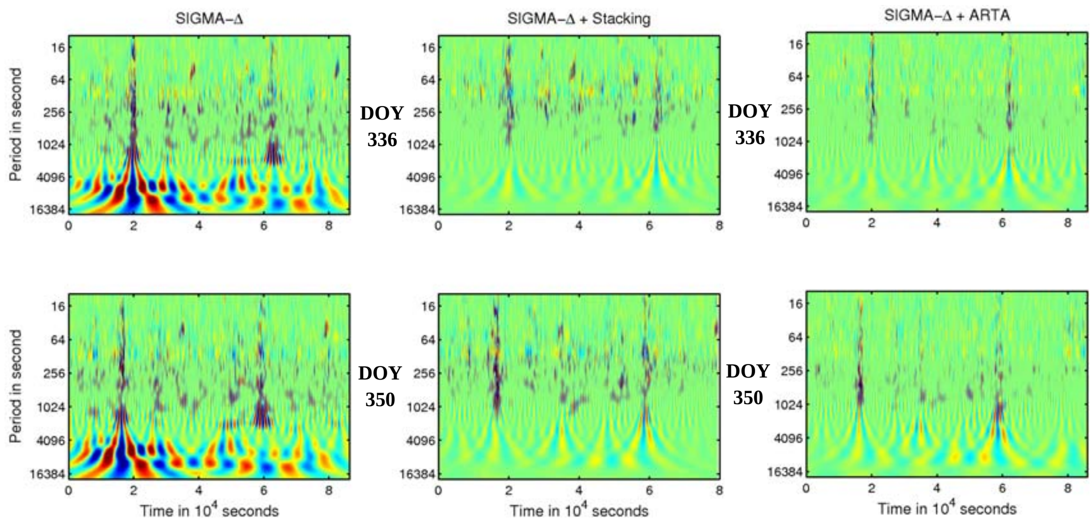

Fig. 5.22 East component wavelet spectra for DOY 336 and 350 after applying the SIGMA-Δ model (left), stacking after the SIGMA-Δ (middle) and ARTA after the SIGMA-Δ (right).

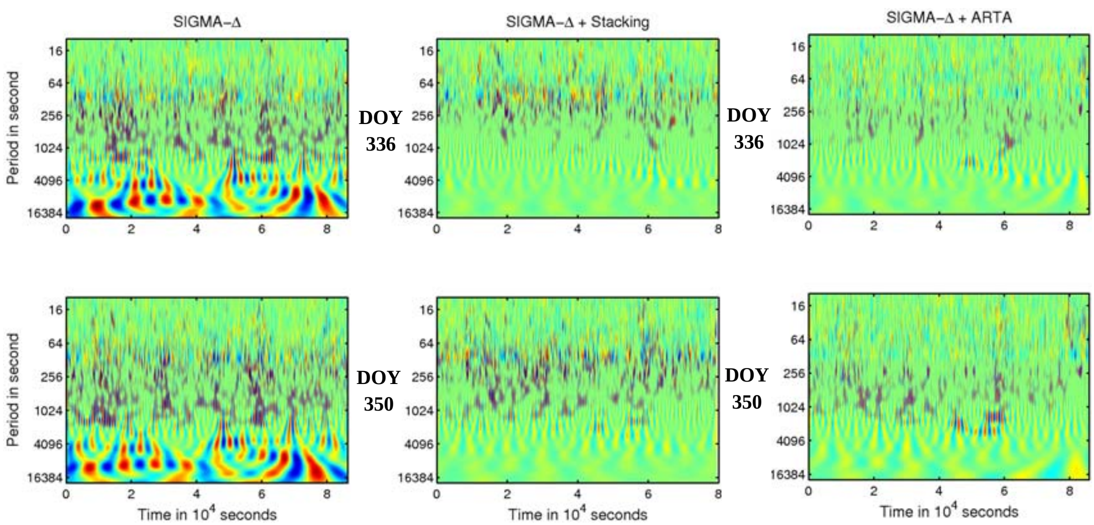

Fig. 5.23 North component wavelet spectra for DOY 336 and 350 after applying the SIGMA-Δ model (left), stacking after the SIGMA-Δ (middle) and ARTA after the SIGMA-Δ (right).

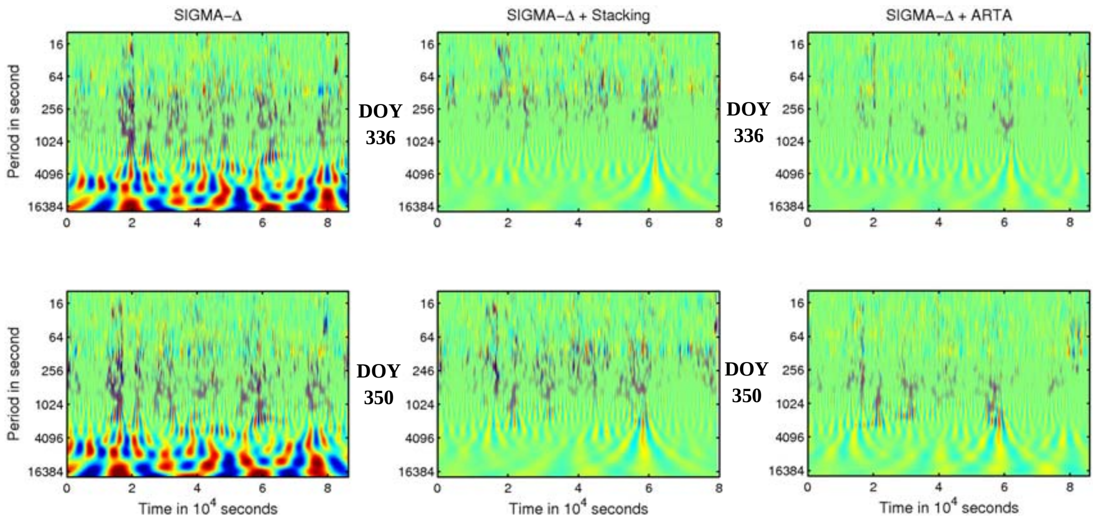

Fig. 5.24 Up component wavelet spectra for DOY 336 and 350 after applying the SIGMA-Δ model (left), stacking after the SIGMA-Δ (middle) and ARTA after the SIGMA-Δ (right).

It can be seen from Figs. 5.22, 5.23 and 5.24 that the signals with short periods (e.g. less than 1000 s) remaining in the wavelet spectra are more for DOY 350 than for DOY 366 after using the stacking or ARTA after the SIGMA-Δ model. This implies that the greater the time interval, the weaker the correlation of short-period multipath signals.

It can also be seen from Figs. 5.22, 5.23 and 5.24 that the method of stacking reduces mainly the multipath effects with long periods (e.g. greater than 1000 s); whereas the ARTA after the SIGMA-Δ can mitigate further the multipath with short periods compared to stacking after the SIGMA-Δ. This indicates that the proposed method is more effective than stacking in mitigating the effects of both short and long-period multipath.

5.6 Conclusions and Discussions

To maximize GPS accuracy improvements over a time period of tens days, this chapter has proposed to use the current SIGMA-Δ model to reduce the diffraction errors, followed by establishing a multipath signal model with the CVVF method and then reducing the multipath effects using the ARTA method. The following conclusions can be drawn based on the study:

(1) The use of the SIGMA-Δ model before making use of the repeating property of multipath signals can reduce significantly the diffraction effects while at the same time retaining the main multipath signals.

(2) The correlation of the multipath signals decreases with the increase of time interval between the current day and the day when the multipath model was established. The shorter the period of multipath signal, the weaker the correlation. The integrated use of the CVVF, SIGMA-Δ and ARTA methods can mitigate effectively the effects of both short and long-period multipath.

(3) The stochastic SIGMA-Δ model is more applicable to improve the accuracy of observations over a short time period (e.g. less than several days); whereas the ARTA method is more applicable to observations over a relatively long time period (e.g. tens of days). The integrated use of the CVVF, SIGMA-Δ and ARTA methods can improve the GPS accuracy by about 16-29% on average over the traditional stacking.

Chapter 6

Sidereal Filtering Based on GPS Single Difference for Mitigating the Effects of Multipath and Diffraction

6.1 Introduction

Since the relative geometry of a GPS satellite with respect to an antenna repeats itself approximately every sidereal day (nominally 23 h 56 m 04 s), multipath errors are highly correlated over successive sidereal days, and it is possible to use the “sidereal” satellite repeat period to mitigate these errors (Genrich and Bock, 1992; Bock et al., 2000; Nikolaidis et al., 2001). Following the discussion in Chapter 5, it can be seen that the GPS orbital repeat period varies for each satellite and differs from the nominal sidereal period (86,164 s) by ~ 8 seconds throughout the year. Choi et al. (2004) demonstrated that the use of the mean orbit repeat periods as the optimal time shift within the coordinate residuals achieved better results than the use of the sidereal period. However, it is not obvious which time shift to use when different satellites are visible at different times of the day, as this results in the mean orbit repeat time varying. It is therefore preferable if the multipath effects can be removed on a satellite-by-satellite basis.

Larson et al. (2007) developed an aspect repeat time adjustment (ARTA) method, using GPS coordinate series to estimate time-varying and site-dependent shifts. However, the limitation of this technique is that it cannot be used in real-time applications such as deformation monitoring.

One technique uses the signal-to-noise ratio (SNR) or carrier-to-noise power-density (C/N_0) recorded in the observational data file to reduce the errors of multipath or signal diffraction (Axelrad et al., 1996; Comp and Axelrad, 1998; Hartinger and Brunner, 1998). Although these methods can improve the accuracy of GPS positions, a potential drawback is that SNR or C/N_0 is not always available at the receiver, which makes it inapplicable in many situations.

Another technique of extracting and eliminating GPS carrier-phase multipath is to use the double-difference residuals series (Satirapod and Rizos, 2005; Ragheb et al., 2007). The main limitation here is that the reference satellite is not always present in the sky, making it difficult to use the method.

In this chapter, a filtering method, based on satellite-specific single difference observables, is developed for mitigating the effects of multipath and diffraction. We use data from short baselines over which errors from satellite and receiver clocks, satellite orbits, and atmospheric delay may be assumed to cancel out when using double difference observables. First the method of converting GPS double differences into single differences is briefly described. Then the filtering procedure based on single differences is proposed. Since the proposed method very much depends on the validity and accuracy of single differences, the method of obtaining single differences from double differences is validated by using simulated GPS data.

Finally, the proposed method is applied to real GPS data and compared with the standard data stacking method. The comparative results and analysis are also presented.

6.2 Obtaining Single Differences from Double Differences

Double differencing is commonly used in high accuracy GPS applications. Let ϕ_A^1 and ϕ_A^2 be observations of satellites 1 and 2 by receiver *A*, and ϕ_B^1 and ϕ_B^2 be observations by receiver *B*. Two single differences can be formed from these four observations,

$$s_{AB}^1 = \phi_A^1 - \phi_B^1 \tag{6.1}$$

$$s_{AB}^2 = \phi_A^2 - \phi_B^2 \tag{6.2}$$

A double difference dd_{AB}^{12} can be obtained by differencing the two single differences

$$dd_{AB}^{12} = (\phi_A^1 - \phi_B^1) - (\phi_A^2 - \phi_B^2) = s_{AB}^1 - s_{AB}^2 \tag{6.3}$$

For short baselines (e.g. shorter than 1 km), satellite and receiver clock biases are eliminated, and orbital and atmospheric errors are largely cancelled when forming the double-difference observations. However, some other errors, such as multipath, may not be removed with the differencing method due to its spatial uncorrelation characteristics.

In order to obtain single differences from double differences, the double difference, *dd*, can be written as the product of a matrix *D* and a vector of single difference, *s*,

$$Ds = dd \tag{6.4}$$

If there are *n* single differences, then only *n*-1 linearly independent double differences can be formed and the matrix *D* cannot be inverted. However, if an independent constraint on at least one of the single differences is added, as shown in Equation (6.5), then *D* has a well defined inverse (Alber et al., 2000).

$$\begin{bmatrix} w_1 & w_2 & w_3 \ldots w_n \\ 1 & -1 & 0 \ \ldots \ 0 \\ 1 & 0 & -1 \ \ldots \ 0 \\ & \ldots & \\ 1 & 0 & 0 \ \ldots -1 \end{bmatrix} \begin{bmatrix} s_{AB}^1 \\ s_{AB}^2 \\ s_{AB}^3 \\ \cdots \\ s_{AB}^n \end{bmatrix} = \begin{bmatrix} w_1 s_{AB}^1 + \ldots + w_n s_{AB}^n \\ s_{AB}^1 - s_{AB}^2 \\ s_{AB}^1 - s_{AB}^3 \\ \cdots \\ s_{AB}^1 - s_{AB}^n \end{bmatrix} = \begin{bmatrix} \sum w_i s_{AB}^i \\ dd_{AB}^{12} \\ dd_{AB}^{13} \\ \cdots \\ dd_{AB}^{1n} \end{bmatrix} \tag{6.5}$$

where $\sum w_i s_{AB}^i$ is the additional constraint and w_i is the satellite-dependent weighting for the site pair *AB*.

In this chapter, the post-fit double difference residuals are used in Equation (6.5), then setting the sum $\sum w_i s_{AB}^i$ equal to zero produces an inverse where the single differences remain the un-modelled part of the double differences. The un-modelled errors are caused mainly by multipath effects for short baseline applications. Since the amplitude attenuation factor (α) shown in Chapter 2 is stronger at low satellite elevation angles due to the gain pattern of a GPS antenna, data from low-elevation satellites therefore show much stronger multipath effects than data from high-elevation satellites (Larson et al., 2007). To downweight the single differences at low angels, a weighting function $w(\theta)$ is adopted as follows,

$$w(\theta) = \sin^2(\theta) \tag{6.6}$$

where θ is the satellite elevation angle.

6.3 Sidereal Filtering Based on Single Differences

The implementation of the proposed filtering method includes four main steps.

Step 1: Fix the coordinates of the unknown station and process the data to yield post-fit double-difference carrier-phase residuals for all independent satellite pairs at each observational epoch.

Step 2: Convert double-difference residuals into single-difference residuals epoch by epoch using the method discussed in Section 6.2.

Step 3: Establish a multipath model by using one day's single-difference residuals with diffraction effects removed if they exist. Then the multipath model is shifted and subtracted from single-difference residuals of the subsequent days on an epoch-by-epoch and satellite-by-satellite basis. Here the shift time of each satellite is determined by the sum of the orbital repeat periods over consecutive days.

Step 4: Resolve the final coordinates based on an ambiguity resolution and the double-difference residuals reconstructed by the corrected single-difference residuals.

A block diagram showing the GPS data filtering procedure is presented in Fig. 6.1. For convenience of reference, the proposed filtering method based on GPS single differences will be termed "single-difference filtering" (or SD filtering for short).

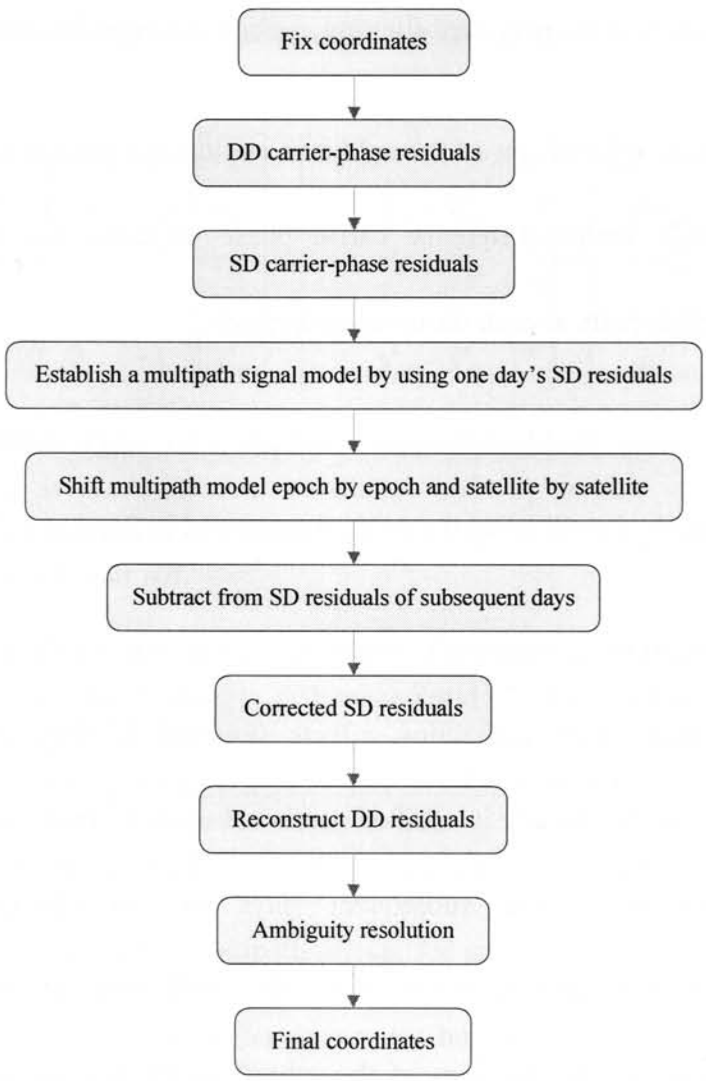

Fig. 6.1 Filtering procedure for mitigating the effects of signal multipath and

diffraction (DD: double-difference; SD: single-difference).

6.4 Simulation Studies

The effectiveness of the SD filtering method greatly depends on the validity and accuracy of the single differences converted from double differences. Here the simulated GPS data are used to validate the proposed method by comparing the converted single differences with simulated ones.

6.4.1 GPS Data Simulator

The 30-satellite GPS constellation (satellite identification number from 1 to 30) is simulated using parameters of perfectly circular Keplerian orbits. The small perturbations associated with the actual satellite orbits are ignored for simulation simplicity. Error-free pseudoranges can be generated for all visible satellites. Errors such as atmospheric delay, multipath error and measurement noise are then added to the true ranges to produce ‘measured’ code and phase pseudoranges.

The traditional raised half-cosine profile for zenith delay and elevation angle-dependent oblique factors are used to simulate ionospheric bias. The modified Hopfield model is used to simulate tropospheric delay. Multipath error at zero-elevation angle is modelled by coloured noise, created by passing white noise through a first-order Butterworth low-pass filter. The zero-angle multipath error is then scaled by the cosine of the true satellite elevation angle before it is applied to the range measurement. Random noise with normal distribution is used to simulate the measurement noise. More details of the GNSS data simulation can be found in Chapter 7.

6.4.2 Analysis of Results of Simulation Studies

GPS data have been simulated for two stations that were about 1.5 km apart over a period of one hour. The satellite elevation cutoff angle was set to 15° and the sampling rate was 1 Hz. Figure 6.2 illustrates the sky plot of the GPS satellites over the reference station.

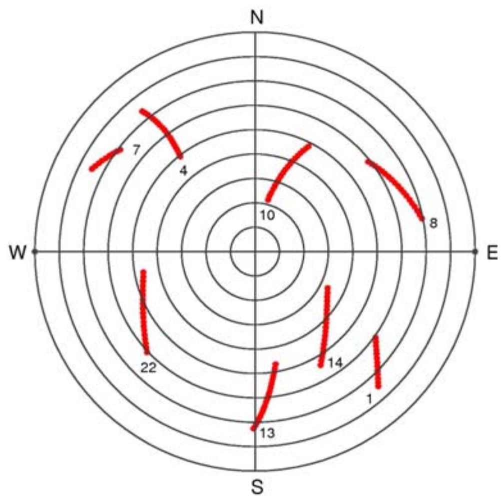

Fig. 6.2 Sky plot of GPS satellites over the reference station.

GPS satellite PRN 10 with the highest elevation angle is selected as the reference satellite when forming the double-differencing observations. Data from three satellites, PRNs 13, 14 and 22, are contaminated by multipath in our analysis. The single-difference carrier-phase residuals are obtained from the double-difference residuals by using the method discussed in Section 6.2. The converted single-difference residuals compared with the simulated single-difference residuals (without receiver clock error) for the multipath-free reference satellite and three multipath-contaminated satellites are shown in Fig. 6.3. An offset of 5 cm is added to each subplot to separate the time series.

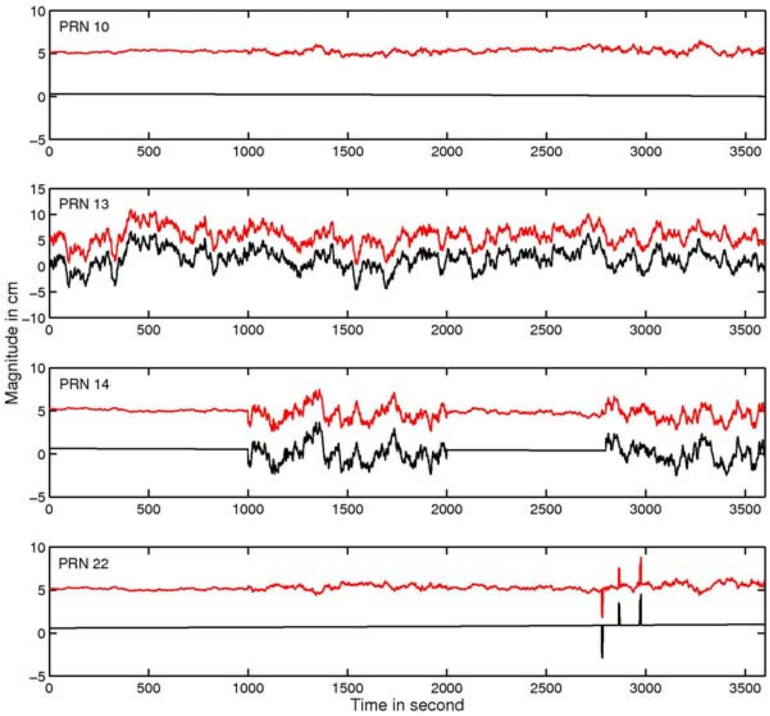

Fig. 6.3 Comparison of converted single-difference residuals (*top curve in each subplot*) with simulated values (*bottom curve in each subplot*) for reference satellite (PRN 10) and three multipath-contaminated satellites (PRN 13, 14 and 22).

It is seen from Fig. 6.3 that the calculated single-difference residuals are quite similar to the simulated ones. The differences between the converted and simulated single-difference residuals are considered to be caused by the weighting strategy. The root mean square (RMS) values of the differences are about ±0.3 cm for the four satellites, indicating that the weighing function adopted in this chapter (see Equation (6.6)) works well in all cases.

6.5 Experiments with Real GPS Data

GPS observations collected from the field experiments described in Chapter 5 are used to test the proposed SD filtering method. Data from 19 to 29 November 2005 (DOY from 323 to 333) are used with the satellite elevation cutoff angle set to 15°. Results from two tests with and without the effects of signal diffraction will be presented later. To clearly show the coordinates over the consecutive days, offsets of 5 cm, 4 cm and 12 cm will be added throughout this section to coordinate series of the East, North and up directions respectively, for separating the time series.

6.5.1 Test 1: Mitigating Multipath and Diffraction Effects

The coordinates of the rover antenna were estimated in a post-processing kinematic mode, where the ambiguities were fixed in the processing. Then the resolved coordinates were projected into a map grid system ENU (East, North, up). The results for a period of about three hours over the 11 consecutive days are shown in Fig. 6.4, 6.5 and 6.6 for the East, North and up directions respectively. The mean coordinates have been removed from the results for easy interpretation of the variations.

It is seen from Figs. 6.4, 6.5 and 6.6 that the coordinate series repeat largely themselves on the consecutive days with sudden changes appearing in the data series, but the day-to-day repeating property of some of the sudden changes is not obvious. After further inspection of the abnormal values, it is considered that they are caused by signal diffraction effects.

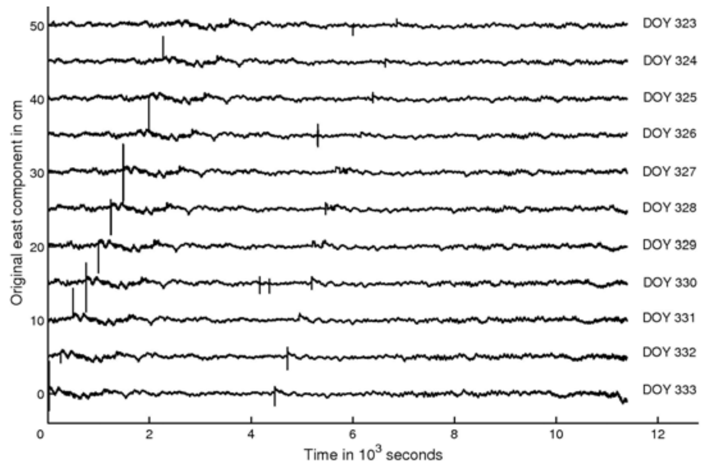

Fig. 6.4 Original coordinate series from DOY 323 (*top*) to 333 (*bottom*) in the East direction (test 1).

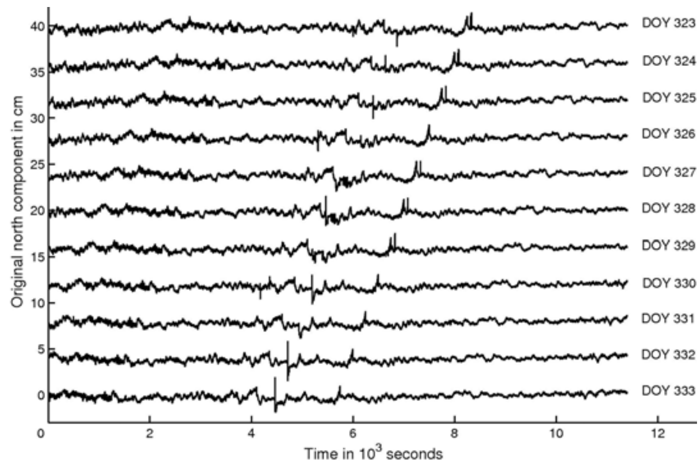

Fig. 6.5 Original coordinate series from DOY 323 (*top*) to 333 (*bottom*) in the North direction (test 1).

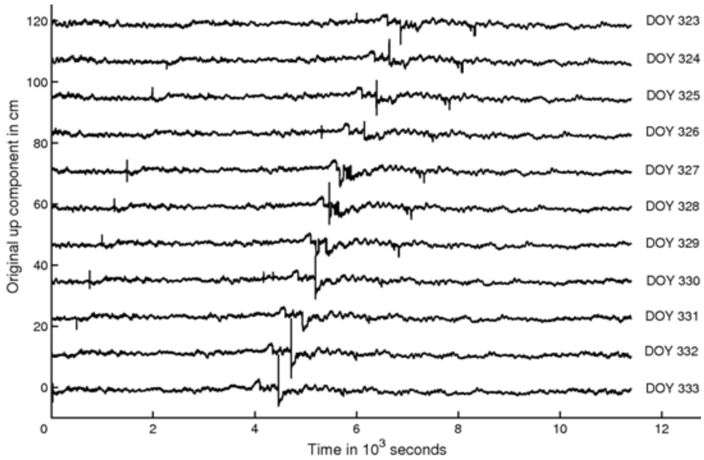

Fig. 6.6 Original coordinate series from DOY 323 (*top*) to 333 (*bottom*) in the up direction (test 1).

To establish a multipath model without the effects of signal diffraction, diffracted GPS satellites can be removed due to the fact that the diffraction signals are usually associated with low C/N_0 values (Brunner et al., 1999) or with satellites that are beginning to rise or fall into view. In this test, the diffracted GPS satellites were removed from the double-difference residuals of DOY 323 based on satellite elevation angles or signal strength in the observation file, and then converted them into the single-difference residuals to obtain the multipath model. Figure 6.7 shows the coordinate series on DOY 323 for all the three directions before and after the signal diffraction effects are removed. Offsets of 2 cm, 3 cm and 5 cm are again added to the East, North and up directions respectively, in order to separate the coordinate series.

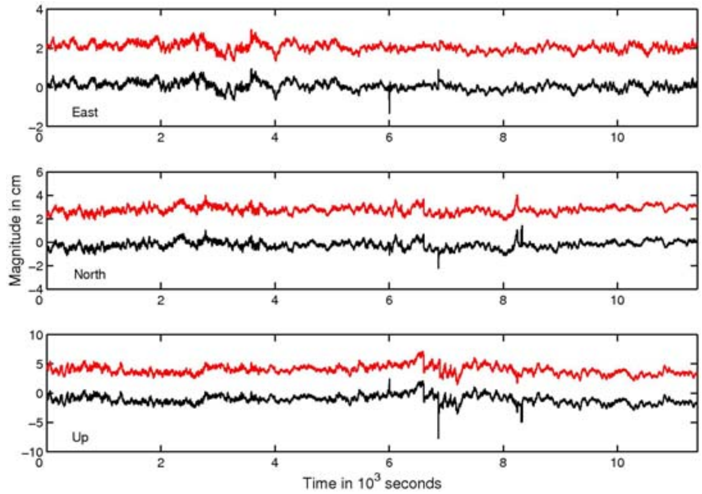

Fig. 6.7 Coordinate series on DOY 323 for the three directions before (*bottom curve in each subplot*) and after (*top curve in each subplot*) removing the diffraction effects.

The filtered coordinate series after implementing the SD filtering method are shown in Figs. 6.8, 6.9 and 6.10 for the three directions. In addition, to compare the proposed method with the standard data stacking technique (Bock et al., 2000), CVVF-filtered coordinate series of DOY 323 after removing the diffraction effects are used as the multipath model for the stacking (see details of the CVVF method in Chapter 4). The filtered coordinates, obtained by subtracting the multipath model of the stacking from the original coordinate series of DOY 324 to 333, are also shown in Figs. 6.8, 6.9 and 6.10 for comparison.

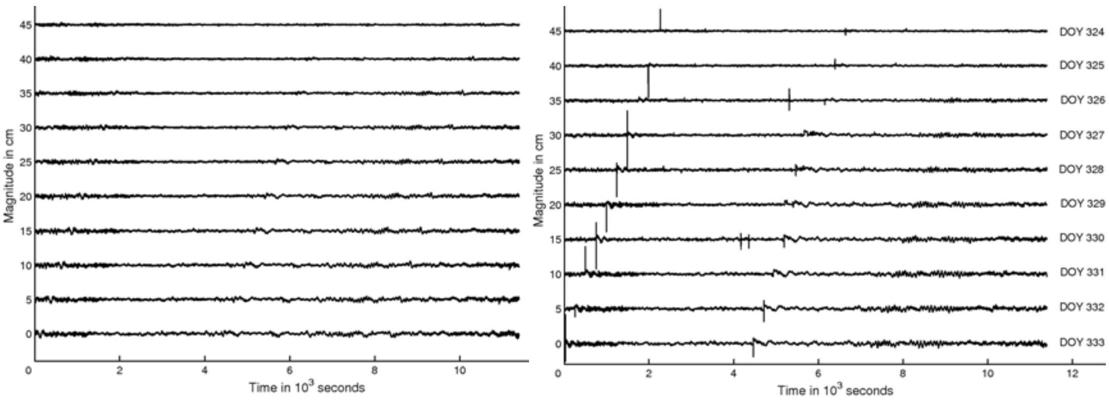

Fig. 6.8 Filtered coordinate series after applying the SD filtering method (*left panel*) and the stacking method (*right panel*) respectively from DOY 324 (*top*) to 333 (*bottom*) for the East direction, when the effects of signal diffraction exist.

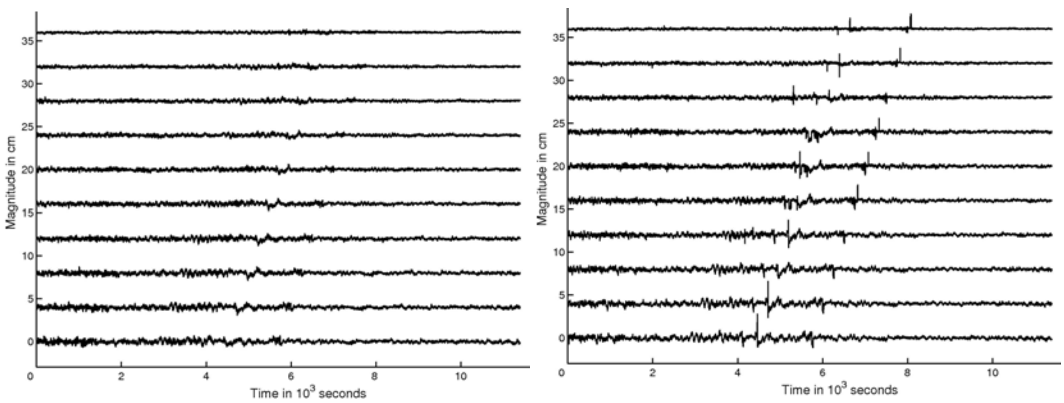

Fig. 6.9 Same as Fig. 6.8, except for the North direction.

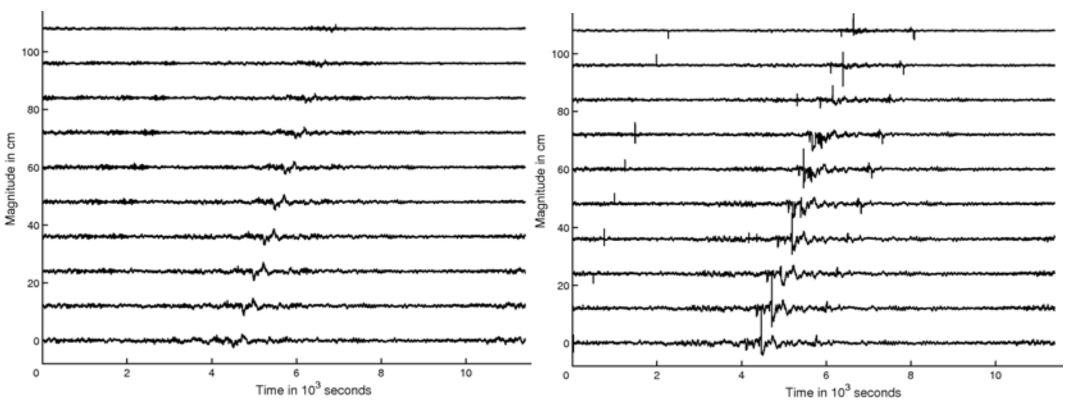

Fig. 6.10 Same as Fig. 6.8, except for the up direction.

It can be seen from Figs. 6.8, 6.9 and 6.10 that compared with the data stacking method, the SD filtering method can not only mitigate significantly the multipath effects, but almost completely remove the diffraction errors. The comparative results in accuracy improvements with these two methods will be presented later.

6.5.2 Test 2: Mitigating Multipath Effects

To obtain further insight into the performance of the proposed method when the signal diffraction effects are not present, a different dataset for a period of about one and a half hours over the same period of the consecutive 11 days is used. The original coordinate series are shown in Figs. 6.11, 6.12 and 6.13 for the East, North and up directions respectively.

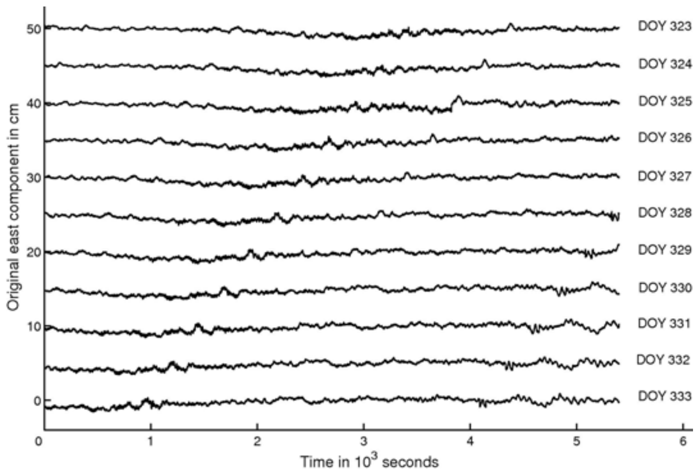

Fig. 6.11 Original coordinate series from DOY 323 (*top*) to 333 (*bottom*) in the East direction (test 2).

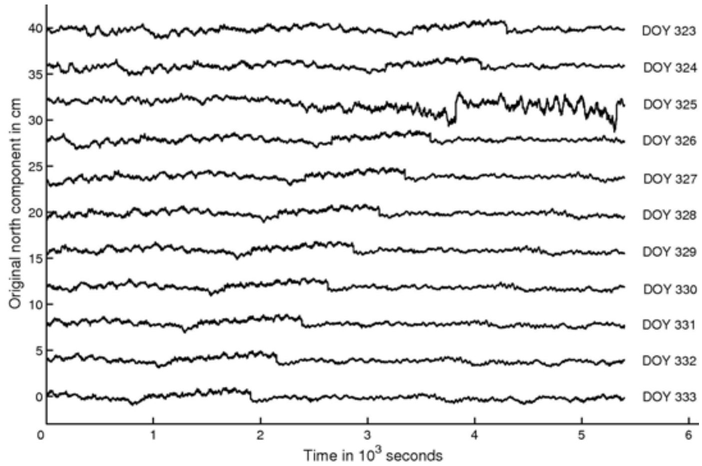

Fig. 6.12 Original coordinate series from DOY 323 (*top*) to 333 (*bottom*) in the North direction (test 2).

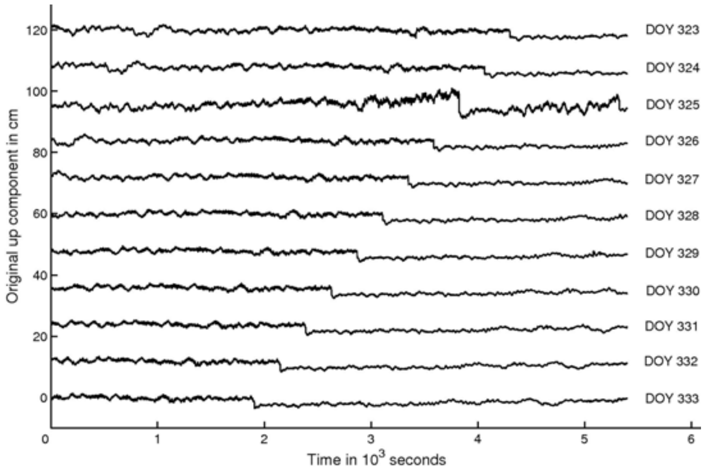

Fig. 6.13 Original coordinate series from DOY 323 (*top*) to 333 (*bottom*) in the up direction (test 2).

In this test, the multipath model for the SD filtering is established by using the single-difference residuals converted from the double-difference residuals on DOY 323; while that for the stacking method is obtained by filtering the coordinate series of DOY 321 to 323 with the CVVF method (Zheng et al., 2005) and then using the moving average technique (Bock et al., 2000). Figures 6.14, 6.15 and 6.16 show the filtered coordinate series for the East, North and up directions respectively, after the SD filtering and the stacking methods are applied.

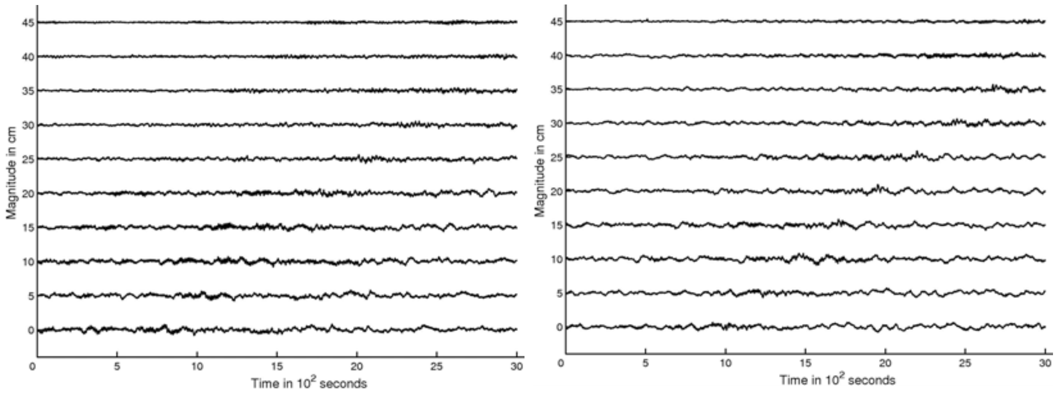

Fig. 6.14 Filtered coordinate series after applying the SD filtering method (*left panel*) and the stacking method (*right panel*) respectively from DOY 324 (*top*) to 333 (*bottom*) for the East direction, when the effects of signal diffraction do not exist.

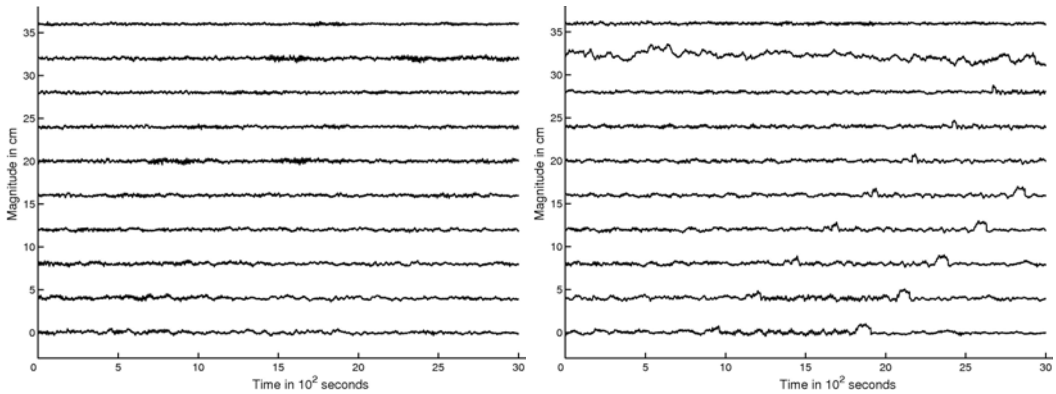

Fig. 6.15 Same as Fig. 6.14, except for the North direction.

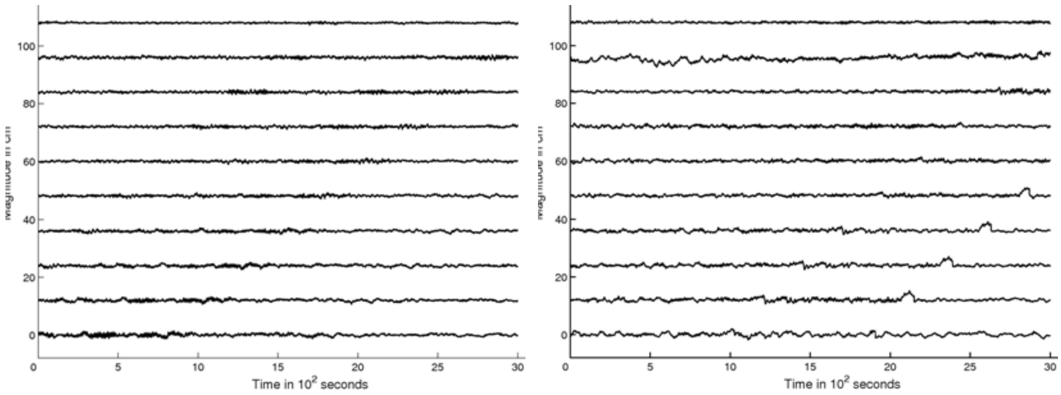

Fig. 6.16 Same as Fig. 6.14, except for the up direction.

Visual inspection of Figs. 6.14, 6.15 and 6.16 indicates that the filtered series after using the SD filtering method gives better results than using the stacking method. Further analysis on the reason for the better performance of the proposed method will be presented in the next section.

6.5.3 Comparative Analysis

RMS errors of the coordinate series in the East, North and up directions with and without applying the SD filtering method for the above two experiments are summarized in Tables 6.1 and 6.2 respectively. To show the effectiveness of the proposed method, the percentage improvement in 3D position accuracy with the SD filtering method is also given in Tables 6.1 and 6.2.

Table 6.1 RMS errors in millimeters before and after SD filtering method is applied, and 3D position accuracy improvements with the SD filtering method as a percentage (test 1).

DOY	East		North		Up		Improve-ment (%)	Improve-ment over stacking (%)
	Before	After	Before	After	Before	After		
324	2.408	0.651	3.228	0.687	7.807	1.589	83	42
325	2.194	0.802	3.192	0.888	7.787	2.141	77	34
326	2.125	0.938	3.139	1.024	7.593	2.647	71	19
327	2.307	1.058	3.368	1.122	8.286	2.981	72	61
328	2.262	1.125	3.259	1.193	7.925	3.313	65	44
329	2.294	1.242	3.179	1.302	7.959	3.545	63	43
330	2.356	1.368	3.087	1.431	7.623	3.790	58	32
331	2.297	1.446	3.134	1.546	7.812	4.030	57	32
332	2.252	1.535	3.175	1.608	7.868	4.082	57	38
333	2.527	1.647	3.257	1.725	7.920	4.192	57	42

It is seen from Table 6.1 that when GPS observations are affected by the diffracted signals, the reduction of RMS values of the 3D position errors ranges from 60% to 80% when the SD filtering method is applied. The results in Table 6.1 show that about 20–60% improvements in 3D position accuracy can be achieved with the proposed method, compared with the stacking method when the signal diffraction effects are present.

Table 6.2 RMS errors in millimeters before and after the SD filtering method is applied, and 3D position accuracy improvements with the SD filtering method as a percentage (test 2).

DOY	East		North		Up		Improve-ment (%)	Improve-ment over stacking (%)
	Before	After	Before	After	Before	After		
324	4.419	0.767	3.337	0.695	6.939	1.664	75	22
325	3.984	0.982	4.148	1.244	9.780	2.955	70	74
326	4.188	1.196	3.343	0.864	6.886	2.833	53	18
327	3.970	1.288	3.565	0.923	6.236	2.820	50	17
328	3.780	1.509	3.432	1.203	5.682	2.699	46	17
329	3.842	1.869	3.490	1.048	7.557	2.940	62	41
330	3.951	2.016	3.386	1.083	9.393	3.214	67	47
331	4.304	2.207	3.286	1.215	10.901	3.508	69	42
332	4.409	2.257	3.349	1.417	11.287	3.642	68	39
333	4.612	2.392	3.395	1.350	11.404	4.121	65	23

It is seen from Table 6.2 that the RMS values of the positioning errors in the three directions have been significantly reduced with the SD filtering method. The 3D position accuracy can be improved by about 50–75% with this method when signal diffraction effects do not exist.

It is also seen from Table 6.2 that the SD filtering method exhibits the best performance on DOY 325 when compared with the stacking method. As confirmed by NANUs (Notice Advisory to Navstar Users) messages, PRN 6 was manoeuvred during the observation period on DOY 325 and thus excluded from coordinate estimates. Figure 6.17 shows the number of satellites, vertical dilution of precision (VDOP) values and coordinate series in the up direction for the multipath model and DOY 325. The mean of the satellite numbers and VDOP values on DOY 321 to 323 is used as the number of satellites and VDOP of the multipath model respectively. An offset of 8 cm is added to the third subplot in Fig. 6.17 to separate the up coordinate series for clarity.

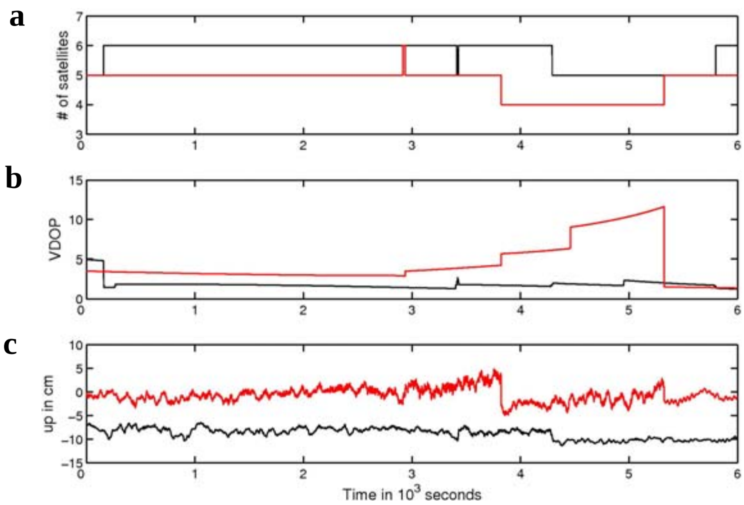

Fig. 6.17 a Number of satellites for multipath model (*top line*) and DOY 325 (*bottom line*); **b** VDOP values for multipath model (*bottom line*) and DOY 325 (*top line*); and **c** up coordinate components for multipath model (*bottom curve*) and DOY 325 (*top curve*) with offset of 8 cm added.

It can be seen from Fig. 6.17 that compared with the multipath model, fewer satellites on DOY 325 resulted in poorer satellite geometry indicated by the higher VDOP. The highest VDOP values were obtained when only four satellites are visible, corresponding to the large fluctuation of the coordinate series on DOY 325. Therefore, the coordinate series of DOY 325 is quite different from the multipath model. It is considered that the coordinate differences caused by missing GPS satellites can degrade the GPS accuracy when the stacking method is applied. The reason for the best performance of the SD filtering method on DOY 325 is due to this method working on a satellite-by-satellite basis; the missing PRN 6 is thus excluded in the final coordinate estimates. This indicates that the SD filtering method is more advantageous than the traditional stacking method in that it can effectively minimize the position errors when different satellites are viewed on each day.

Further analysis shows that although the same satellites were observed on DOY 324 to 333 (except for DOY 325) during the observation time period, the 3D position accuracy can be improved by about 20–40% with the SD filtering method over the stacking as shown in Table 6.2. To investigate the reason of the improved performance, Fig. 6.18 illustrates the comparison of satellite numbers and North coordinate components for the multipath model and DOY 330, and filtered coordinate series on DOY 330 after applying the stacking and the SD filtering methods. When the stacking is applied, the optimal shift time is determined by peak cross-correlation between the multipath model and the coordinate series on subsequent days. An offset of 1 cm is added to the fourth subplot in Fig. 6.18 to separate the time series for comparison.

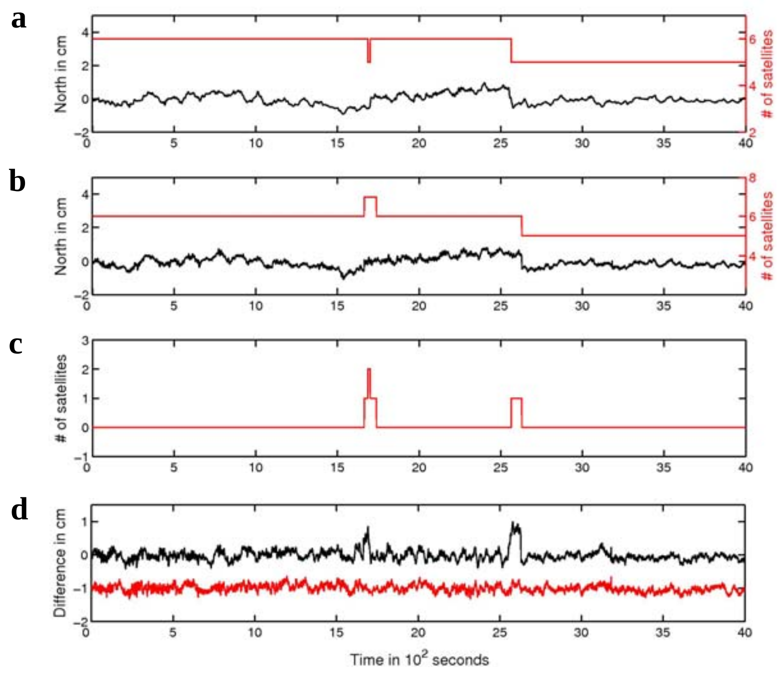

Fig. 6.18 a Number of satellite (*line*) and North coordinate component (*curve*) for multipath model; **b** number of satellite (*line*) and North coordinate components (*curve*) on DOY 330; **c** difference of satellite numbers between multipath model and DOY 330; and **d** filtered series on DOY 330 after using the stacking (*top curve*) and the SD filtering (*bottom curve*) methods with offset of 1 cm added.

It is seen from Fig. 6.18 that the two peaks in the filtered coordinate series after using the stacking method correspond to two non-zero differences of satellite numbers. It is considered that the left peak is due to different satellites being used in the position estimates for the multipath model and DOY 330, making some of the coordinates not exactly repeatable; while the right peak is caused by some of the GPS satellites not having been shifted by their optimal shift time. Since multiple satellites contribute to each coordinate, it is considered that the stacking method necessarily forces a compromise among the satellite-specific optimal time shifts. Compared to the SD filtering method, both peaks are removed from their filtered series, indicating that the proposed method can not only ensure the same satellites in position estimates, but also provide more precise results than the stacking by shifting each satellite by its individual shift time instead of a single time shift.

6.6 Conclusions

A sidereal filtering method based on GPS single difference observations has been proposed for mitigating GPS signal multipath and diffraction effects. Test results have shown that the new method can be used to effectively reduce these effects. The accuracy of GPS measurements can be improved by about 50–80% with the proposed method. Tests have also shown that about 20–60% improvements in GPS accuracy can be achieved with the proposed method when compared with the standard data stacking method. The new filtering method is more advantageous in that it is applicable when different satellites are observed on each day. It can not only exclude satellites that have just been manoeuvred from final position estimates, but also ensure the same satellites are used for the multipath model and subsequent coordinate series. The proposed method is more practical in that it can be implemented in real-time application such as deformation monitoring.

Chapter 7

Mitigation of GPS Multipath Effects Using Modernized GNSS Signals

7.1 Introduction

Although GPS has been widely used in high-accuracy positioning and navigation, the non-availability of GPS signals is a major limitation in high masked environment such as dense urban areas or deep open-pit valleys. Fortunately, the modernized GPS, GLONASS and Galileo will provide signals in more frequency bands (e.g. Galileo will transmit on four frequencies, namely E1, E5a, E5b and E6). With the interoperability of all these global navigation satellite systems (GNSS), more satellites in view can be expected to improve the accuracy of positioning. In recent years, much research has concentrated on the use of multiple-frequency GNSS data to improve the ambiguity resolution (e.g. Tiberius et al., 2002; Zhang et al., 2003; Schlotzer and Martin, 2005). Studies on multipath mitigation using multiple signals from the new GNSS have also been carried out by some researchers (Irsigler et al., 2004; Lau, 2004); however, little attention has been paid to GPS/GLONASS/Galileo integration. This is perhaps primarily due to the uncertain future of GLONASS since the first GLONASS satellite was launched in 1982. However, with the new Russian commitment to rebuild the system and the announcement of the provision of financial support from India at the end of 2004, it is worth considering such a scenario now.

This chapter investigates the influence of modernized GNSS signals on precise carrier phase positioning when the multipath effects are present. We first describe the modernized GNSS signals and the processing of GNSS data. A GNSS simulator is then introduced to simulate GNSS multiple-frequency data, followed by an assessment of the performance of standalone GPS and integrated GPS/GLONASS, GPS/Galileo and GPS/GLONASS/Galileo systems in multipath mitigation. Finally, comparative analysis and results for the different scenarios are presented.

7.2 GNSS Modernization

7.2.1 Modernized GPS Signals

Although GPS has performed extremely well in the past three decades, some significant improvements are needed to satisfy both military and civil users (McDonald, 2002). The first step in the GPS modernization process was the termination of Selective Availability (SA) in 2000. Modernized GPS will offer three additional signals, including two new civil signals (an L2 civil (L2C) signal and an L5 signal) and a new military signal (M code). L2C will be added on the L2 channel and broadcast by GPS Block IIR-M and Block IIF satellites, while L5 will be provided beginning with the first Block IIF satellite, and continuing with the Block III satellites expected for launch by 2013 (Alexander, 2006). At the time of writing (mid-2007), the GPS constellation consists of 30 Block II/IIA/IIR/IIR-M satellites. The present and new GPS signal structures and frequencies are shown in Fig. 7.1.

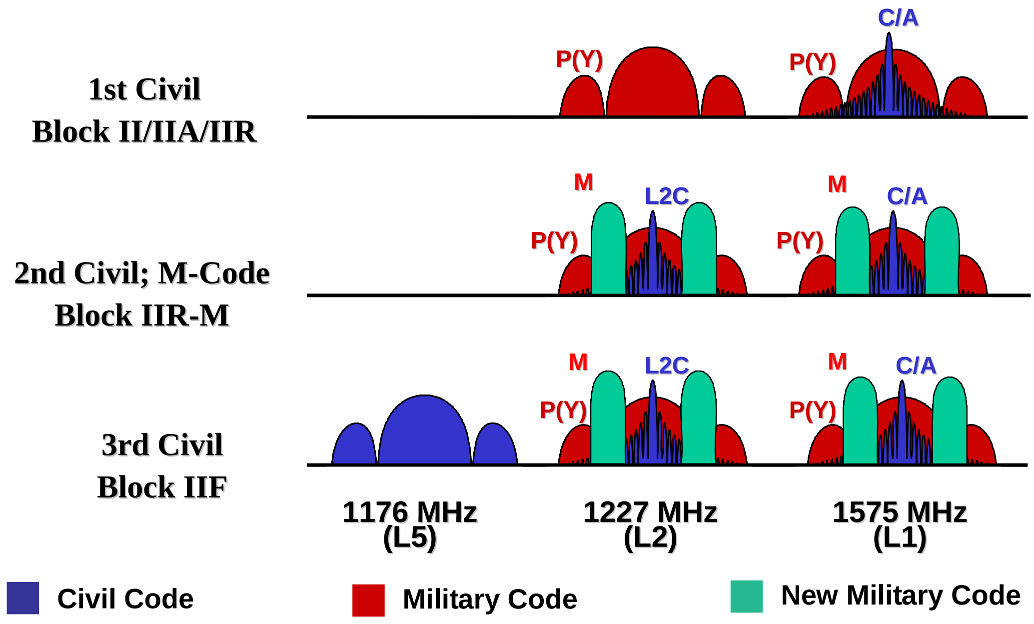

Fig. 7.1 GPS frequencies and signal structure (ICD-GPS-200C, 2003).

7.2.2 Replenishment of GLONASS

Several new generations of modernized GLONASS satellites are currently being developed to replenish the constellation. The new GLONASS-M spacecraft (a modernized version of the GLONASS spacecraft) was first launched in 2003. Compared with the GLONASS spacecraft, the L2 signal is modulated with the civil code on GLONASS-M. At the time of writing (mid-2007), three GLONASS-M satellites launched in December 2006 have brought the number of operational GLONASS satellites to 17. A total of 10 to 12 GLONASS-M satellites will be launched over the next several years until the design and production of the next generation of satellites, GLONASS-K, are completed (Kaplan and Hegarty, 2006). The GLONASS-K spacecraft is projected to be much smaller, with half the weight and a longer lifetime. The new GLONASS-K spacecraft series is planned to start launching in 2008. Figure 7.2 shows the GLONASS constellation history and the plans for replenishment.

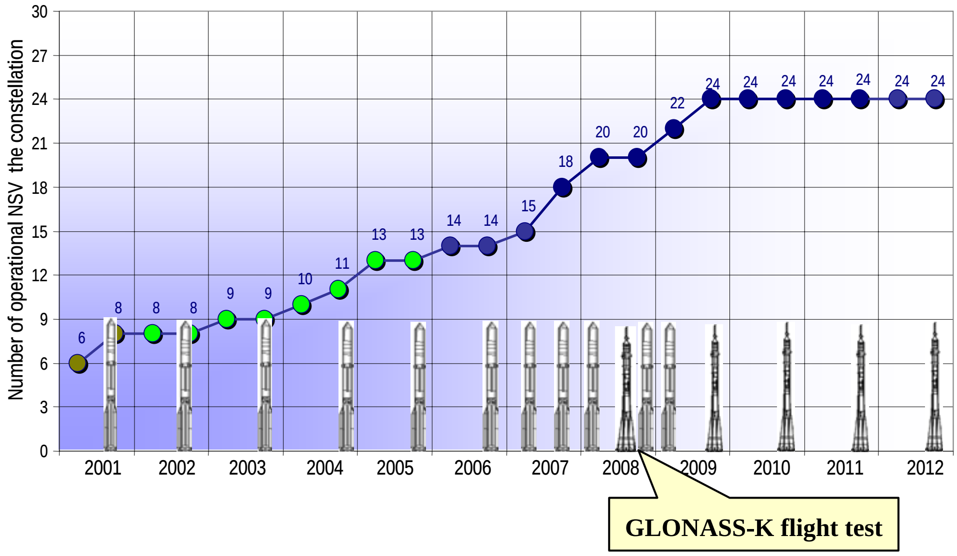

Fig. 7.2 GLONASS constellation history and plans for replenishment (Averin, 2006).

7.2.3 Galileo Development

Galileo is being developed to comprise 27 operational satellites that transmit 10 signals in the four frequency bands indicated in Fig. 7.3. These are 1164-1215 MHz (E5a band and E5b band), 1260-1300 MHz (E6 band) and 1559-1591 MHz (L1 band). They provide a wide bandwidth for the transmission of the Galileo signals. Six signals will be open to all civil users on L1, E5a and E5b for Open Service (OS) and Safety-of-Life Service (SoL). Two signals on E6 with encrypted ranging code are only accessible to users of Commercial Service (CS). Two signals (one in E6 band and one in L1 band) with encrypted ranging code and data will be accessible to authorized users of the Pubic Regulated Service (PRS) (Hein, 2002). The Full

Operational Capability (FOC) of Galileo is scheduled for 2010.

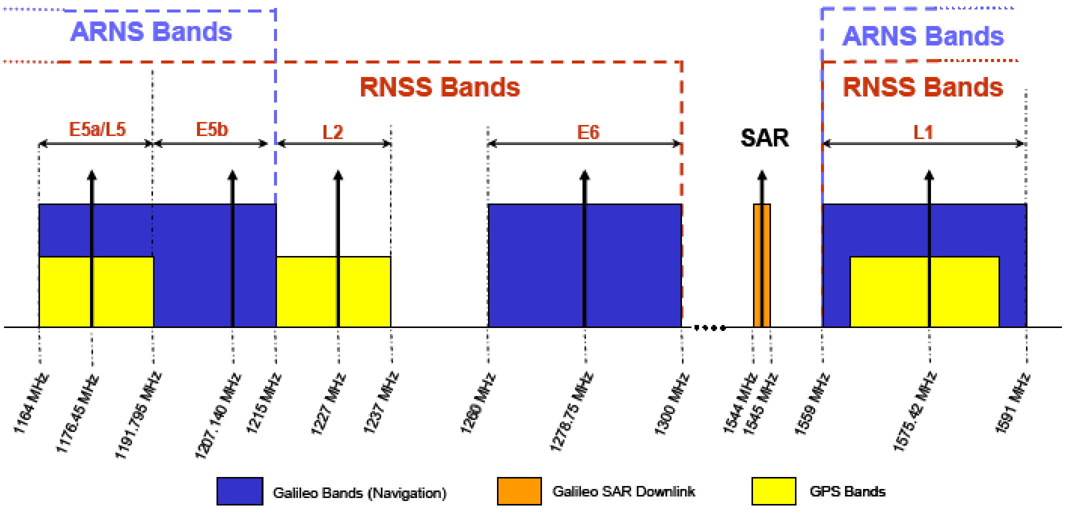

Fig. 7.3 Galileo Frequency Plan (ESA and GJU, 2006).

7.3 GNSS Data Processing

Since the encrypted data are not accessible to all users, the civilian Galileo signals on L1, E5a and E5b are only considered. The carrier frequencies of GPS, GLONASS and Galileo used in this chapter are shown in Table 7.1. To investigate the impact of multipath effects on different GNSS or combinations of frequencies, the five scenarios shown in Table 7.2 will be analysed.

Table 7.1 Carrier frequencies of civilian GPS, GLONASS and Galileo (k is the channel number).

GPS	Carrier frequency (MHz)	GLONASS	Carrier frequency (MHz)	Galileo	Carrier frequency (MHz)
L1C	1575.42	L1	$1602.0 + 0.5625k$	L1	1575.42
L2C	1227.60	L2	$1246.0 + 0.4375k$	E5a	1176.45
L5	1176.45	-	-	E5b	1207.14

Table 7.2 Scenarios with different GNSS or combinations of frequencies.

Scenario	Description in brief	Description in detail
1	SF GPS	GPS signals on L1
2	TF GPS	GPS signals on L1, L2 and L5
3	GPS/GLONASS	GPS three-frequency and GLONASS dual-frequency
4	GPS/Galileo	GPS three-frequency and Galileo three-frequency
5	GPS/GLONASS/Galileo	All civilian signals of GPS, GLONASS and Galileo

The double-difference least squares solution on an epoch-by-epoch basis is used to process the multiple-frequency GNSS data in the analysis, where the ambiguities are pre-determined by using the simulated error-free ‘measurements’. Single-difference (SD) carrier phase observables between receivers can be expressed as (Hofmann-Wellenhof et al., 2001):

$$\lambda^j \Delta\phi^j = \Delta\rho^j - \lambda^j \Delta N^j + c \cdot \Delta\delta + \Delta I^j /(f^j)^2 + \Delta T^j + \varepsilon_{\Delta\phi^j} \tag{7.1}$$

where the superscript j denotes the satellite; $\Delta\phi^j$ is the SD phase observable in units of cycles; λ^j and f^j are the wavelength and frequency respectively; $\Delta\rho^j$ is the SD geometric distance between the satellite and the receivers; ΔN^j is the SD integer ambiguity; $\Delta\delta$ is the difference between the two receiver clock errors; $\Delta I^j /(f^j)^2$ and ΔT^j are the SD range errors resulted from the ionospheric and tropospheric delays, where I is a function of the Total Electron Content (TEC); and $\varepsilon_{\Delta\phi^j}$ is the measurement noise of $\Delta\phi^j$.

Equation (7.1) is valid for GPS, GLONASS and Galileo carrier phase measurements. However, unlike GPS and Galileo, where each satellite transmits on the same frequency in a Code Division Multiple Access (CDMA) format, each GLONASS satellite transmits on a different frequency in a Frequency Division Multiple Access (FDMA) format. For two satellites j and k, double-difference phase observable can be expressed in units of cycles:

$$\begin{aligned}\nabla\Delta\phi^{jk} = \Delta\phi^k - \Delta\phi^j = (\frac{1}{\lambda^k}\Delta\rho^k - \frac{1}{\lambda^j}\Delta\rho^j) - \nabla\Delta N^{jk} + (f^k - f^j)\Delta\delta \\ + (\frac{1}{c \cdot f^k}\Delta I^k - \frac{1}{c \cdot f^j}\Delta I^j) + (\frac{1}{\lambda^k}\Delta T^k - \frac{1}{\lambda^j}\Delta T^j) + \varepsilon_{\nabla\Delta\phi^{jk}}\end{aligned} \tag{7.2}$$

where ∇ represents the difference between satellites. It can be seen from Equation (7.2) that processing of GNSS multiple-frequency data becomes more complicated for integrated GPS/GLONASS and GPS/GLONASS/Galileo due to the different signal frequencies of GLONASS satellites. Over short baselines (e.g. shorter than 1 km), the differenced ionospheric and tropospheric delays shown in Equation (7.2) can be cancelled to a significant extent. However, the difference between the receiver clock biases cannot be eliminated from Equation (7.2). To compensate the time offset caused by different time references, a receiver clock bias/offset is estimated for each system in the adjustment. Therefore, the vector of unknown parameters for a combined GPS/GLONASS/Galileo positioning solution is:

$$x = [dX, dY, dZ, \delta_{\mathrm{GPS}}, \delta_{\mathrm{GLONASS}}, \delta_{\mathrm{Galileo}}]^T \tag{7.3}$$

where dX, dY and dZ are the coordinates; and δ_{GPS}, $\delta_{\mathrm{GLONASS}}$ and $\delta_{\mathrm{Galileo}}$ are the receiver clock offsets for GPS, GLONASS and Galileo respectively.

For simulation efficiency, reference time and coordinate reference frames of the simulated GLONASS and Galileo ephemerides are referred to GPS time and WGS-84 (GPS coordinate reference frame, tied to the International Terrestrial Reference Frame (ITRF)) respectively. Although GLONASS provides position and time in the Russian reference systems, the modernization of GLONASS will improve the GLONASS Terrestrial Reference Frame (PZ90.02) to make it agree with the ITRF and will transmit corrections between GPS and GLONASS time to facilitate joint uses. In addition, the Galileo Terrestrial Reference Frame (GTRF) will be tied to the ITRF. The differences between WGS-84 and GTRF are expected to become insignificant, implying that WGS-84 and GTRF will be identical within the accuracy of both realizations (Hein et al., 2003). In the future, precise estimation of the

Galileo/GPS time offset will be provided in each system's navigation message for interoperability. Therefore, alignment of one GNSS reference time to another can be easily achieved using the parameters of time offset in navigation messages. It is considered that the simulated GLONASS and Galileo data referred to the GPS time and WGS-84 have no significant impact on the simulation performance.

7.4 Simulation of GNSS Data

Since the modernized GPS signals and Galileo signals cannot be made available now and the full GLONASS constellation is still being developed, the multiple-frequency data used in this chapter were simulated using a GNSS simulator (Satellite Navigation Toolbox 3.0, developed by GPSoft®). Pseudorange and carrier phase 'measurements' can be generated as true geometric ranges corrupted by many error sources, such as ionospheric and tropospheric refraction and delay, multipath error and measurement noise. Parameters related to simulating the GNSS orbit and various errors are described below.

7.4.1 Orbit Simulation

Keplerian orbital parameters for ideal circular orbits are used to simulate the constellations of 30-satellite GPS, 24-satellite GLONASS and 30-satellite GALILEO. The parameters used include orbit radius (a), longitudes of ascending node (Ω), inclination angle of orbital plane (i), mean anomalies at reference time (M_0), reference time for orbital parameters (t_{oe}). The small perturbations associated with the actual satellites are ignored for simulation simplicity. Since the simulated satellite orbit is assumed to be perfectly circular, only the orbit radius, a, can determine the orbital dimension. The relative orientation of the orbital plane with respect to Earth can then be determined by the two parameters Ω and i. Finally, M_0 as the function of time can be used to describe the instantaneous position of the satellite within its orbit.

For GPS constellation simulation, there are six evenly spaced orbital planes with ascending nodes approximately 60° apart. Five satellites are spaced on each plane with an inclination of 55° and an orbit radius of about 26,561 km. The GLONASS constellation has three orbital planes whose ascending nodes are 120° apart. Eight satellites are equally spaced per plane with an argument of latitude displacement of 45°. The satellites operate in circular orbits at an inclination of 64.8°, with an orbit radius of about 25,490 km used in the simulation. For simulated Galileo, there are three orbital planes with a 56° nominal inclination and an orbit radius of about 29,601 km. Each orbital plane contains nine satellites nominally 40° apart and one acts as a spare.

7.4.2 Ionospheric Delay

The ionospheric delay is modelled using the traditional raised half-cosine profile for path delay along the vertical direction with the satellite at an elevation angle of 90° (i.e. zenith). For other elevation angles, the zenith delay is scaled by the FAA (Federal Aviation Administration) Wide Area Augmentation System obliquity factor to account for the increased path length that the signal will travel within the ionosphere. The model used for zenith delay is also called the Klobuchar model. This model assumes the zenith ionospheric delay can be approximated by half a cosine function of the local time during daytime and by a constant level during nighttime (Klobuchar, 1996). Descriptions of the obliquity factor utilized in our simulation can be found in Kaplan and Hegarty (2006). Figure 7.4 shows the resulting ionospheric delay over a period of one day, where each curve represents a satellite pass. It is seen from Fig. 7.4 that the ionospheric delay is highly variable throughout the day.

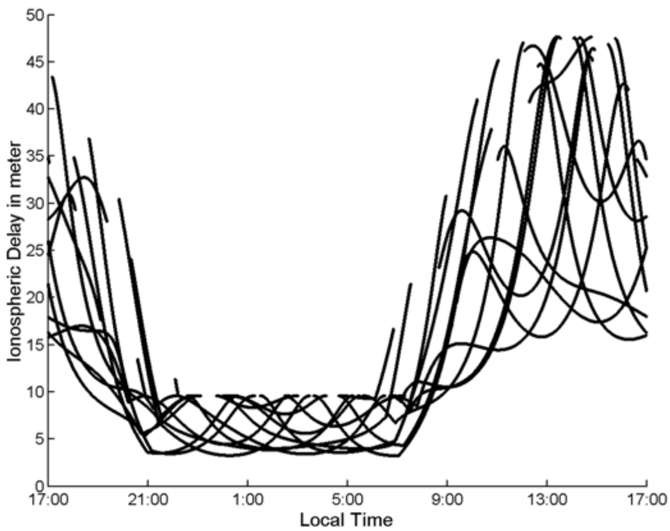

Fig. 7.4 Variations of simulated ionospheric error for a 24-hour period (each curve represents a satellite pass).

7.4.3 Tropospheric Delay

The modified Hopfield model is employed to simulate the tropospheric delay, which results in a ranging error of about 3 m for a satellite at the zenith to about 25 m for a satellite at an elevation angle of approximately 5°. This delay is a function of the tropospheric refraction index, which is dependent on the local temperature, pressure and relative humility (Hoffman-Wellenhof et al., 2001). For the experiments carried out in this chapter, typical values of 288.15 Kelvin, 1013 millibar and 50% are assumed for the temperature, pressure and relative humility respectively. The relationship between the resulting tropospheric delay and the satellite elevation angle is depicted in Fig. 7.5.

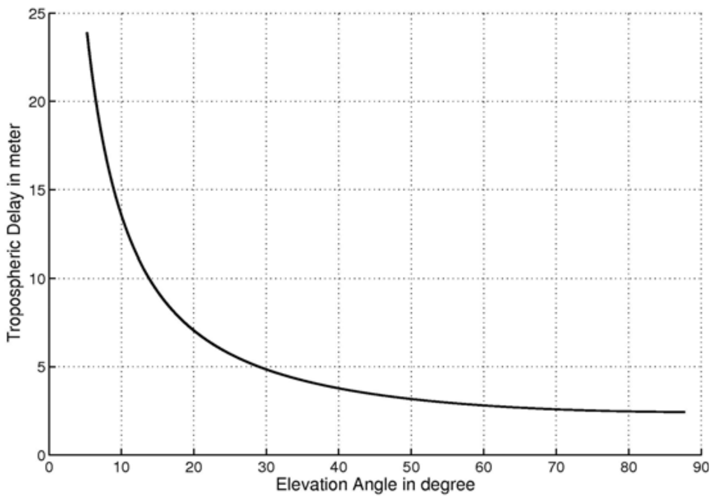

Fig. 7.5 Variations of simulated tropospheric delay as a function of satellite elevation angles.

7.4.4 Multipath Error

The zero-elevation angle multipath error is modelled by a coloured or time-correlated noise, which is then scaled by the satellite elevation angle in order to account for the greater multipath effects for satellites with low elevation angles (Larson et al., 2007). A first-order recursive digital filter having a Butterworth response, expressed by Equation (7.4), is used to generate the code multipath error of zero elevation angle.

$$y(n) = a_0 x(n) + a_1 x(n-1) - b_1 y(n-1) \tag{7.4}$$

where $y(n)$ is an output response; a_0, a_1 and b_1 are Butterworth lowpass filter coefficients; and $x(n)$ is an input white noise series. The carrier-phase multipath error is generated by multiplying the code multipath error by a factor of $(0.05*\lambda)$, where λ is the carrier wavelength in meters. Uncorrelated multipath errors are simulated for each carrier frequency and each observation site to ensure that the multipath errors will not be eliminated when forming the double-difference observations. Figure 7.6 shows the GPS L1 carrier-phase multipath effects for a high and a low elevation satellite, where a lowpass Butterworth filter with a cutoff frequency of 0.025 Hz was used and its standard deviation of white noise was set to 5 m. It can be seen from Fig. 7.6 that the simulated multipath effects are smaller for the high elevation satellite; while are greater for the low elevation angles.

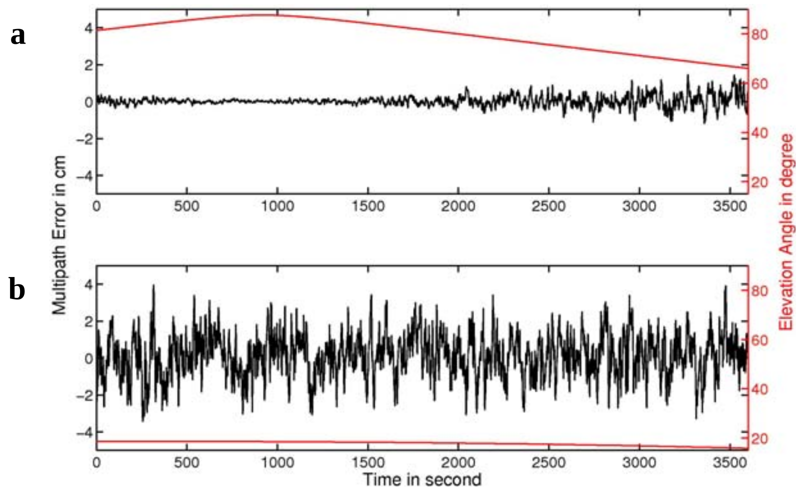

Fig. 7.6 a Multipath effects on L1 phase (*bottom curve*) and satellite elevation angle (*top curve*); **b** multipath effects on L1 phase (*top curve*) and satellite elevation angle (*bottom curve*). The satellite elevation angle is indicated by the right hand vertical axis.

7.4.5 Measurement Noise

The measurement noise is modelled by a random white noise with normal distribution. In this simulation, the standard deviation is 1 meter for pseudorange and ($0.05*\lambda$) meters for carrier phase (where λ is the carrier wavelength in meters).

7.5 Results and Analysis for Multipath Mitigation

7.5.1 Global Satellite Visibility

Simulations have been carried out as though the complete GPS, GLONASS and Galileo systems were in operation. A global snapshot of satellite visibilities for the standalone GPS, integrated GPS/GLONASS, GPS/GALILEO and GPS/GLONASS/GALILEO constellations is presented in Fig. 7.7. The simulation was performed for 0000 h at 1° intervals of latitude and longitude and an altitude of 50 m, using a 15° masking angle.

The average satellite visibilities are approximately 8, 14, 16 and 23 for GPS, GPS/GLONASS, GPS/Galileo and GPS/GLONASS/Galileo scenarios respectively. The visibility improvements of the combined systems with respect to GPS-only are therefore about 175%, 200% and 290% for GPS/GLONASS, GPS/Galileo and GPS/GLONASS/Galileo respectively. The GPS/Galileo system is slightly better than the combined GPS/GLONASS due to the simulated Galileo constellation having six more satellites than GLONASS.

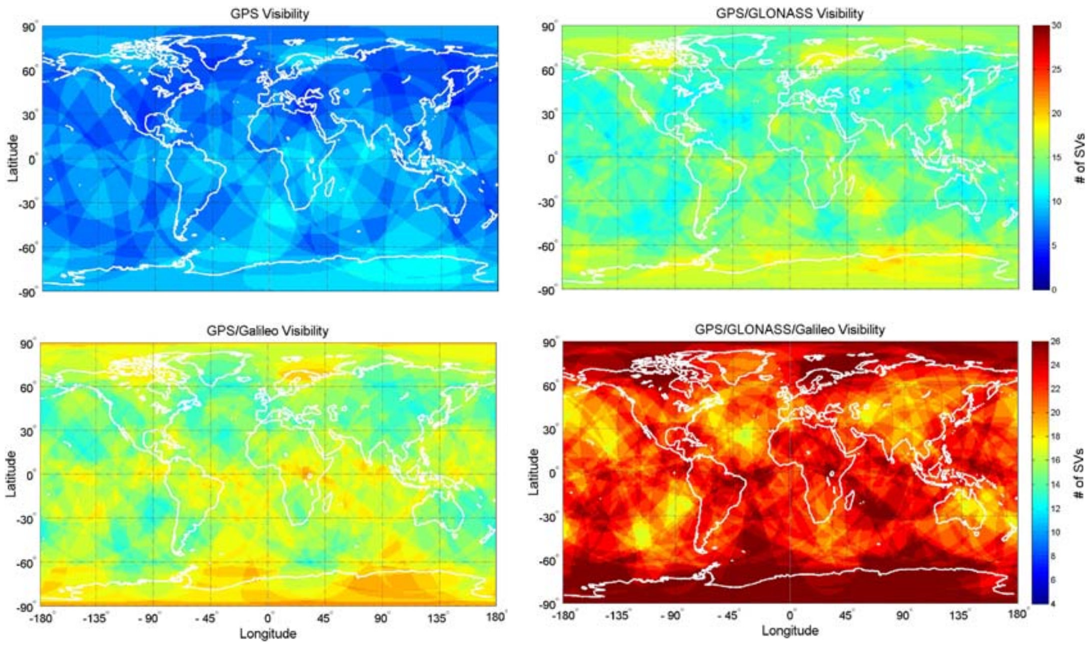

Fig. 7.7 Global satellite visibility for GPS, GPS/GLONASS, GPS/Galileo and GPS/GLONASS/Galileo, with a 15° masking angle.

7.5.2 Description of Experimental Data

Simulations have been performed over a period of one hour at a sampling rate of 1 Hz, with a baseline length of about 84 m. The sky plot of all available satellites is shown in Fig. 7.8, where a unique range of satellite identification number (or SV ID for short) is assigned to each constellation (i.e., GPS: 1-30; GLONASS: 51-74; Galileo: 201-230). Moreover, the information of satellites contaminated by multipath effects is given in Table 7.3. The simulated GPS, GLONASS and Galileo multipath errors for their respective multipathing satellites at the reference station are shown in Figs. 7.9 to 7.16.

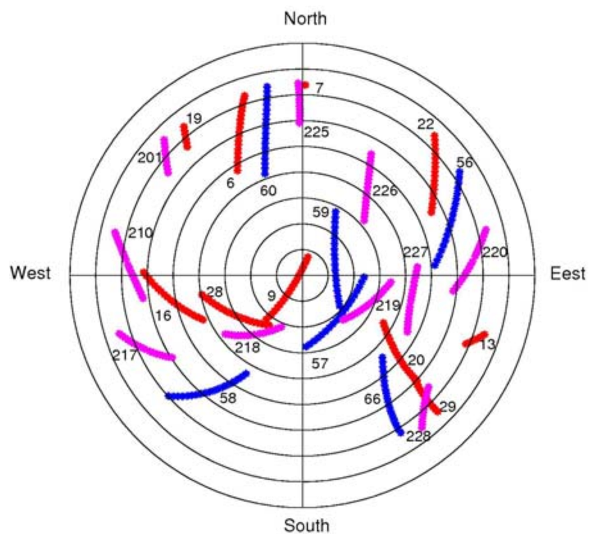

Fig. 7.8 A sky plot of GPS (SV ID: 1-30), GLONASS (SV ID: 51-74) and Galileo (SV ID: 201-230) satellites for a period of one hour.

Table 7.3 Information of satellites contaminated by multipath effects.

Available satellites Nos	Satellites Nos with multipath effects	SV ID of satellites with multipath effects		
		GPS	GLONASS	Galileo
21-24	8	6, 16, 28	58, 60	210, 217, 218

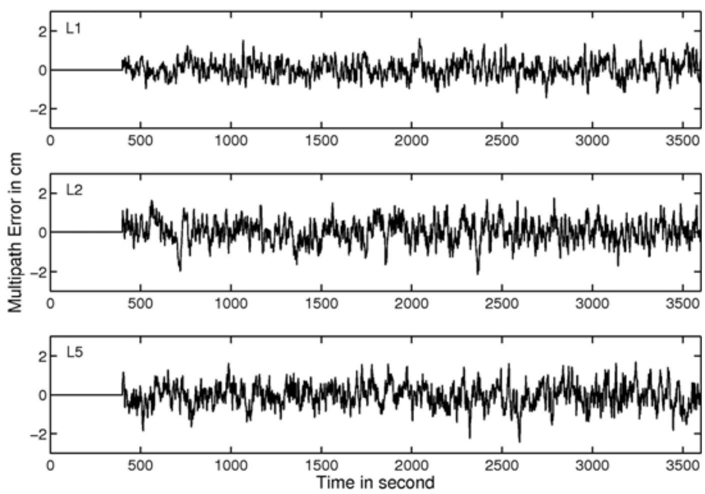

Fig. 7.9 Simulated GPS carrier-phase multipath errors on L1 (*top panel*), L2 (*middle*

panel) and L5 (*bottom panel*) for SV 06 at the reference station.

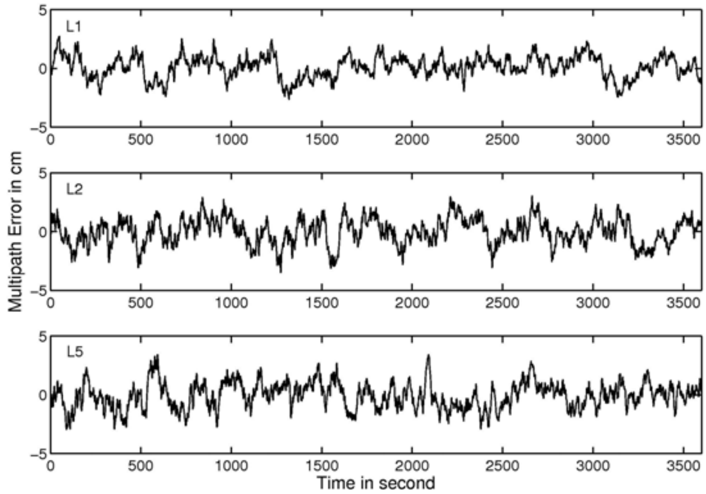

Fig. 7.10 Simulated GPS carrier-phase multipath errors on L1 (*top panel*), L2 (*middle panel*) and L5 (*bottom panel*) for SV 16 at the reference station.

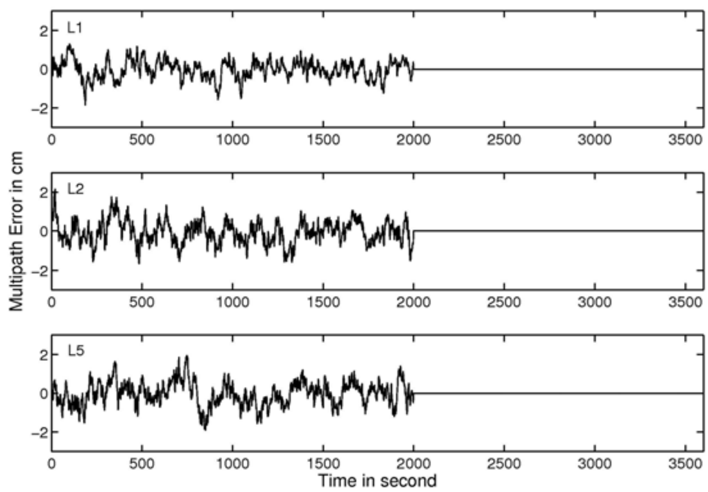

Fig. 7.11 Simulated GPS carrier-phase multipath errors on L1 (*top panel*), L2 (*middle panel*) and L5 (*bottom panel*) for SV 28 at the reference station.

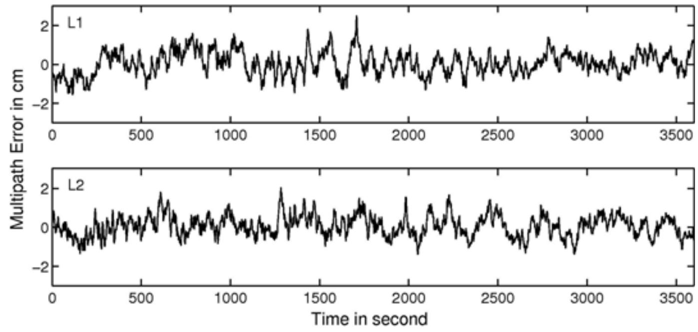

Fig. 7.12 Simulated GLONASS carrier-phase multipath errors on L1 (*top panel*) and L2 (*bottom panel*) for SV 58 at the reference station.

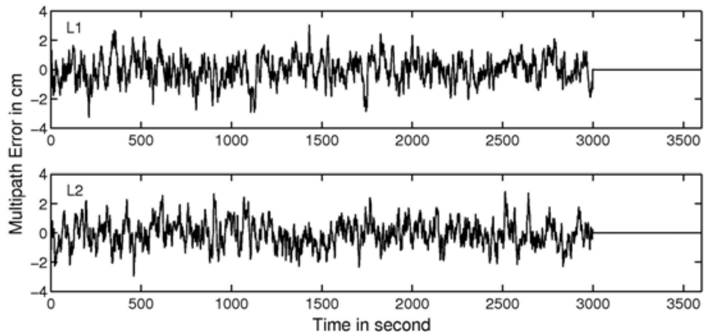

Fig. 7.13 Simulated GLONASS carrier-phase multipath errors on L1 (*top panel*) and L2 (*bottom panel*) for SV 60 at the reference station.

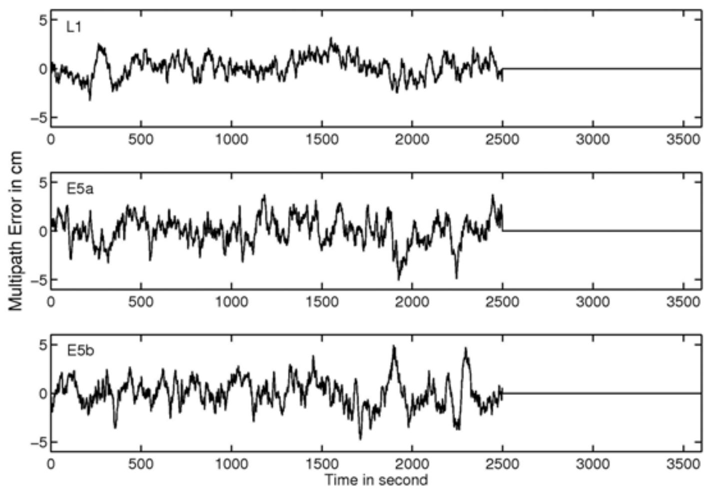

Fig. 7.14 Simulated Galileo carrier-phase multipath errors on L1 (*top panel*), E5a (*middle panel*) and E5b (*bottom panel*) for SV 210 at the reference station.

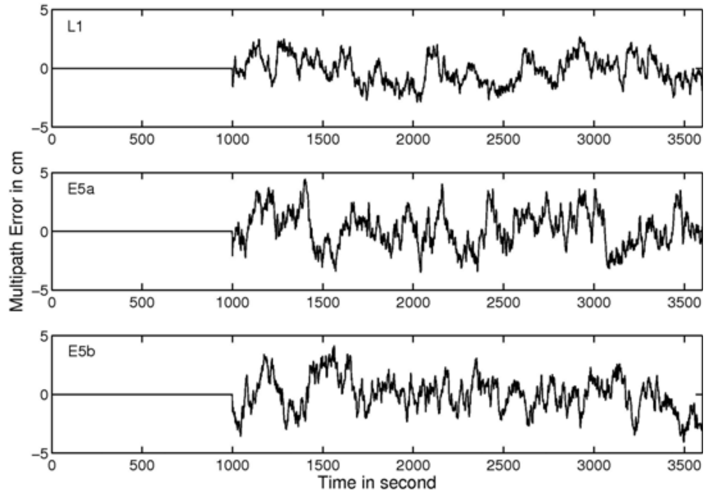

Fig. 7.15 Simulated Galileo carrier-phase multipath errors on L1 (*top panel*), E5a (*middle panel*) and E5b (*bottom panel*) for SV 217 at the reference station.

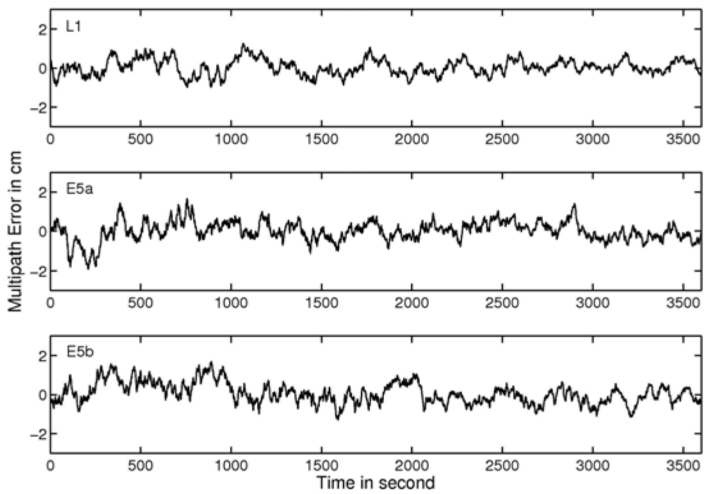

Fig. 7.16 Simulated Galileo carrier-phase multipath errors on L1 (*top panel*), E5a (*middle panel*) and E5b (*bottom panel*) for SV 218 at the reference station.

7.5.3 Results of GNSS Data Processing

To acquire a deeper insight into the potential of future GNSS signals to mitigate multipath in different propagation environments, typical mask elevation angles of 15° and 30° were used to simulate the effects of suburban and urban canyons respectively. The following 1-h simulation results show the positioning errors and accuracy improvements under different scenarios.

Positioning Errors Using an Elevation Angle of 15°

Figures 7.17 to 7.21 show the positioning errors from least squares single-epoch solutions in the East, North and up directions respectively, for scenarios 1 to 5 (see Table 7.2 for scenario descriptions), when a 15° elevation angle is used.

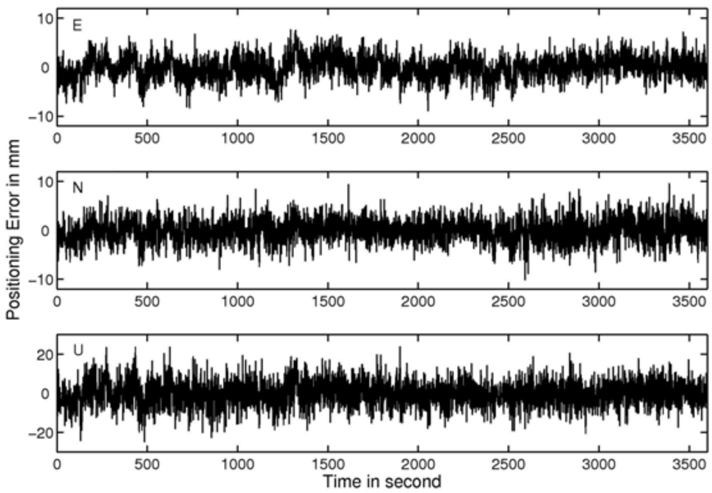

Fig. 7.17 Positioning errors in the East (*top panel*), North (*middle panel*) and up (*bottom panel*) directions of single-epoch solution using L1 GPS signal, when a 15° elevation angle is used.

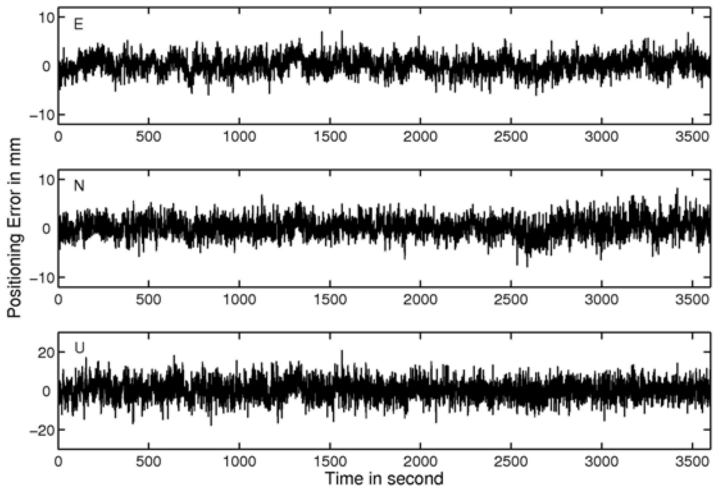

Fig. 7.18 Positioning errors in the East (*top panel*), North (*middle panel*) and up (*bottom panel*) directions of single-epoch solution using L1, L2 and L5 GPS signals, when a 15° elevation angle is used.

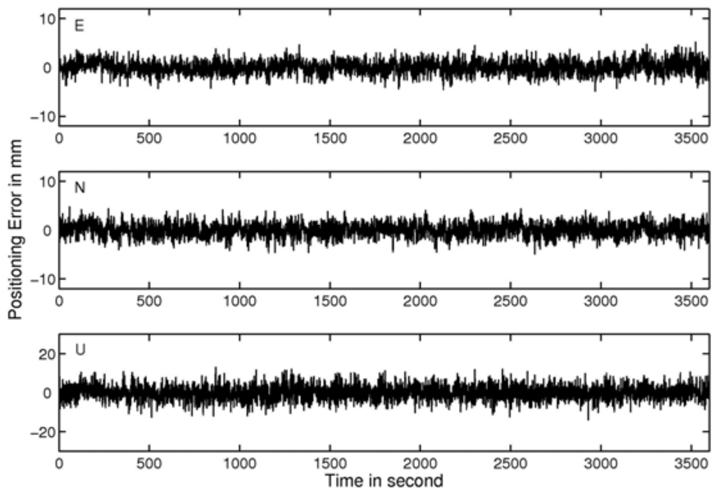

Fig. 7.19 Positioning error in the East (*top panel*), North (*middle panel*) and up (*bottom panel*) directions of single-epoch solution using GPS three-frequency and GLONASS dual-frequency data, when a 15° elevation angle is used.

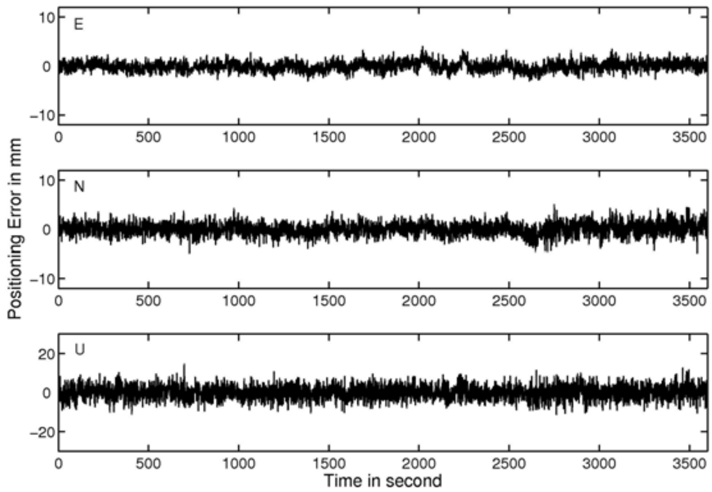

Fig. 7.20 Positioning errors in the East (*top panel*), North (*middle panel*) and up (*bottom panel*) directions of single-epoch solution using GPS and Galileo three-frequency data, when a 15° elevation angle is used.

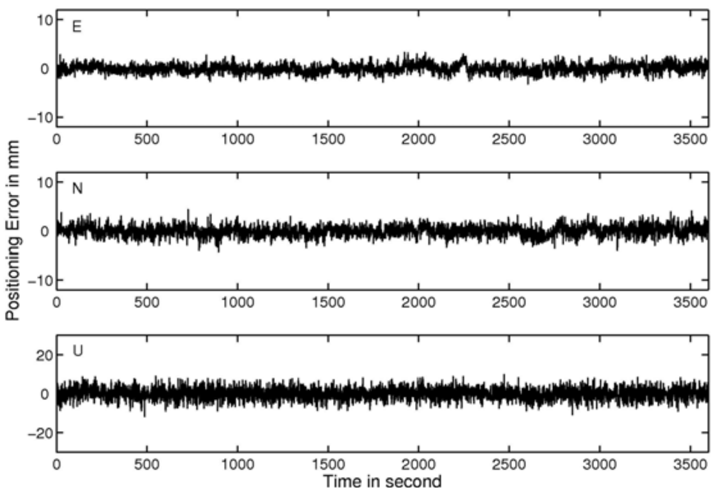

Fig. 7.21 Positioning errors in the East (*top panel*), North (*middle panel*) and up (*bottom panel*) directions of single-epoch solution using GPS three-frequency, GLONASS dual-frequency and Galileo three-frequency data, when a 15° elevation angle is used.

Positioning Errors Using an Elevation Angle of 30°

Positioning errors from single-epoch solutions in the East, North and up directions for scenarios 1 to 5 (see Table 7.2 for scenario descriptions) are shown in Figs. 7.22 to 7.26 respectively, when an elevation angle of 30° is used.

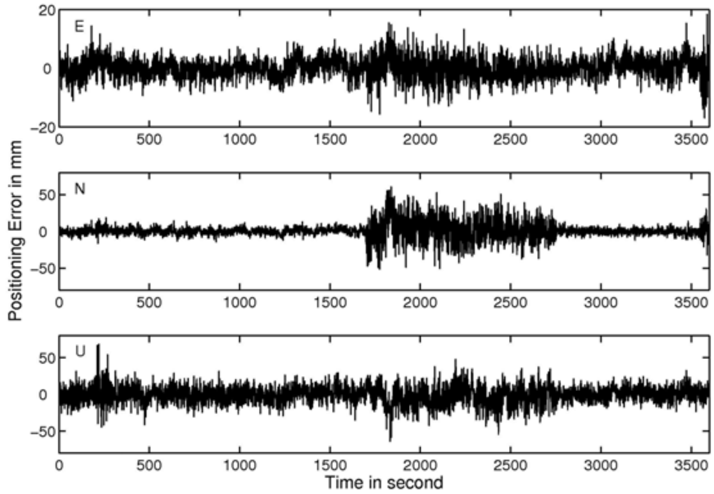

Fig. 7.22 Positioning errors in the East (*top panel*), North (*middle panel*) and up (*bottom panel*) directions of single-epoch solution using L1 GPS signal, when a 30° elevation angle is used.

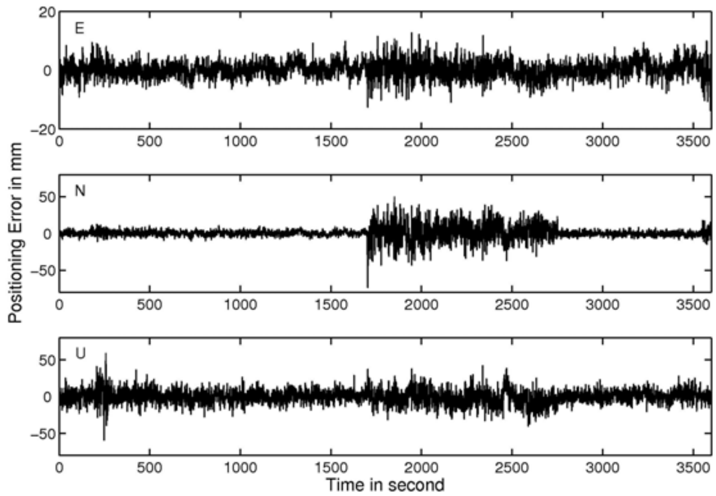

Fig. 7.23 Positioning errors in the East (*top panel*), North (*middle panel*) and up

(*bottom panel*) directions of single-epoch solution using L1, L2 and L5 GPS signals, when a 30° elevation angle is used.

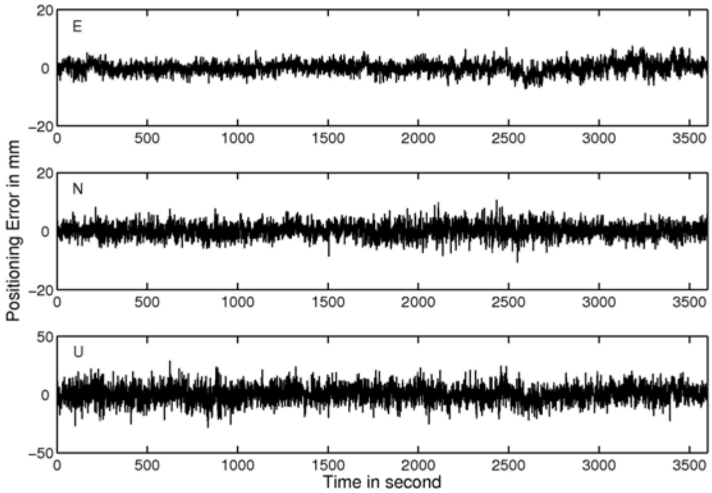

Fig. 7.24 Positioning errors in the East (*top panel*), North (*middle panel*) and up (*bottom panel*) directions of single-epoch solution using GPS three-frequency and GLONASS dual-frequency data, when a 30° elevation angle is used.

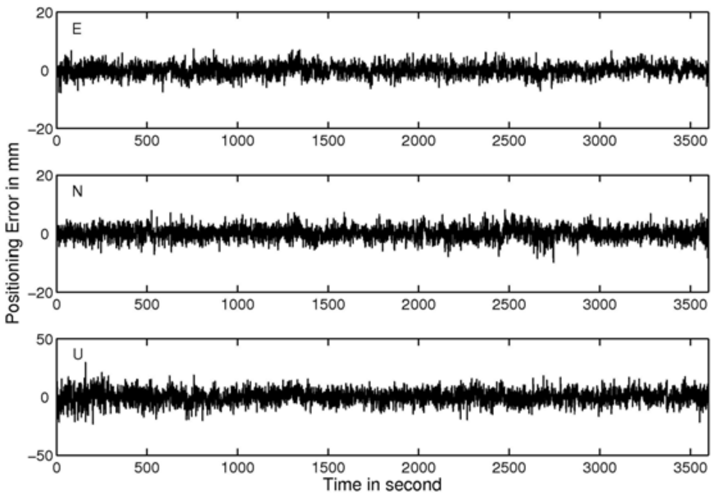

Fig. 7.25 Positioning errors in the East (*top panel*), North (*middle panel*) and up (*bottom panel*) directions of single-epoch solution using GPS and Galileo three-frequency data, when a 30° elevation angle is used.

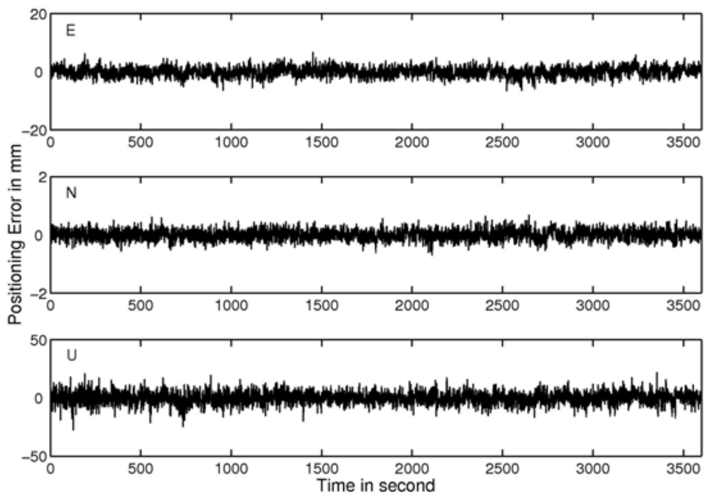

Fig. 7.26 Positioning errors in the East (*top panel*), North (*middle panel*) and up (*bottom panel*) directions of single-epoch solution using GPS three-frequency, GLONASS dual-frequency and Galileo three-frequency data, when a 30° elevation angle is used.

7.5.4 Comparison and Analysis

RMS values of the positioning errors in the East, North, up directions and 3-Dimensional (3D) position for elevation angles of 15° and 30° are shown in Tables 7.4 and 7.5 respectively, for each scenario. In addition, improvements in 3D position accuracy with the multiple-frequency GNSS data over the current GPS single-frequency data are also shown in Tables 7.4 and 7.5 in order to evaluate the effectiveness of future GNSS signals in multipath mitigation.

Table 7.4 RMS positioning errors in the East, North, up directions and 3D position in millimeters and 3D position accuracy improvements as percentages for a 15° elevation angle.

Scenario	E	N	U	3D	Improvement (%)
SF GPS	2.420	2.508	6.733	3.893	-
TF GPS	1.878	2.029	5.328	3.027	22
GPS/GLONASS	1.387	1.428	3.776	2.110	46
GPS/Galileo	0.996	1.309	3.636	1.991	49
GPS/GLONASS/Galileo	0.928	1.124	3.123	1.713	56

Table 7.5 RMS positioning errors in the East, North, up directions and 3D position in millimeters and 3D position accuracy improvements as percentages for a 30° elevation angle.

Scenario	E	N	U	3D	Improvement (%)
SF GPS	3.771	10.489	12.409	10.121	-
TF GPS	3.021	8.393	10.037	8.176	19
GPS/GLONASS	2.044	2.524	7.552	4.342	57
GPS/Galileo	2.091	2.275	5.946	3.333	67
GPS/GLONASS/Galileo	1.716	1.864	5.448	3.053	70

It can be seen from Tables 7.4 and 7.5 that an increasing improvement in 3D position accuracy can be obtained from the TF GPS, GPS/GLONASS, GPS/Galileo and GPS/GLONASS/Galileo scenarios compared to the SF GPS scenario. The use of GPS three-frequency data shows about 20% improvement on accuracy when compared with the GPS single-frequency data. When integrating GPS with GLONASS or Galileo system, the positioning errors can be significantly reduced by about 55% with respect to the SF GPS scenario. From the current GPS single frequency to the future GPS/GLONASS/Galileo maximum number of frequencies, the positioning accuracy can be improved by about 63% in average. This coincides well with the fact that more redundant measurements give better averaging within the adjustment, indicating that the multiple-frequency data from future GNSS systems have greater potential to mitigate multipath effects than data from the current GPS system.

It can also be seen from Tables 7.4 and 7.5 that the combined GPS/GLONASS, GPS/Galileo and GPS/GLONASS/Galileo constellations exhibit better performances in accuracy improvements for a 30° elevation angle than those for a 15° elevation angle. It is considered that this is due to the poorer positioning results of standalone GPS when a 30° satellite elevation angle is used. The analysis for this is further depicted in Fig. 7.27, where an offset of 7 cm is added to the third subplot to separate the coordinate series for clarity.

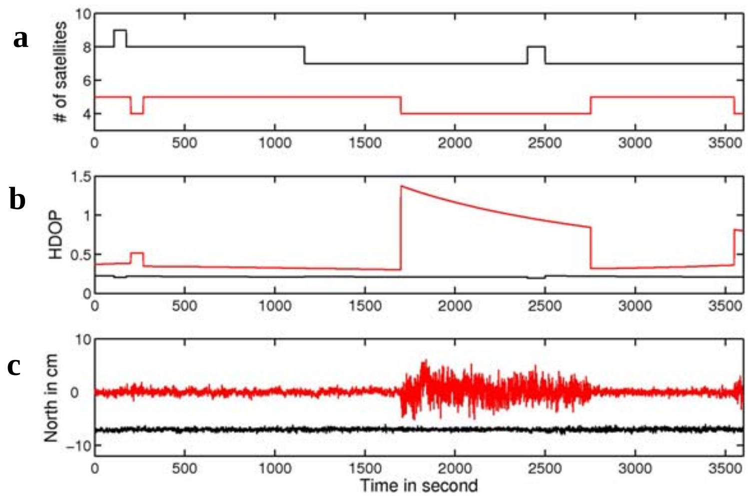

Fig. 7.27 a Number of satellites for 15° (*top line*) and 30°(*bottom line*) elevation angles; **b** HDOP values for 15° (*bottom line*) and 30°(*top line*) elevation angles; and **c** North coordinate components using L1 GPS signals for 15° (*bottom curve*) and 30° (*top curve*) elevation angles, where an offset of 7 cm was added.

It can be seen from Fig. 7.27 that fewer visible satellites results in poorer satellite geometry indicated by the higher HDOP values, corresponding to greater positioning errors. The results of Tables 7.4 and 7.5 and Fig. 7.27 indicate that mitigation of multipath effects using modernized GNSS signals may be more applicable to areas where satellite signals are obstructed, such as in urban canyons, under tree canopies or in open-cut mines.

7.6 Conclusions and Discussions

The impact of modernized GNSS data on single-epoch positioning accuracy in the presence of multipath effects has been investigated in this chapter. Simulation studies have shown that consistent improvements in positioning accuracy can be achieved when more satellites and signals are available. The use of the future GPS/GLONASS/Galileo multiple-frequency data can improve the accuracy by about 63% on average when compared to the current GPS single-frequency data. The GPS/GLONASS and GPS/Galileo combination scenarios exhibit similar results; both reduce the RMS values of the positioning errors by about 55% with respect to the GPS single-frequency scenario. Results have also shown that multipath mitigation using modernized GNSS signals may be more applicable in areas where satellite signals are obstructed.

[blank page]

Chapter 8

Conclusions and Recommendations

8.1 Conclusions

GPS signal multipath effects on the carrier phase measurements can be up to about 1/4 of the GPS signal wavelength. As a result, the effects of multipath have been a limiting error source in many precise GPS positioning and navigation applications where the accuracy requirements are often at the millimeter level. Despite great research efforts devoted to multipath mitigation, the existing methods for mitigating the GPS multipath effects are not always as effective as desired. This thesis focuses mainly on further understanding the characteristics of GPS multipath effects, developing methods for better mitigating the effects of multipath, and investigating real-time applications of some of the multipath mitigation methods.

GPS has been widely used in precise GPS applications such as structural vibration monitoring over the last two decades. In such applications, filters are frequently used to retrieve vibration signals from the multipath effects. A Vondrak bandpass filter has been proposed in this thesis to smooth out the multipath effects and extract the vibration signals. The proposed filter is compared with two commonly used filters for such applications, i.e., the wavelet and adaptive FIR filters. Results from the study have revealed that the GPS accuracy of tracking structural dynamics and complex signals with varying frequencies can be improved with all the filters tested. The results of the experiments described in this thesis show that the performance of the Vondrak filter is similar to that of the wavelet filter in terms of the minimum detectable vibrations and the accuracy improvements. Both filters are superior to the adaptive FIR filter. The implementation of the Vondrak and wavelet filters is computationally efficient; however time-frequency analysis or a prior knowledge of structure design is required.

The Vondrak filter has a good signal resolution at the signal truncation frequency band and the wavelet filter has good localized time-frequency features. The new filtering methods, i.e., cross-validation Vondrak filter (CVVF) and cross-validation wavelet filter (CVWF), based on the Vondrak or wavelet filter and the method of cross-validation, have been developed for separating noise from the signals in a data series with no time-frequency analysis or prior information. The CVVF method uses the cross-validation method to determine the optimal smoothing factor of the Vondrak numerical filter; whereas the CVWF method utilizes the method of cross-validation to automatically identify signal levels after wavelet decomposition.

In order to take advantage of GPS multipath day-to-day repeating property, an accurate multipath signal model is essential to reduce the effects of multipath. The proposed filtering methods have been applied to establish reliable GPS multipath signal models for point coordinate series and then make corrections to the subsequent GPS coordinates. Test results have shown that the proposed CVVF and CVWF methods are both effective signal decomposers. Both methods work well for data series with different noise levels and the former is superior to the latter. The CVVF method can be used to separate noise and signal in a data series when the noise level is lower than the magnitude of the signal. When the noise level is higher than the magnitude, high-frequency signals tend to be filtered out together with the noise. With regard to the CVWF method, the signal can be separated from noise when the noise level is lower than half of the magnitude of the signal. Test results have also shown that a 20–40% improvement in GPS accuracy can be obtained by using the two methods.

For precise positioning applications such as deformation monitoring, low cutoff elevation angle of GPS satellites (e.g. 10–15°) can be used to minimize the multipath disturbance and signal blockage. In this situation, the errors caused by the diffracted GPS signals may become significant. To investigate the variation in the multipath day-to-day repeatability and to maximize the GPS accuracy improvements, this thesis has proposed the use of the stochastic SIGMA-Δ model to reduce the diffraction errors. This is followed by application of the proposed CVVF to establish a multipath signal model and use of the ARTA method to reduce the multipath effects. Test examples have shown that using the SIGMA-Δ model can reduce significantly the signal diffraction effects and at the same time retain the main multipath signals. The correlation of the multipath signals decreases with the increase of the time span between the current day and the day when the multipath model was established. The shorter the period of multipath signal, the weaker the correlation. Test examples have also shown that the stochastic SIGMA-Δ model is more applicable to improve the accuracy of observations over a short time period (e.g. less than several days); whereas the ARTA method is more applicable to observations over a long time period (e.g. tens of days). Compared with the standard data stacking method, the proposed integrated use of the CVVF, SIGMA-Δ and ARTA methods can improve further GPS accuracy by about 29%, 16% and 24% for the East, North and up directions respectively.

Since the orbital repeat period varies for each satellite, and different satellites may contribute to position estimates, it is preferable if the multipath in the carrier phase observations can be removed on a satellite-by-satellite basis. A new filtering method, based on satellite-specific single differences, has been developed for mitigating the effects of GPS signal multipath and diffraction. First, GPS double-difference carrier-phase residuals are converted into single-difference residuals on each day. The single-difference residuals thus obtained are used as a multipath signal model and the model is then subtracted from single-difference residuals of the subsequent days. The final coordinates are resolved by using the double-difference residuals formed based on the corrected single-difference residuals. Test results have demonstrated that the new filtering method can reduce the effects of GPS signal multipath and diffraction more effectively, and a further 20–60% improvement in accuracy can be achieved when compared with the stacking method. The proposed method is also advantageous in that it can be implemented in real-time.

Lack of available GPS signals is a major limitation in highly masked environments; however, the interoperability of GNSS can be expected to provide more satellites and the positioning accuracy can thus be improved. Multipath mitigation through averaging based on the least squares process using multiple-frequency GNSS data has been investigated. Since the modernized GPS, GLONASS and Galileo signals are not yet available, all data has been generated by a GNSS data simulator. Simulation results have shown that the modernized GPS and integrated GPS/GLONASS, GPS/Galileo and GPS/GLONASS/Galileo multiple-frequency systems have much better multipath mitigation capability than the current single-frequency GPS. The GPS/GLONASS and GPS/Galileo scenarios exhibit similar results; both reduce the RMS values of GPS positioning errors by about 55% with respect to the GPS single-frequency scenario. The use of the future GPS/GLONASS/Galileo multiple-frequency data can improve the accuracy by about 63% on average when compared to the GPS single-frequency data. It has also been shown that multipath mitigation using modernized GNSS signals are more applicable to areas where satellite signals are obstructed.

8.2 Recommendations

The approaches developed in this thesis reveal promising results, but some of these need to be further investigated. First, GPS observations over a longer time period (e.g. several months, even up to one year or more) can be expected to provide a better understanding of the variations in the multipath day-to-day repeating characteristics. Second, besides the GPS, GLONASS and Galileo systems as demonstrated in this thesis, other future space-based navigation systems, such as China's Beidou system, Japan's Quasi Zenith Satellite System (QZSS) and India's Regional Navigational Satellite System (IRNSS), can be used to increase further the redundancy that offers a better possibility to mitigate the multipath effects. Future study on detecting and rejecting the measurements contaminated by multipath effects may be carried out. Finally, the approaches proposed here are only applied to short baselines due to the fact that differential GPS techniques can largely eliminate the common-mode errors between reference and rover GPS stations. Further investigation into these methods for long baselines (e.g. tens to hundreds of kilometers) is needed.

References

Agnew DC, Larson KM (2007) Finding the repeat times of the GPS constellation. GPS Solutions 11(1): 71-76.

Akay M (1994) Biomedical signal processing. Academic Press, New York.

Alber C, Ware R, Rocken C, Braun J (2000) Obtaining single path phase delays from GPS double differences. Geophysical Research Letters 27: 2661-2664.

Alexander K (2006) U.S. space based PNT policy and GPS modernization. United Nations/Zambia/ESA Regional Workshop on the Applications of Global Navigation Satellite System Technologies in Sub-Saharan Africa, Lusaka, Zambia, 26-30 June.

Averin SV (2006) GLONASS system: present day and prospective status and performance. European Navigation Conference GNSS-2006, Manchester, UK, May, 7-10.

Axelrad P, Comp CJ, Macdoran PF (1996) SNR-based multipath error correction for GPS differential phase. Aerospace and Electronic Systems, IEEE Transactions on 32(2): 650-660.

Axelrad P, Larson K, Jones B (2005) Use of the correct satellite repeat period to characterize and reduce site-specific multipath errors. Proceedings of the ION GNSS 2005, Long Beach, CA, 13-16 September, pp 2638-2648.

Bauersima I (1983) NAVSTAR/Global Positioning Sytems (GPS) II. Mitteilungen der Satellitenbeobachtungsstation Zimmerwald, Nr.10, Astronomical Institute, University of Berne, Switzerland.

Bétaille D, Maenpa J, Euler HJ, Cross PA (2003) A new approach to GPS phase multipath mitigation. Proceedings of the ION NTM 2003, Anaheim, CA, 22-24 January, pp 243-253.

Bilich A, Larson KM, Axelrad P (2008) Modeling GPS phase multipath with SNR: case study from Salar de Uyuni, Bolivia. Journal of Geophysical Research 113: B04401.

Bock Y (1991) Continuous monitoring of crustal deformation. GPS World June 1991: 40-47.

Bock Y, Nikolaidis R, de Jonge PJ, Bevis M (2000) Instantaneous geodetic positioning at medium distances with the Global Positioning System. Journal of Geophysical Research 105: 28,223-28,254.

Braasch MS (1996) Multipath effects, in Parkinson BW, Spilker JJ, Axelrad P, Enge P (eds.), Global Positioning System: Theory and Applications (Volume I). American Institute of Aeronautics and Astronautics, Washington, DC, pp 547-568.

Braasch MS, van Dierendonck AJ (1999) GPS receiver architectures and measurements. Proceedings of the IEEE 87(1): 48-64.

Breiman L, Friedman JH, Olshen RA, Stone CJ (1984) Classification and regression trees. Wadsworth International Group, Belmont, California.

Brown J, Karuna R, Ashkenazi V, Roberts GW, Evans R (1999) Monitoring of structures using the Global Positioning System. Proceedings of the Institution of Civil Engineers, Structures and Buildings 134: 97-105.

Brunner FK, Gu M (1991) An improved model for the dual frequency ionospheric correction of GPS observations. Manuscripta Geodaetica 16: 205-214.

Brunner FK, Hartinger H, Troyer L (1999) GPS signal diffraction modelling: the stochastic SIGMA-Δ model. Journal of Geodesy 73: 259-267.

Chan WS, Xu YL, Ding XL, Dai WJ (2005) Calibration of GPS for dynamic displacement measurement of long span cable-supported bridges in vertical direction. Proceedings of the SPIE 5770: 168-179.

Choi K, Bilich A, Larson KM, Axelrad P (2004) Modified sidereal filtering: implications for high-rate GPS positioning. Geophysical Research Letters 31(22): L22608.

Clark MR, Thompson R (1978) An objective method for smoothing paleomagnetic data. Geophysical Journal of the Royal Astronomical Society 52(2): 205-213.

Cohen C, Parkinson B (1991) Mitigating multipath error in GPS-based attitude determination. Guidance and Control, Advances in Astronautical Sciences 74: 53-68.

Comp CJ, Axelrad P (1998) Adaptive SNR-based carrier phase multipath mitigation technique. Aerospace and Electronic Systems, IEEE Transactions on 34(1): 264-276.

Daubechies I (1992) Ten lectures on wavelets. SIAM, Philadelphia, PA.

Debnath L (2002) Wavelet transforms & their applications. Birkhauser, Boston.

Ding X, Chen Y, Zhu J, Huang D (1999) Surface deformation detection using GPS multipath signals. Proceedings of the ION GPS 99, Nashville, TN, 14-17 September, pp 53-62.

Donoho DL (1995) De-noising by soft-thresholding. Information Theory, IEEE Transactions on 41(3): 613-627.

Elòsegui P, Davis JL, Jaldehag RTK, Johansson JM, Niell AE, Shapiro II (1995) Geodesy using the global positioning system: the effects of signal scattering on estimates of site position. Journal of Geophysical Research 100(B7): 9921-9934.

Estey LH and Meertens CM (1999) TEQC: The multi-purpose toolkit for GPS/GLONASS data. GPS Solutions 3: 42-49.

European Space Agency (ESA), Galileo Joint Undertaking (GJU) (2006) Galileo open service signal in space interface control document (OS SIS ICD), Draft 0, Retrieved from http://www.galileoju.com.

Feissel M, Lewandowski W (1984) A comparative analysis of Vondrak and Gaussian smoothing techniques. Journal of Geodesy 58: 464-474.

Forward T, Stewart M, Tsakiri M (2003) GPS data stacking for small scale GPS deformation monitoring applications. Proceedings of the 11th FIG International Symposium on Deformation Measurements, Santorini, Greece, 25-28 May, pp 233-240.

Garin L, Rousseau J (1997) Enhanced strobe correlator multipath rejection for code & carrier. Proceedings of the ION GPS 97, Kansas City, 16-19 September, pp 559-568.

Ge L, Chen HY, Han S, Rizos C (2000) Adaptive filtering of continuous GPS results. Journal of Geodesy 74(7-8): 572-580.

Genrich JF, Bock Y (1992) Rapid resolution of crustal motion at short ranges with the global positioning system. Journal of Geophysical Research 97(B3): 3261-3269.

Georgiadou Y, Kleusberg A (1988) On carrier signal multipath effects in relative GPS positioning. Manuscripta Geodaetica 13(3): 172-179.

Guo JJ, Shang RB, Li YL (1995) Study on multipath effects to GPS positioning. Geotechnical Investigation & Surveying (2): 46-49. (in Chinese)

Han S, Rizos C (1997) Multipath effects on GPS in mine environments. Proceedings of the Xth International Congress of the International Society for Mine Surveying, Fremantle, Australia, 2-6 November, pp 447–457.

Hartinger H, Brunner FK (1998) Signal distortion in high precision GPS surveys. Survey Review 34: 531-541.

Haykin S (2002) Adaptive filter theory. Prentice-Hall, New Jersey.

Hein G, Godet J, Issler J, Martin J, Erhard P, Lucas-Rodriguez R, Pratt T (2002) Status of Galileo frequency and signal design. Proceedings of the ION GPS 2002, Portland, Oregon, 24-27 September, pp 266-277.

Hein GW, Godet J, Issler J, Martin J, Erhard P, Lucas-Rodriguez R, Pratt T (2003) Galileo frequency and signal design. GPS World 14(6): 30-37.

Hofmann-Wellenhof B, Lichtenegger H, Collins J (2001) Global Positioning System: theory and practice. Springer-Verlag, New York.

Hsung TC, Lun DPK, Siu WC (1999) Denoising by singularity detection. Signal Processing, IEEE Transactions on 47(11): 3139-3144.

Huang KY, Zhou X (1981) On essentiality of the Whittaker-Vondrak method as a filter, and estimations of standard deviation and correlation for digital filter. Acta Astronomica Sinica 22(2): 120-130. (in Chinese)

ICD-GPS-200C (2003) Interface control document: Navstar GPS space segment/ navigation user interfaces, US DOD, IRN-200C-005R1, 14 Jan 2003.

Ince CD, Sahin M (2000) Real-time deformation monitoring with GPS & Kalman filter. Earth Planets and Space 52(10): 837-840.

Internaltional GPS Service (IGS) (2005) IGS product table. Retrieved in November 2005, from http://igscb.jpl.nasa.gov/components/prods.html.

Irsigler M, Hein GW, Eissfeller B (2004) Multipath performance analysis for future GNSS signals. Proceedings of the ION NTM 2004, San Diego, California, 26-28 January.

Kaplan ED, Hegarty CJ (2006) Understanding GPS: principles and applications. Artech House Publishers, Boston.

Kim D, Langley R, Bond J, Chrzanowski A (2003) Local deformation monitoring using GPS in an open pit mine: initial study. GPS Solutions 7: 176-185.

Kinawi H, Reda Taha M M, El-sheimy N (2002) Structural health monitoring using the semantic wireless web: a novel application for wireless networking. Proceedings of the 27th Annual IEEE Conference on Local Computer Networks (LCN), Tampa, Florida, USA.

Klobuchar JA (1987) Ionospheric time-delay algorithm for single-frequency GPS users. Aerospace and Electronic Systems, IEEE Transactions on AES-23(3): 325-331.

Klobuchar JA (1996) Ionospheric effects on GPS, in Parkinson BW, Spilker JJ, Axelrad P, Enge P (eds.), Global Positioning System: Theory and Applications

(Volume I). American Institute of Aeronautics and Astronautics, Washington, DC.

Kunysz W (2001) Advanced pinwheel™ compact controlled reception pattern antenna (AP-CRPA) designed for interference and multipath mitigation. Proceedings of the ION GPS 2001, Salt Lake City, Utah, 11-14 September, pp 2030-2036.

Langley RB (1997) GPS receiver system noise. GPS World 8(6): 40-45.

Langley RB (1998) Propagation of the GPS signals, in Kleusberg A, Teunissen PJG (eds.), GPS for Geodesy (2nd edn). Springer-Verlag, Berlin, pp 111-149.

Larson KM, Bilich A, Axelrad P (2008) Improving the precision of high-rate GPS. Journal of Geophysical Research 112: B05422.

Lau L (2004) Investigations into multipath effects on GNSS multiple-frequency single epoch high precision positioning. Proceedings of the ION GNSS 2004, Long Beach, California, 21-24 September, pp 1169-1180.

Leick A (2004) GPS satellite surveying. Wiley, Hoboken.

Leva JL, de Haag MU, Dyke KV (1996) Performance of standalone GPS, in Kaplan D (ed.), Understanding GPS principles and applications. Artech House, Boston, pp 237-285.

Li XJ, Ge LL, Ambikairajah E, Rizos C, Tamura Y, Yoshida A (2006) Full-scale structural monitoring using an integrated GPS and accelerometer system. GPS

Solutions 10: 233-247.

Lovse JW, Teskey WF, Lachapelle G, Cannon ME (1995) Dynamic deformation monitoring of tall structure using GPS technology. Journal of Surveying Engineering 121(1): 35- 40.

Mallat S (1988) Multiresolution representation and wavelets. Grasp. Lap 153, University of Pennsylvania, Philadelphia.

Mallat S, Hwang WL (1992) Singularity detection and processing with wavelets. Information Theory, IEEE Transactions on 38(2): 617-643.

Mallat SG (1989) A theory for multiresolution signal decomposition: the wavelet representation. Pattern Analysis and Machine Intelligence, IEEE Transactions on 11(7): 674-693.

McDonald K (2002) The modernization of GPS: plans, new capabilities and the future relationship to Galileo. Journal of Global Positioning System 1(1): 1-17.

Meng XL, Roberts GW, Dodson AH, Cosser E, Barnes J, Rizos C (2004) Impact of GPS satellite and pseudolite geometry on structural deformation monitoring: analytical and empirical studies. Journal of Geodesy 77: 809-822.

Misra P, Enge P (2001) Global Positioning System: signals, measurements, and performance. Ganga-Jamuna Press, Massachusetts.

Nason GP (1996) Wavelet shrinkage using cross-validation. Journal of the Royal Statistical Society Series B 58(2): 463-479.

Nikolaidis RM, Bock Y, de Jonge PJ, Shearer P, Agnew DC, Van Domselaar M (2001) Seismic wave observations with the Global Positioning System. Journal of Geophysical Research 106(B10): 21,897-21,916.

Ogaja C, Hedfors J (2007) TEQC multipath metrics in MATLAB. GPS Solutions 11: 215-222.

Ogaja C, Rizos C, Wang J, Brownjohn J (2001) Towards the implementation of on-line structural monitoring using RTK-GPS and analysis of results using the wavelet transform. Proceedings of the 10th FIG International Symposiumon Deformation Measurements, Orange, California, 19-22 March, pp 284-293.

Park KD, Elosegui P, Davis JL, Jarlemark POJ, Corey BE, Niell AE, Normandeau JE, Meertens CE, Andreatta VA (2004) Development of an antenna and multipath calibration system for Global Positioning System sites. Radio Science 39(5): RS5002.

Park KD, Nerem RS, Schenewerk MS, Davis JL (2004) Site-specific multipath characteristics of global IGS and CORS GPS sites. Journal of Geodesy 77: 799-803.

Parkinson BW, Enge PK (1996) Differential GPS, in Parkinson BW, Spilker JJ, Axelrad P, Enge P (eds.), Global Positioning System: theory and applications

(Volume II). American Institute of Aeronautics and Astronautics, Washington, DC, pp 3-50.

Pinsky MA (2002) Introduction to Fourier analysis and wavelets. Brooks/Cole, New York.

Radovanovic RS (2000) High accuracy deformation monitoring via multipath mitigation by day-to-day correlation analysis. Proceedings of the ION GPS 2000, Salt Lake City, UT, 19-22 September, pp 35-44.

Ragheb AE, Clarke PJ, Edwards SJ (2007) GPS sidereal filtering: coordinate- and carrier-phase-level strategies. Journal of Geodesy 81(5): 325-335.

Ray JK, Cannon ME, Fenton P (2001) GPS code and carrier multipath mitigation using a multiantenna system. Aerospace and Electronic Systems, IEEE Transactions on 37(1): 183-195.

Satirapod C, Rizos C (2005) Multipath mitigation by wavelet analysis for GPS base station applications. Survey Review 38(295): 2-10.

Schlotzer S, Martin S (2005) Performance study of multi carrier ambiguity resolution techniques for Galileo and modernized GPS. Proceedings of the ION GNSS 2005, Long Beach, CA, 13-16 September, pp 142-151.

Schumacher M, Holländer N, Sauerbrei W (1997) Resampling and cross-validation techniques: a tool to reduce bias caused by model building. Statistics in Medicine 16:

2813-2827.

Seeber G (2003) Satellite geodesy: foundations, methods, and applications. de Gruyter, Berlin.

Seeber G, Menge F, Völksen C, Wübbena G, Schmitz M (1997) Precise GPS positioning improvements by reducing antenna and site dependent effects. Proceedings of the IAG Symposium No. 115, International Association of Geodesy, Rio de Janeiro, Brazil, pp 237-244.

Souza EM, Monico JFG (2004) Wavelet shrinkage: high frequency multipath reduction from GPS relative positioning. GPS Solutions 8(3): 152-159.

Spilker JJ (1996) GPS signal structure and theoretical performance, in Parkinson BW, Spilker JJ, Axelrad P, Enge P (eds.), Global Positioning System: Theory and Applications (Volume I). American Institute of Aeronautics and Astronautics, Washington, DC, pp 57-119.

Spilker JJ, Parkinson BW (1996) Overview of GPS operation and design, in Parkinson BW, Spilker JJ, Axelrad P, Enge P (eds.), Global Positioning System: Theory and Applications (Volume I). American Institute of Aeronautics and Astronautics, Washington, DC, pp 29-55.

Stone M (1974) Cross-validatory choice and assessment of statistical predictions. Royal Statistical Society B 36: 111-147.

Sun Y, Yang YJ, Zhou P (2003) Wavelet-based compression of terrain. Proceedings of the International Geoscience and Remote Sensing Symposium (IGARSS)'03, Toulouse, France, 21-25 July, pp 2030-2032.

Teolis A (1998) Computational signal processing with wavelets. Birkhauser, Boston.

Tiberius C, Pany T, Eissfeller B, Joosten P, Verhagen S (2002) 0.99999999 confidence ambiguity resolution with GPS and Galileo. GPS Solutions 6(2): 96-99.

Vondrak J (1969) A contribution to the problem of smoothing observational data. Bulletin of the Astronomical Institute of Czechoslovakia 20: 349-355.

Vondrak J (1977) Problem of smoothing observational data II. Bulletin of the Astronomical Institute of Czechoslovakia 28: 84-89.

Wan DC, Wei GW (2000) The study of quasi wavelets based numerical method applied to Burgers' equations. Applied Mathematics and Mechanics 21(10): 1099-1110.

Weill LR (2003) Multipath mitigation: how good can it get with new signals? GPS World 14(6): 106-113.

Welch PD (1967) The use of fast Fourier transforms for the estimation of power spectra: A method based on time averaging over short modified periodograms. IEEE Transactions on Audio and Electroacoustics 15: 70-73.

Wells DE, Beck N, Delikaragolou D, Kleusberg A, Krakiwsky EJ, Lachapelle G, Langley RB, Nakiboglu M, Schwarz KP, Tranquilla JM, Vanicek P (1987) Guide to GPS positioning. Canadian GPS Associates, Fredericton, New Brunswick, Canada.

Wübbena G, Bagge A, Boettcher G, Schmitz M, Andree P (2001) Permanent object monitoring with GPS with 1 millimeter accuracy. Proceedings of the 14th International Technical Meeting of the Satellite Division of the Institute of Navigation ION GPS-2001, Salt Lake City, Utah, 11-14 September, pp 1000-1008.

Xiong YL, Ding XL, Huang DF, Dai WJ, Chan WS (2005) Integrated single epoch algorithm based on wavelet transform and its application to structural vibration monitoring. Acta Geodaetica et Cartographica Sinica 34(3): 202-207. (in Chinese)

Zhang WT, Cannon ME, Julien O, Alves P (2003) Investigation of combined GPS/Galileo cascading ambiguity resolution schemes. Proceedings of the ION GPS/GNSS 2003, Portland, USA, pp 2599-2610.

Zheng DW (1988) Discussion on selecting the smooth factor using cross-validation technique. Annals of Shanghai Observatory Academia Sinica 9: 23-26. (in Chinese)

Zheng DW, Luo SF (1992) Contribution of time series analysis to data processing of astronomical observations in China. Statistica Sinica 2(2): 605-618.

Zheng DW, Zhong P, Ding XL, Chen W (2005) Filtering GPS time-series using a Vondrak filter and cross-validation. Journal of Geodesy 79(6-7): 363-369.

Zhong P, Ding XL, Zheng DW, Chen W (2006) Separation of structural vibrations and GPS multipath signals using Vondrak filter. Journal of Central South University (Science and Technology) 37(6): 1189-1195. (in Chinese)

Zhong P, Ding XL, Zheng DW, Chen W, Huang DF (2008) Adaptive wavelet transform based on cross-validation method and its application to GPS multipath mitigation. GPS Solutions 12:109-117.

Zhong P, Ding XL, Zheng DW, Chen W, Xu YL (2007) Filtered-based GPS structural vibration monitoring methods and comparison of their performances. Acta Geodaetica et Cartographica Sinica 36(1): 31-36. (in Chinese)

Zhou Y, Zheng D (1999) Monte Carlo simulation test of correlation significant levels. Acta Geodaetica et Cartographica Sinica 22: 313-318. (in Chinese)